Design methodology for multi-degrees-of-freedom compliant mechanisms with optimal stiffness and dynamic properties

Lum, Guo Zhan

2016

Design Methodology for Multi-Degrees-of-Freedom Compliant Mechanisms with Optimal Stiffness and Dynamic Properties

Guo Zhan Lum

School of Mechanical & Aerospace Engineering

A thesis submitted to the Nanyang Technological University in partial fulfillment of the requirements for the degree of Doctor of Philosophy.

Abstract

Compliant mechanisms are flexible structures that utilize elastic deformation to achieve their desired motions. Using their unique mode of actuation, compliant mechanisms can achieve highly repeatable motions that are essential for high precision micro/nano-positioning applications. As a result, they have been utilized for a wide range of applications like positioning mechanisms for high resolution imaging systems, industrial nano-imprint and nano-alignment applications, and numerous other micro/nano-manipulation tasks. The performance of the compliant mechanisms is highly dependent on their stiffness and dynamic properties because these properties dictate their workspace, transient responses and capabilities to reject disturbances. However, despite the importance of compliant mechanisms, it is still an open challenge to optimize such properties when these structures have multi-degrees-of-freedom.

This thesis addresses these limitations by developing an integrated design methodology that can create multi-degrees-of-freedom compliant mechanisms with optimal dynamic and stiffness properties. This methodology first employs a kinematic approach to select suitable parallel-kinematic configurations for the compliant mechanisms. Subsequently, a structural optimization approach is used to automatically synthesize and optimize the sub-chains' structural topology, shape and size. In order to integrate the kinematic and structural optimization approaches, a new topological optimization algorithm termed the mechanism-based approach has been created. In comparison with existing algorithms, a notable benefit for the mechanism-based approach is that it can eliminate infeasible solutions that have no physical meanings while having a flexible way to change its topology during the optimization process. This algorithm has been shown to be able to develop various devices such as a μ-gripper, a compliant prismatic joint, and a compliant prismatic-revolute joint. A generic semi-analytical dynamic model that can accurately predict the fundamental natural frequency for compliant mechanisms with parallel-kinematic configurations has also been developed for the proposed integrated design methodology.

The effectiveness of the proposed methodology is demonstrated by synthesizing a $X-Y-\theta_z$ flexure-based parallel mechanism (FPM). This FPM has a large workspace of 1.2 mm $\times 1.2$ mm $\times 6°$, bandwidth of 117 Hz, and translational and rotational stiffness ratios of 130 and 108, respectively. The achieved stiffness and dynamic properties show significant improvement over existing 3-degrees-of-freedom, centimeter-scale compliant mechanisms that can deflect more than 0.5 mm and 0.5°. These compliant mechanisms typically only have stiffness ratios and bandwidth that are less than 50 and 45 Hz, respectively. The stiffness and dynamic properties of the optimal FPM were validated experimentally and they deviated less than 9% from the simulation results. Based on the inspirational performance of the $X-Y-\theta_z$ FPM, we envision that the proposed methodology can inspire a variety of high precision machines that have optimal performances.

iv

Acknowledgments

Contents

List of Figures

List of Tables

Chapter 1

Introduction

1.1 Motivation

Compliant mechanisms are flexible structures that are designed to have high compliance in their actuating directions while having high stiffness in their off-axis directions. As compliant mechanisms achieve their motions via elastic deformation, they can effectively eliminate dry friction, mechanical play, backlash and wear-and-tear [1, 2, 3, 4, 5]. These unique characteristics allow the compliant mechanisms to achieve highly repeatable motions, making them the ideal candidates for a wide range of high precision applications; they have been employed as positional mechanisms for high-resolution imaging systems [6], industrial nano-imprint [7, 8] and nano-alignment applications [9, 10, 11], and numerous other micro/nano-manipulation tasks [12, 13, 14, 15, 16]. Furthermore, as compliant mechanisms can be miniaturized easily, they have also been extensively used for MEMS devices [17, 18, 19, 20, 21, 22].

The performance of the compliant mechanisms is highly dependent on their stiffness properties. For example, the actuating stiffness have a direct impact on the workspace because it will be easier to produce large desired deflections when

these stiffness are low. Likewise, when the compliant mechanisms have higher off-axis stiffness, they can reduce the undesired deflections induced by disturbances. Thus, it is desirable to maximize the compliant mechanisms' stiffness ratio, i.e. the ratio of off-axis to actuating stiffness, to optimize the compliant mechanisms' workspace and capabilities to resist disturbances. In addition to attaining good stiffness properties, it is also essential for the compliant mechanisms to achieve a fast dynamic response. However, higher bandwidth requires higher stiffness, and this will generally reduce the workspace and compromise the stiffness ratio of the compliant mechanisms. Therefore, despite the importance of compliant mechanisms, it is still a great challenge to synthesize compliant mechanisms with optimal stiffness and dynamic properties. This is especially true when the compliant mechanisms have multi-degrees-of-freedom.

There are generally two approaches to synthesize compliant mechanisms: the kinematic and the structural optimization approaches. The kinematic approach is an established way to synthesize compliant mechanisms with multi-degrees-of-freedom. The general design procedure is to use a combination of flexural and rigid components such that the compliant mechanism can achieve its desired kinematics. A typical method for the kinematic approach is to first select a traditional mechanism that can fulfill the desired kinematic requirements. Subsequently, a compliant mechanism is synthesized with the selected mechanism's kinematic configuration by using flexures (compliant joints) to replace the traditional joints. The deformation characteristics of the compliant joints are designed to mimic motions achieved by traditional joints. Thus, when the compliant joints are integrated with rigid linkages, the achievable motions of the compliant mechanism are similar with the selected traditional mechanism. As a result, the compliant mechanism's motion can be approximated by using the traditional rigid-

Kinematic Approach

(a) Traditional mechanism

Compliant joint

(b) Compliant mechanism
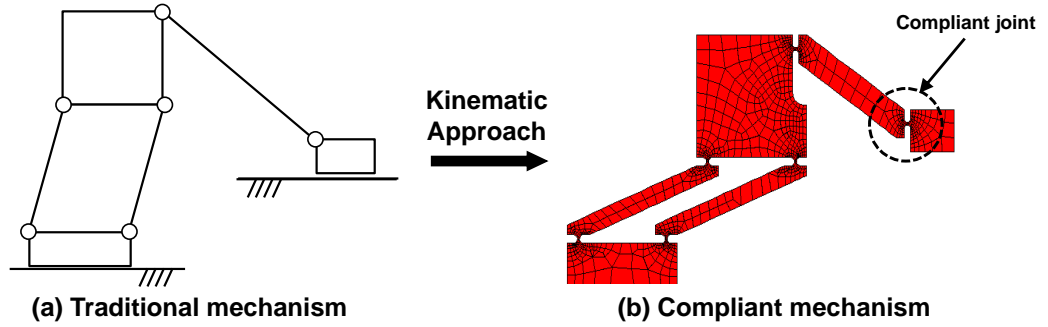
Figure 1.1: An example that illustrates the kinematic approach. A compliant mechanism, shown in (b), is synthesized by replacing the joints of a traditional mechanism, shown in (a), with elastic-bodies called compliant joints. As an example, a compliant joint located on the extreme right of (b) is highlighted.

body kinematics and stiffness analyses. Since there are well-established synthesis guidelines, the kinematic approach has been an effective approach to synthesize a variety of compliant mechanisms [1, 23]. An example of the kinematic approach is illustrated in Fig. 1.1 where the joints of a traditional mechanism's joints are replaced with compliant joints. The main drawback of the kinematic approach, however, is that while the selected topology is feasible, it is not necessarily optimal [24, 25]. As a result, the flexural designs of these compliant mechanism may not have optimal stiffness and dynamic properties, limiting them from fulfilling their maximum potential.

On the other hand, the structural optimization approach synthesizes compliant mechanisms by using optimization algorithms to determine their optimal topology, shape and size [26, 27, 28, 29, 30]. Because the topology has the highest hierarchical rank in the structural form, topological optimization forms the utmost critical aspect in this approach. The general approach for topological optimization is to first determine the fitness function, loading points, the fixed points and the output points of the design domain. Subsequently, the design do-

3

main is discretized into a mesh of finite elements and the aim is to determine the final state for each element - either solid or void. This is determined by iteratively evolving the performance of the compliant mechanism via an optimization algorithm. The performance of the compliant mechanism is determined quantitatively by the fitness function and the behavior of the compliant mechanism is approximated numerically via finite element analysis (FEA). Figure 1.2 shows the general procedure to implement topological optimization method. After obtaining the optimal topology, the performance of the compliant mechanism can be further enhanced with shape and size optimizations. As the structural optimization method synthesizes compliant mechanisms via mathematical programming, it has the potential to select an optimal topology for the structure [28]. Therefore, their synthesized compliant mechanism generally would have better performance compared to their kinematic counterparts.

Unfortunately, the structural optimization approach has its limitations too. For example many established topological optimization algorithms may produce infeasible final designs such as having disconnected solid elements, or elements that are neither solid nor void. Furthermore, unlike the kinematic approach, formulation for the structural optimization problem becomes difficult for compliant mechanisms with more than 1-degree-of-freedom [21, 22, 31, 32] and thus majority of them have only one degree-of-freedom.

In summary, both the kinematic and topological optimization approaches have their corresponding benefits and limitations. For example, although structural optimization method can synthesize compliant mechanisms with optimal characteristics, most of the synthesized compliant mechanisms have only 1-degree-of-freedom. Conversely, the kinematic approach is an established way to synthesize compliant mechanisms with multi-degrees-of-freedom but their obtained stiffness
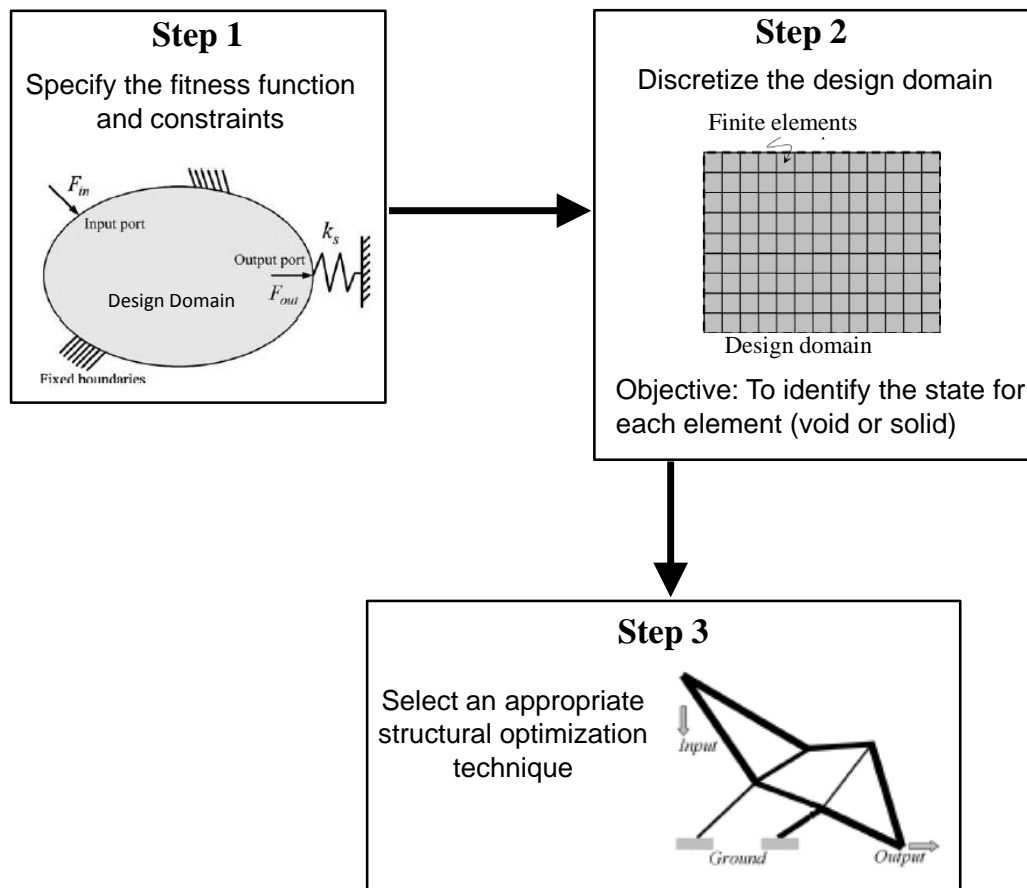
Figure 1.2: The general procedure to implement topological optimization method. Step 1 formulates the optimization problem by specifying the fitness function, constraints, and loading and boundary conditions. This is followed by step 2 where the design domain/space of the compliant mechanism is discretized into a mesh of finite elements. The state of each element can only either be solid or void. Lastly, step 3 uses an appropriate algorithm to perform the structural optimization method, and eventually an optimized design can be obtained.

and dynamic properties might not be optimized. Thus, it is still a great challenge to synthesize multi-degrees-of-freedom compliant mechanisms that have optimal stiffness and dynamic properties.

1.2   Objective and Scope

The objective of this research is to propose a new design methodology that can synthesize multi-degrees-of-freedom compliant mechanisms with optimal stiffness and dynamic properties. The results in this study would enable engineers to synthesize a variety of high precision machines that have optimal performances.

The scope of this thesis is as follows:

- A new topological optimization algorithm will be proposed. The aim of this algorithm is to eliminate the possibility of having infeasible final designs that have disconnected solid elements or ambiguous elements that are neither solid nor void, while having a flexible way to alter their topologies during the optimization process. The effectiveness of this algorithm will be evaluated by creating various flexure mechanisms, including a μ-gripper, a compliant prismatic joint and a compliant prismatic-revolute joint. The stiffness properties of these flexures will also be evaluated experimentally.

- We will also develop a generic dynamic model that can accurately predict the fundamental natural frequency for compliant mechanisms with parallel-kinematic configurations. This model will help to evaluate the dynamic properties of the compliant mechanism during the design optimization process. The accuracy of the model will be evaluated by various compliant mechanisms with random geometries.

- An integrated design methodology that can incorporate the benefits of both the kinematic and structural optimization approaches will be developed. This methodology will provide the critical design steps to create multi-degrees-of-freedom compliant mechanisms with optimal dynamic and stiffness properties.

- An optimal $X - Y - \theta_z$ compliant mechanism will be created based on the proposed design methodology. The stiffness and dynamic properties will

7

be compared with the ones in the literature to illustrate the benefits of the proposed methodology. These properties will also be evaluated experimentally.

1.3   Organization of the Report

The following chapters are organized in the following manner:

Chapter 2 provides the literature review on the synthesis methods for compliant mechanisms. Both synthesis approaches for compliant mechanism - the kinematic and structural optimization approaches will be discussed in detail.

Chapter 3 introduces a new topological optimization algorithm. The performance of this algorithm will be evaluated via the synthesis of a small-scale gripper.

Chapter 4 shows the feasibility of using the structural optimization approach to create various compliant joints, and subsequently assembling them into a multi-degrees-of-freedom compliant mechanism. This will be demonstrated via the development of a 3$\underline{P}$PR compliant mechanism.

Chapter 5 introduces the proposed design approach for optimal compliant mechanisms that have multi-degrees-of-freedom. This will be demonstrated via the development of a $X - Y - \theta_z$ planar-motioned compliant mechanism.

Chapter 6 provides the conclusion of this thesis, discusses about possible future works and also the contributions of this work.

Chapter 2

Literature Review

This chapter provides a detail review for the available methods to synthesize compliant mechanisms. The two general approaches, the kinematic and structural optimization approaches, are discussed in sections 2.1 and 2.2, respectively. A summary of the chapter is given in section 2.3.

2.1 Kinematic Approach

The kinematic approach uses a combination of flexural and rigid-body components such that the compliant mechanism can achieve its desired kinematics. An advantage of the kinematic approach is that it can easily synthesize compliant mechanisms with multi-degrees-of-freedom. Two main methods, the rigid-body-replacement and the constraint-based design methods, are established synthesis procedures that can select suitable kinematic configurations for their compliant mechanisms.

2.1.1 Rigid-body-replacement method

The rigid-body-replacement method synthesizes compliant mechanisms by mimicking the motions of traditional mechanisms [1]. This is achieved by replacing the joints of the traditional mechanisms with suitable flexures known as compliant joints. The elastic deformation characteristics of these compliant joints are designed to mimic motions achieved by corresponding traditional joints. Thus, by assembling corresponding compliant joints with "rigid" bodies, the motions of these compliant mechanisms can be similar to the traditional mechanisms. This resemblance allows the rigid-body-replacement method to predict its end-effector's motion accurately by using traditional inverse kinematics and stiffness analyses [33, 34]. Furthermore, similar to traditional mechanisms, well-developed Lagrangian equations can be used to describe the dynamic behavior of these compliant mechanisms. By using these valuable analyzes, a vast variety of compliant mechanisms had been developed by the rigid-body-replacement method.

Unfortunately, while the rigid-body-replacement method can select a feasible kinematic configuration, its topology is not necessarily optimal. As a result, the performance of these compliant mechanisms, i.e. their stiffness and dynamic properties, are generally not optimal.

2.1.2 Constraint-based design method

The constraint-based design method models the off-axis stiffness axes of the flexures as constraint lines, which can restrict specific motions on the rigid components [4, 5, 34, 35]. Each constraint line is assumed to be able to provide infinite resistive force, restricting the rigid components from moving along it. Once a topology of constraint lines has been set, a line that can intersect all these con-

straint lines is known as a freedom line. This line represents a permitted rotational axis for the rigid component because all the resisting forces do not have an effective moment arm that can supply a resisting torque along that axis. This argument is also true for translational motions as they can be represented by rotations about axes that are located infinitely away from the rigid component. As a result, the number of linearly independent freedom lines that a rigid component possesses, dictates its degrees-of-freedom. Thus, by properly designing the constraint topologies, the desired kinematics for the compliant mechanism can be realized. Although it seems difficult to use intuition to create a suitable constraint topology, all feasible constraint topologies can now be visualized by the freedom and constraint topology (FACT) method [36, 37, 38]. Furthermore, this design process can be further simplified by using the screw theory to mathematically represent the FACT method [39]. As an illustration, Fig. (2.1) shows a compliant mechanism that is synthesized by using five wire flexures (rods) to constrain the end-effector.

Ideally, if all the constraint lines can indeed provide infinite resistive forces to the rigid components, any selected constraint topology would have perfect performance. Unfortunately, this assumption is not true because the off-axis stiffness of the flexures are not infinite, and as the constraint-based design method cannot determine an optimal topology for the compliant mechanism, the overall performance of these compliant mechanisms are not necessarily optimal too.

2.1.3 Compliant joints

In addition to the wire flexures that are shown in Fig. (2.1), there are two other types of elementary compliant joints - the leaf-spring design and the notched-type design (Fig. 2.2 [2, 40, 41]). The leaf-spring compliant joints, also known as
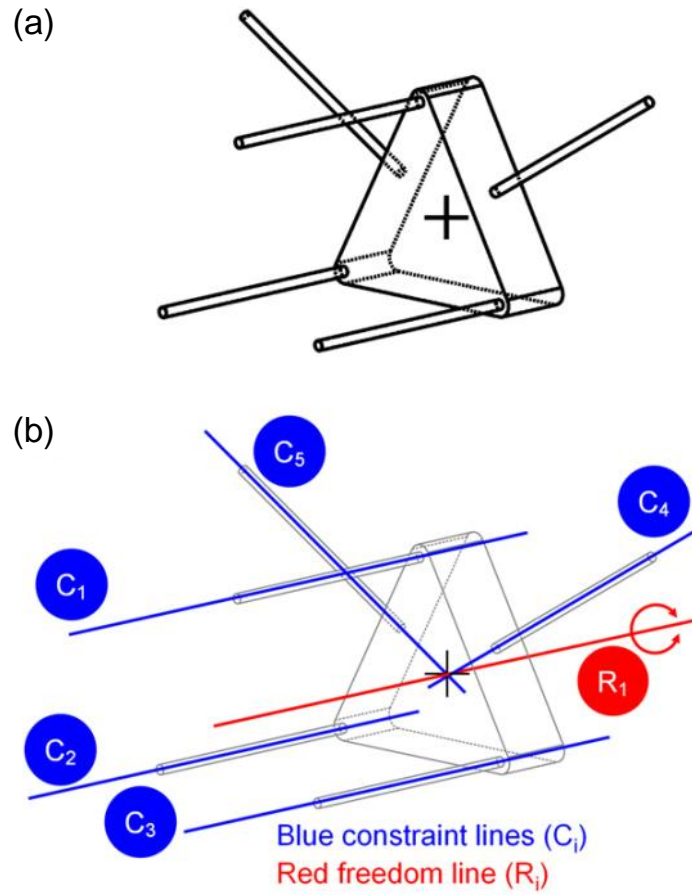
Figure 2.1: A compliant mechanism that is constrained by five wire flexures [36]. (a) A rigid-body (triangular prism) is constrained by five wire flexures (rods). (b) Each wire flexure can be represented as a constraint line that is indicated by a blue line. The freedom line, which is represented in red, shows the permitted rotation achievable by the rigid-body.

blade flexures, are simple beam designs where the flexural thickness and width of the beam are intentionally reduced and increased respectively as shown in Fig. 2.2. By having this configuration, certain planes of this design would have low area moment of inertia while other planes would have high area moment of inertia. Thus, this allows the leaf-spring compliant joint to bend easily in the high compliance directions as shown in Fig. (2.2). This actuating compliance of the leaf-spring designs can be determined by using the classical Euler-Bernoulli equations. In comparison with the notch-type design, the leaf-spring design have higher actuating compliance but with lower off-axis stiffness. Thus, the leaf-spring compliant joints can achieve a larger workspace but at the expense of compromising their off-axis stiffness characteristics.

The last elementary compliant joint, the notched-type design, has cutouts on both sides of a blank to form a necked-down section. While there are various types of notch shaped joints, we have presented three examples in Fig. 2.3. Extensive studies have been carried out to determine the actuating stiffness for different types of compliant joints [2, 41]. The notch-type compliant joints are ideal for applications that only require small workspace where the compliant mechanism does not have to compromise its off-axis stiffness.

Compliant joints with more complex deformation characteristics can be obtained by amalgamating the elementary compliant joints. Some examples of such compliant joints include the cart-wheel and prismatic joints that are shown in Fig. 2.4(a) and (b), respectively. It should, however, be noted that the stiffness characteristics of these elementary compliant joints may not be optimal because their selected topology did not undergo an optimization process.

13
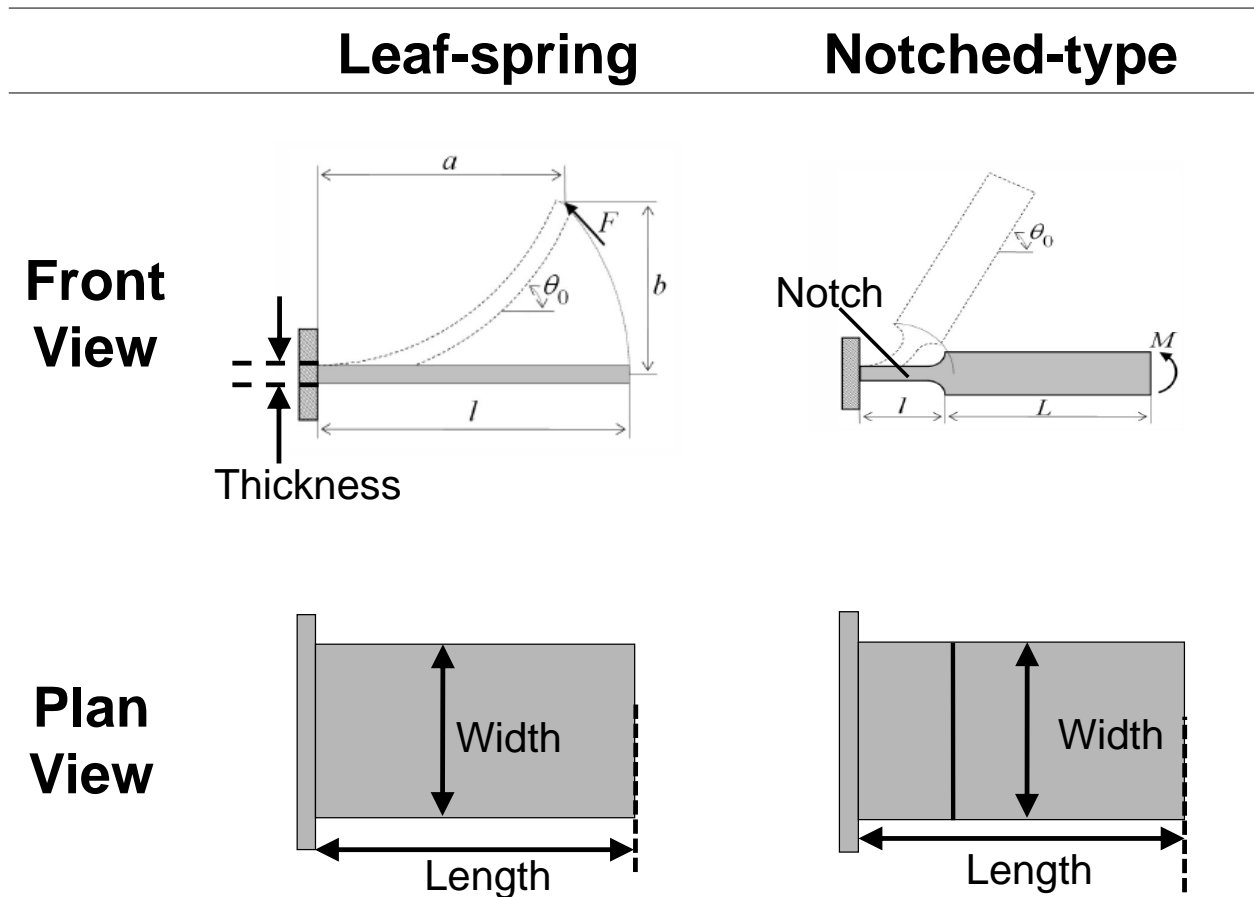
Figure 2.2: The elementary leaf-spring and notched-type compliant joints. The leaf-spring design is a simple beam design that has a high width to thickness ratio. The notch-type design has cutouts on both sides of a blank to form a necked-down section.

Circular
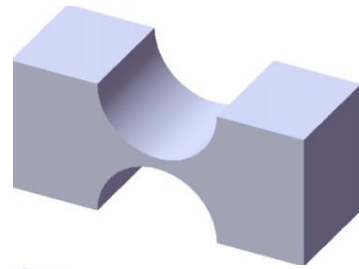
Filleted leaf
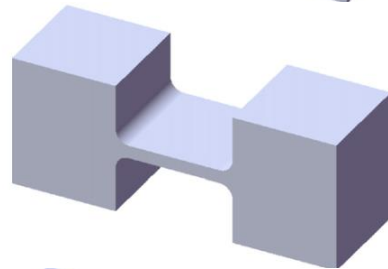
Elliptical
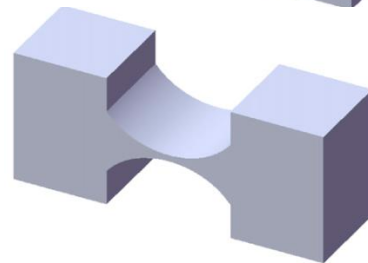
Figure 2.3: Examples of some notch-type compliant joints: the circular, the filleted leaf and elliptical notch-type joints [2, 41].
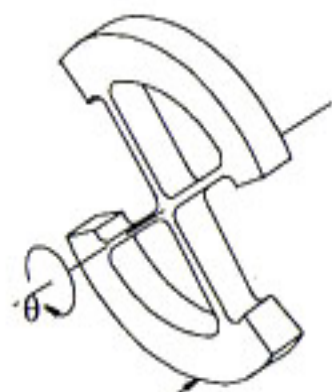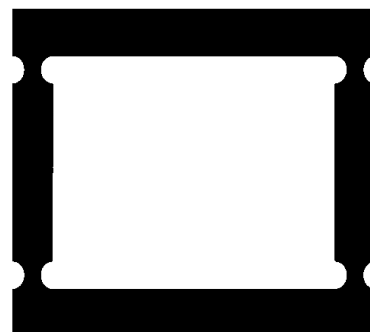
(a) Cartwheel   (b) Prismatic

Figure 2.4: Based on the elementary compliant joints, complex compliant joints such as the (a) cartwheel and (b) prismatic compliant joints can be constructed.

2.1.4 Kinematic configurations

The overall topology of the compliant mechanism, i.e. the connectivity between the compliant joints and the rigid linkages, can be classified into either the serial or parallel kinematic configurations. A compliant mechanism with a serial configuration consists of a chain of compliant joints and rigid linkages that are serially connected to one another. Conversely, a compliant mechanism with a parallel configuration has an end-effector that is articulated by several parallel sub-chains. The parallel-kinematic compliant mechanisms are also commonly termed as a flexure-based parallel mechanism (FPM). An example of a compliant mechanism with a serial configuration is shown in Fig. 2.5(a) while an example of a FPM is illustrated in Fig. 2.5(b).

In comparison, compliant mechanisms with the serial kinematic configuration generally have a larger workspace compared to the FPMs. This is because the elastic deflections of the compliant joints are accumulated for a compliant mechanism with serial kinematic configuration, while the overall stiffness of the FPM is accumulated by the stiffness of each sub-chain. The FPMs, however, have several advantages over their serial counterparts. These include having superior dynamic responses, lower sensitivity towards disturbances and higher off-axis stiffness.

2.1.5 Performances for existing centimeter-scale $X - Y - \theta_z$ compliant mechanisms

The kinematic approach had been used to develop a variety of compliant mechanisms with multi-degrees-of-freedom. Examples of such compliant mechanisms include those with X–Y [35, 42, 43, 44, 45], X– Y– θ_z [9, 10, 46], θ_X– θ_Y–Z [7, 8], X– Y–Z [47, 48, 49] motions, or high precision grippers [14, 15]. As this
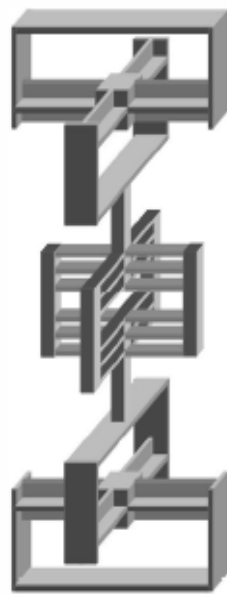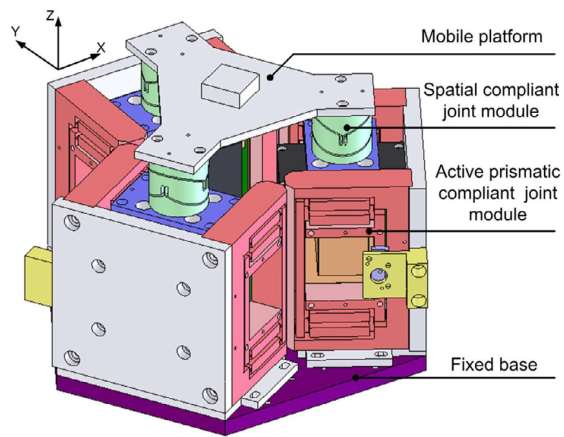
(a) Serial configuration   (b) FPM configuration

Figure 2.5: There are generally two types of kinematic configurations. (a) A serial configured compliant mechanism has a chain of compliant joints and rigid linkages that are serially connected to one another [40]. (b) A FPM has an end-effector that is articulated by several parallel sub-chains [7]. As an example, a sub-chain of a FPM is highlighted.
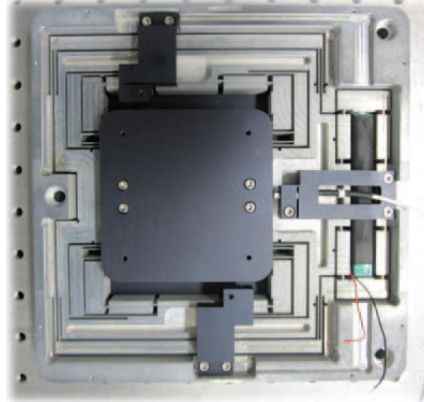
(a) Serial-kinematic X-Y-θ_z
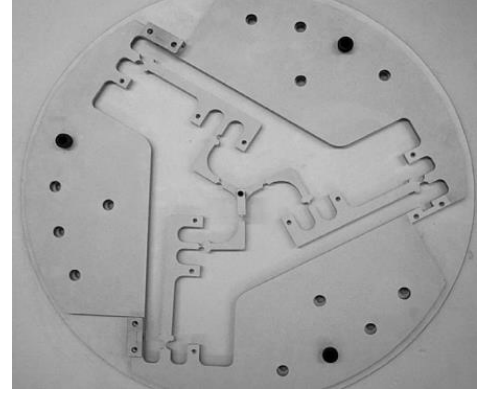
(b) Parallel-kinematic X-Y-θ_z

Figure 2.6: (a) A $X-Y-\theta_z$ compliant mechanism with a serial kinematic configuration [46]. (b) A FPM constructed by Yi et al. that can achieve X-Y-θ_z [51].

report illustrates the proposed integrated design approach via the synthesis of a $X- Y- \theta_z$ compliant mechanism, this sub-section will discuss the performances of such existing structures in detail.

In the literature, $X- Y- \theta_z$ compliant mechanisms can be synthesized with either the serial or FPM configurations as shown in Fig (2.6). In comparison, the FPMs are more popular as they have superior dynamic responses, lower sensitivity towards disturbances and higher off-axis stiffness. Among the developed $X- Y- \theta_z$ FPMs, many are synthesized by replacing the traditional revolute joints with compliant notch joints [9, 10, 12, 50]. Due to the high actuating stiffness of the notch-type compliant joints, the resultant workspaces for these FPMs are small. The allowable translational and rotational motions of these FPMs are only within hundreds of micrometers and arcseconds, respectively. The small workspace characteristics for these FPMs are primarily restricted by the high actuating stiffness nature of the notch joints.

Larger workspace FPMs, however, can be obtained by replacing the compliant notch joints with the more compliant beam joints [11, 52]. For example, the beam-type $X - Y - \theta_z$ FPM constructed by Yang et al. can achieve

18

a large workspace of ± 2.5 mm $\times \pm 2.5$ mm $\times \pm 2.5°$[11]. However, the non-actuating stiffness of these FPMs are lower than their notch joint counterparts and this results in lower resistance towards unwanted external disturbances. Thus, the stiffness characteristics for both the notch-type and beam-type FPMs are not optimal as the former is too stiff while the latter is too compliant. Furthermore, the typical stiffness ratio of their end-effector, i.e. $K_{zz}/K_{yy}, K_{zz}/K_{xx}, K_{\theta_x\theta_x}/K_{\theta_z\theta_z}, K_{\theta_y\theta_y}/K_{\theta_z\theta_z}$, only range between 0.5-50, regardless of the type of elementary compliant joints the $X-Y-\theta_z$ FPM utilized [7, 8, 9, 10, 11, 46, 50, 51, 52, 53]. The variables K_{xx}, K_{yy}, K_{zz} refer to the end-effector's stiffness along the $x-, y-$ and $z-$axes, respectively. Likewise, the variables $K_{\theta_x\theta_x}, K_{\theta_y\theta_y}, K_{\theta_z\theta_z}$ refer to the end-effector's stiffness about the $x-, y-$ and $z-$axes, respectively. Although it is possible to increase the FPMs' stiffness ratio by increasing the aspect ratio of their compliant joints (the flexures' width to thickness ratio), the maximum achievable aspect ratio is constrained by two factors. Firstly, in order to operate the FPM within its elastic regime, the induced stress on the compliant joints must not exceed their fatigue stress. This dictates that the flexural thickness of the compliant joints cannot be too small. Secondly, if the flexural width of the compliant joints is too large, the FPM's actuating stiffness might become too high for the FPM to achieve its required workspace. Therefore, the development of a $X-Y-\theta_z$ FPM that has a high stiffness ratio greater than 100 is still a great challenge.

In addition to attaining good stiffness properties, it is also essential for the $X-Y-\theta_z$ compliant mechanism to obtain a fast dynamic response. However, higher bandwidth requires higher stiffness, and this will reduce the workspace of the compliant mechanism. As an example, the bandwidth for the $X-Y-\theta_z$ compliant mechanisms that have workspace of 0.22 mm$\times$0.22 mm$\times$0.22° and 0.52

19

mm$\times$0.6 mm$\times$0.3$°$ are reported to be 84 Hz [50] and 45 Hz [46] respectively. Large workspace 3-degrees-of-freedom compliant mechanisms that can deflect more than 0.5 mm and $0.5°$, have yet to achieve a high bandwidth that is greater than 45 Hz [7, 8, 46, 52].

2.2   Structural Optimization Approach

The structural optimization approach synthesizes compliant mechanisms automatically via numerical methods such as optimization algorithms and finite element analysis (FEA). By following the structural hierarchy of the compliant mechanism, this synthesis approach will sequentially determine the structure's topology, shape and size. A compliant mechanism's topology can be described as its overall connectivity. For a selected topology, the curvature of a segment that connects different portions of the compliant mechanism can be described as shape. Lastly, based on the selected topology and shape, the physical dimensions of the compliant mechanism can be described as size. In particular, the topological optimization is the most essential component in the structural optimization method and it will be discussed in detail in this section.

Topological optimization determines the compliant mechanisms' optimal overall connectivity via optimization algorithms. This is achieved by first defining the fitness function, loading and boundary conditions of the design domain. Subsequently, the design domain is discretized into a mesh of finite elements and the aim is to identify the state of the elements. Note that topological optimization is a discrete-natured optimization problem as the state of the elements can only either be solid or void. The final state of the elements is determined after the performance of the compliant mechanism had gone through iterations of evolution. Performance is quantitatively defined by the fitness value, which is in turned
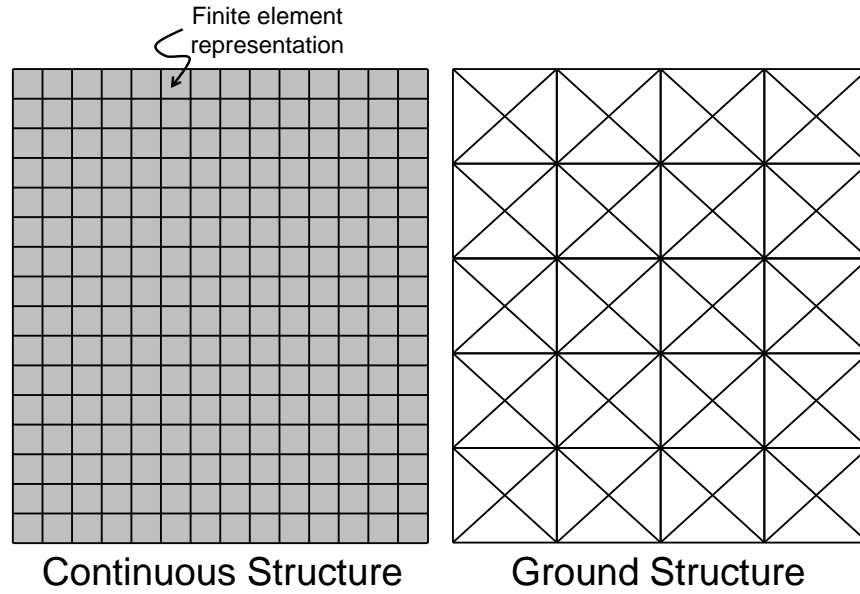
Figure 2.7: Comparison between continuous structure and ground structure topology. The design domain of a ground structure topology is made of discrete components such as bars, beams or frames.

evaluated via FEA.

From the current literature, there are a number of algorithms developed to perform topological optimization. These include the homogeneous [28, 40, 54], simple isotropic material with penalization (SIMP) [26, 55, 56, 57, 58, 59, 60, 61], evolutionary structural optimization (ESO/BESO) [27, 62, 63], genetic algorithm (G.A.) based algorithms [29, 32, 64, 65, 66, 67], level set methods [68, 69, 70, 71], ground-structure [31, 72, 73, 74, 75, 76, 77] and building block algorithms [30, 78]. Continuum structure topologies can be optimized by homogeneous, SIMP, BESO, level set and G.A. based algorithms. Ground structure algorithms, on the other hand, optimize the topology that is composed by discrete bars/beams/frames. The comparison between the topology of continuous structure and ground structure is illustrated in Fig. 2.7.

As these algorithms differ from one another in their modeling and optimization schemes, each of them has their corresponding benefits and limitations. The

21

following sub-sections will describe these various algorithms.

2.2.1 Homogeneous

The homogeneous algorithm introduces a hole within every finite element in the design domain [54]. This is illustrated in Fig. 2.8 where the variables a and b determine the size of the hole and θ determines its orientation. Performance of the topology will change when the size and orientation of the holes vary. Thus, by doing a size optimization on the holes, the optimal topology can be determined. If the size of the hole is as large as the element, this element is considered as a void element. Likewise, if the hole vanishes, it means that this element is considered as a solid element. As the design variables are continuous, the optimization problem can be converted from a discrete-natured one into a continuous one. This simplifies the optimization problem and allows the homogeneous algorithm to utilize a gradient-based solver. Note that gradient-based solvers can only be used for continuous optimization problems. Based on the fitness function, the solver will iteratively search for a new solution until the fitness value converges to a solution. The resultant topology will be deemed as the optimal topology.

The homogeneous algorithm has two advantages. Firstly, it has good convergence as it uses a gradient-based solver. Secondly, as the homogeneous algorithm factors in the orientation of the inner hole, this optimization can be extended to composite materials as well.

However, this algorithm has also two drawbacks. The homogeneous algorithm may produce infeasible designs such as having microscopic sized holes and disconnected solid elements. Figure 2.9 illustrates an example of a topology, which consists of disconnected solid elements. In addition, since the homogeneous method uses gradient-based solvers, the optimal topology is very sensitive
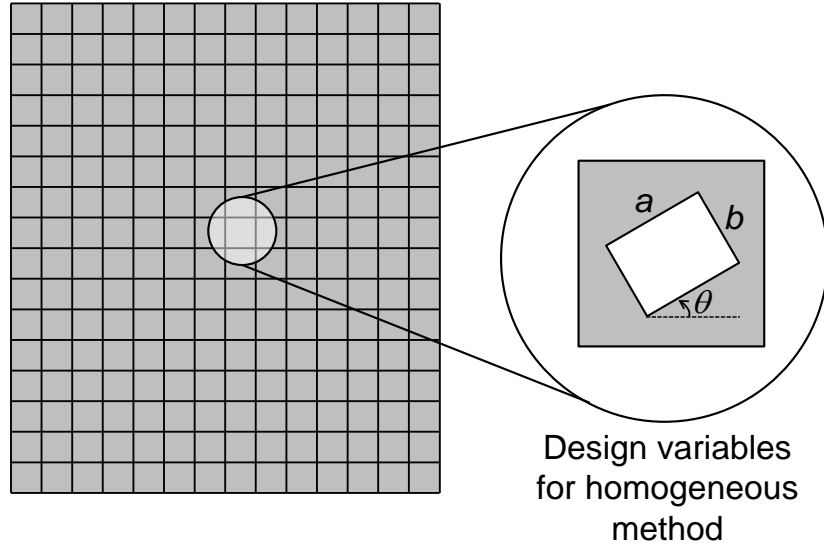
Figure 2.8: Illustration of the design variables for homogeneous method. Within each finite element, a void with the size of $a \times b$ is introduced. The orientation of each void can be specified by the angle θ.

to the initial guess. This implies that there is a higher probability to converge to a local solution, instead of the global one.

2.2.2 Solid isotropic material with penalization (SIMP)

The SIMP algorithm assigns each element with an artificial density [26]. These densities are continuous design variables that range between '0' and '1'. Elements with density values of '1' and '0' represent solid (black) and void (white) elements, respectively. As the densities are continuous design variables, SIMP can also convert the discrete natured topological optimization problem into a continuous one too. Gradient-based solvers can thus be utilized to perform a "size" optimization on the densities to obtain the optimal topology. The gradient for the fitness function can be obtained from the FEA.

Ideally, all the elements in the optimal topology should be either '1' or '0'. However, in actual implementations, SIMP will usually generate elements that
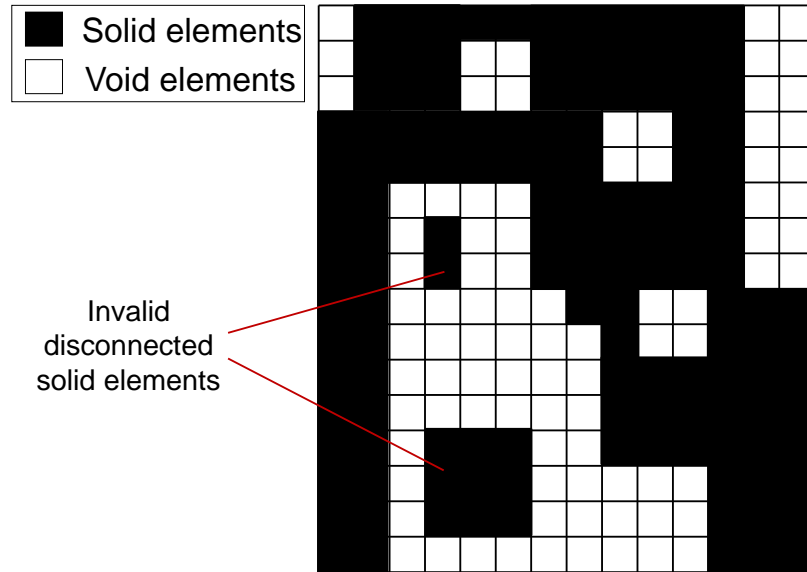
Figure 2.9: Illustration of an infeasible design that consists of disconnected solid elements. In this illustration, the final design is composed of three solid pieces which are disconnected to one another.

are in between '0' and '1'. These are termed as 'grey' elements and they do not have any physical representations. Thus, designers would have to use their intuition to determine the final state of these 'grey' elements. As a result, the performance of the topology usually deteriorates. Figure 2.10 illustrates the 'grey' elements that are produced by SIMP. In addition to having ambiguous 'grey' elements, SIMP may also produce disconnected solid elements that are invalid too.

Despite the shortcomings of SIMP, it is important to note that SIMP is able to demonstrate good converge capability [26, 56]. It is also an established topological optimization algorithm that is highly robust, and has been utilized for a vast range of applications.
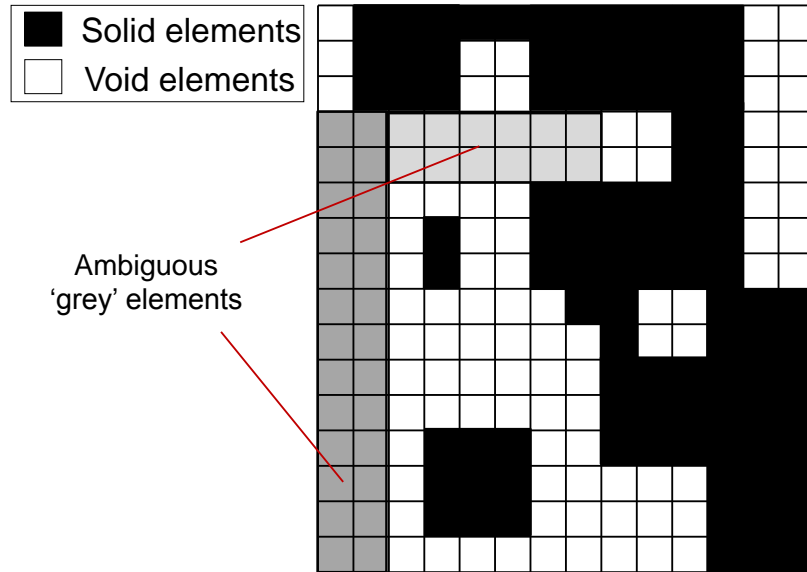
Figure 2.10: Ambiguous 'grey' elements that maybe produced by SIMP. Ideally, all the elements in the mesh should either be solid or void. The 'grey' elements are ambiguous as they are neither solid nor void.

2.2.3 Evolutionary structure optimization/bi-directional evolutionary structure optimization (ESO/BESO)

The ESO/BESO algorithm uses identical design variables as SIMP, where each element is assigned a continuous artificial density. Similarly, the gradient of the fitness function is evaluated via FEA. However, in contrast to SIMP, ESO/BESO does not rely on mathematical programming. Instead, it relies on a set of rules to determine the state of the elements [27, 62, 63]. The earlier version of ESO has only rules to remove solid elements [27] while recent progress allows BESO to add solid elements back to the structure [63]. As ESO/BESO uses a rule-based approach, the artificial densities for all elements remain either a 'zero' or a 'one' at all times. Thus, the possibility of having 'grey' elements does not occur for BESO.

Nevertheless, ESO/BESO was largely criticized for its heuristic approach to perform the optimization process. It has been illustrated that on several occasions, the ESO/BESO algorithm is unable to converge into a solution [79]. Furthermore, similar to homogeneous and SIMP, the ESO/BESO algorithm may produce disconnected solid elements as well.

2.2.4   Genetic algorithm based algorithm

Genetic algorithm (G.A.) is a search and find optimization solver and it will create an initial population of random chromosomes to represent the design parameters. By employing the concept of "survival of the fittest", G.A. can evolve the population gradually until the optimal solution is obtained. When G.A. was first employed for topological optimization, each chromosome maps a corresponding topology by assigning every element in the design domain with a binary number of either a '0' or a '1'. A value '1' corresponds to a solid element while a '0' indicates a void. As genetic algorithm is a discrete solver in nature, it can tackle the topological optimization efficiently and thus it does not produce any 'grey' elements like SIMP [80]. However, this modeling has a high possibility to produce disconnected solid elements. Fortunately, this issue was eventually resolved when the morphological method was introduced. Instead of using the state of every element as the design variables, the chromosomes of the morphological methodology use the geometrical structure of animals to represent a topology [29, 32, 64, 65, 66]. Each topology differs from one another in terms of the locations of their loading, support and output points and the Bezier curves that connect these points. These Bezier curves form the skeleton of the 'animal' and corresponding flesh are added onto the skeleton to form a corresponding topology. Figure 2.11 shows a typical mapping for the morphological method. The

(a) Discretize the design domain

(b) Connect input/output with
Bezier curves with control points (•)

(c) Skeleton made of elements
along the curves

(d) Add flesh to the skeleton to form
the final structure
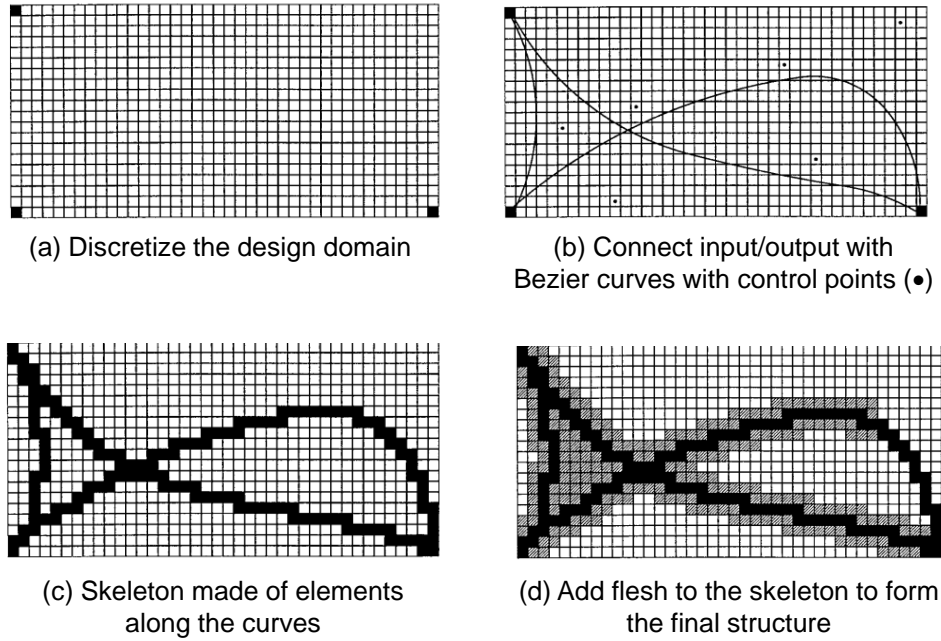
Figure 2.11: A typical mapping for the morphological method [29]. The output, input and fixed points are connected to one another via a skeleton that is formed by various Bezier curves. Subsequently, additional flesh are added to the skeleton to form a corresponding compliant mechanism.

solver will continue to evolve the population of chromosomes until the fitness function converges to a minimum. With the mutation function, the G.A. solver has a higher chance to search for the global minimum while exhibiting good convergence capability [64]. Furthermore, it is important to highlight that the solution is always feasible as it does not produce checkerboard, ambiguous 'grey' elements and disconnected solid elements.

Recent advances of this method introduce the concept of "passive" and "active" Bezier curves [32, 66]. The "passive" curves are curves that do not appear on the topologies while the "active" curves do appear. Based on the performance, all the Bezier curves have the option to switch between "active" and "passive". This essentially increases the search space for the optimization and adds more flexibility in choosing the number of curves. However, the main drawback of

this method is that the designer would not know the maximum number of Bezier curves required (active plus passive). In addition, new holes cannot be introduced within each Bezier curve as all elements within the "flesh" components are always solid. Lastly, it requires more computational time and power to implement this algorithm.

2.2.5 Level set method

The level set method uses moving boundaries as its design variables. Elements that are within the boundaries are considered solid while others are void. This effectively allows the optimization process to be performed discretely and eliminates the possibility of having ambiguous "grey" elements. The moving boundaries are represented by a scalar function of a higher dimensionality known as the level set function [68, 69, 70, 71]. This function allows the topology/shape of the compliant mechanism to undergo drastic changes while it remains simple and continuous. A speed function is used to represent the motion of the moving boundaries and it can be determined by FEA. One notable advantage of using the level set method is that it does not require a seed; thus, it does not have limited sets of solutions. When the boundaries move, a boundary can be spilt to form more boundaries or several boundaries may form into one. By using the topological derivatives in conjunction with the level set method, new holes can be generated [69].

As the optimization is usually solved by using steepest descent, it is very sensitive on the initial guess. Thus, it is very likely that the final design will converge to a local minimum instead of the global solution. In terms of the computational power, the level set method is computationally more expensive than SIMP and homogeneous algorithms. Similar to other algorithms, the level set method may
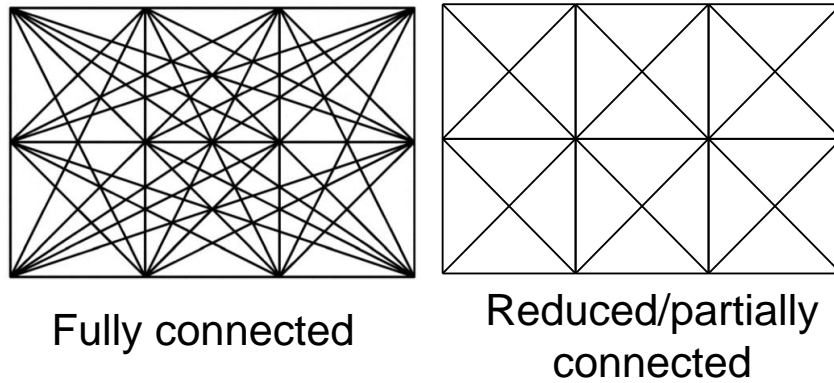
Figure 2.12: The two types of ground structure topology. The fully connected topology has a more inclusive topology compared to its reduced/partially connected counterpart.

produce disconnected solid elements as well.

2.2.6 Ground structure algorithms

As mentioned earlier, the ground structure algorithm differs from all of the above methods as it uses a discrete form of topology to represent its design domain [31, 72, 73, 74, 75, 76, 77]. In general, there are two different types of ground structure topology - the reduced/partial topology and the fully connected topology as shown in Fig. 2.12. Regardless if it is fully- or partially-connected, each connecting element is typically modeled as a bar, beam, or frame.

The fully connected topology will allow the user to have a more inclusive topology. However, this will also increase the complexity of the problem and the optimal topology is usually harder to be manufactured. Solutions obtained from the fully-connected topology are also generally stiffer than the ones obtained from the reduced connected topology.

Once the design domain has been selected, the cross-sectional area of the el-

ements will be optimized by the ground structure algorithm. This allows both topological and size optimization to be carried out simultaneously. The major drawback of this method is that even if one is using a fully-connected ground structure topology, it is still not as inclusive as the ones obtained via continuous structure. In addition, ground structure topology is highly sensitive to the modeling of each element. Based on different types of modeling, the optimized topology will change accordingly.

2.2.7 Building block algorithms

There are generally two types of building block algorithms. The first algorithm uses the concept of 'divide and conquer' to synthesize their compliant mechanisms [78]. This is achieved by first pre-defining the required stiffness properties of the compliant mechanisms and decomposing the synthesis process into multiple sub-problems. The objective of each sub-problem is to match specific stiffness ratios by using a combination of basic building blocks. Based on this approach, the building block method is similar to the kinematic approach because it aims to identify feasible topologies for the compliant mechanism. Thus, there may exist multiple feasible topologies, and the selected topology may not have optimal performance.

The second algorithm uses the reduced connected topology to represent the design domain [30]. Instead of using elementary bars, beams or frames, however, this algorithm uses a library of basic blocks to represent each sub-block in the design domain. Similar to other topological optimization algorithms, it is difficult to use this algorithm to construct compliant mechanisms with multi-degrees-of-freedom. Furthermore, similar to the ground structure algorithms, the represented topology is not as inclusive as the ones obtained via continuous structure.

2.2.8 Fitness functions for topological optimization

In addition to the fitness function mentioned for the building block algorithm, other available fitness functions for topological optimization include the geometric advantage, mechanical advantage, energy efficiency and reduced path error [28]. Geometric advantage fitness functions minimize the ratio of the input displacement against the output displacement while the mechanical advantage minimizes the ratio of the input force against the output force. If the designer considers both geometric and mechanical advantage concurrently, the energy efficiency fitness function can be used. The reduced path error fitness function is used when one tries to design a compliant mechanism, which can follow a prescribed path indicated by the designer. In addition to these fitness functions that focus on the static behavior of the compliant mechanisms, the topological optimization method has been shown to be able to optimize their dynamic responses too. The popular approach for dynamic optimization is to maximize the fundamental natural frequencies of the compliant mechanism by using the Rayleigh principle. Despite the variety of available fitness functions, it should be noted that most of these functions are only valid for compliant mechanisms with 1-degree-of-freedom, and the optimization formulations become difficult when multi-degrees-of-freedom are required.

2.3   Summary

Based on the current literature, the kinematic and structural optimization approaches are two main ways to synthesize compliant mechanisms. The advantage of the kinematic approach is that it is an established way to design compliant mechanisms with multi-degrees-of-freedom. However, its major drawback is that

the flexural designs of these compliant mechanisms are generally not optimized as their selected topology are not necessarily optimal. On the other hand, although the structural optimization approach can produce optimal configurations, it has several limitations too. For example, algorithms such as SIMP and homogeneous methods may produce infeasible solutions that have ambiguous "grey" elements and microscopic voids, respectively. Many algorithms also suffer from having infeasible solutions that have disconnected solid elements. A brief summary of these limitations can be found in Table 2.1. Furthermore, the formulation of the structural optimization problem becomes difficult for compliant mechanism with multi-degrees-of-freedom [31, 32]. As a result, most of the compliant mechanisms synthesized via structural optimization method generally only have 1-degree-of-freedom. It is still an open challenge to develop a new approach that can synthesize multi-degrees-of-freedom compliant mechanisms with optimal dynamic and stiffness properties.

Table 2.1: Summary of the limitations of existing topological optimization methods. The columns indicate the common limitations for topological optimization methods, i.e. whether they will produce ambiguous 'gray' like elements, disconnected solid elements, have poor convergence capabilities, may over constrain the search sapce and whether they require high computational cost. Conversely, the rows represent the existing methods and this include the homogenuous, SIMP, level set, morphological, building block and ground structure methods. The limitations for each method is indicated with a corresponding checkmark.

	'Gray' elements	Disconnected elements	Poor convergence	Over constrain	High computational cost
Homogenuous	✓	✓			
SIMP	✓	✓			
ESO		✓	✓		
Level set		✓			✓
Morphological				✓	✓
Building block method		✓		✓	
Ground structure		✓		✓	

33

Chapter 3

The Mechanism-based Topological Optimization Algorithm

This chapter introduces a new topological optimization algorithm termed the mechanism-based approach. This algorithm is specifically created for the proposed integrated design methodology. The procedure to carry out the mechanism-based approach will be discussed in Section 3.1. Subsequently, the performance of the proposed algorithm will be evaluated by a test problem in Section 3.2 and a summary will be given in Section 3.3.

3.1 Geometrical Mapping for the Mechanism-based Approach

Inspired by the morphological algorithm that can eliminate infeasible solutions, we develop a new topological optimization termed the mechanism-based approach. This algorithm uses traditional mechanisms as seeds to represent the topology of the continuum compliant mechanism. In order to implement the

mechanism-based approach, traditional mechanisms that have the same degrees-of-freedom as the compliant mechanism are selected as seeds. If there are multiple seeds, a discrete variable, m, will be used to select a seed to superimpose onto a design domain where all the finite elements are initially selected as void. The position of links' tip for the selected seed will be defined by other design variables.

Once the seed has been superimposed, there are two ways to represent its links. The first way is to represent each link with a straight line and all the finite elements that are in contact with the selected seed are converted into solid elements. As the solid elements are selected in a discrete manner, no ambiguous "grey" elements can be formed.

Alternatively, the second way represents each link of the mechanism with one cubic curve, one harmonic curve (sinusoidal curve), and their reflected curves about the link. As an example, the second way of mapping is illustrated with a four-bar linkage seed in Fig. 3.1. The four curves form the boundaries used in the selection of solid elements. Based on the value of γ assigned to each link $(\gamma \in \mathbb{Z}^+, 1 \leq \gamma \leq 3)$, different combinations of solid elements can be generated. If $\gamma = 1$, all the elements bounded between the original curves and the link are solid. When $\gamma = 2$, all the elements bounded by the reflected curves and the link are solid. When $\gamma = 3$, the solid elements will be the combined elements of $\gamma = 1$ and $\gamma = 2$ cases. Similar to the first way of mapping, the second way selects their solid elements in a discrete manner and this prevents any ambiguous "grey" elements from forming.

Using the second way of mapping, the cubic curves are designed to have one stationary point within the link length so that the harmonic curves can be enclosed. With this configuration, it is possible to create holes within each link.

36
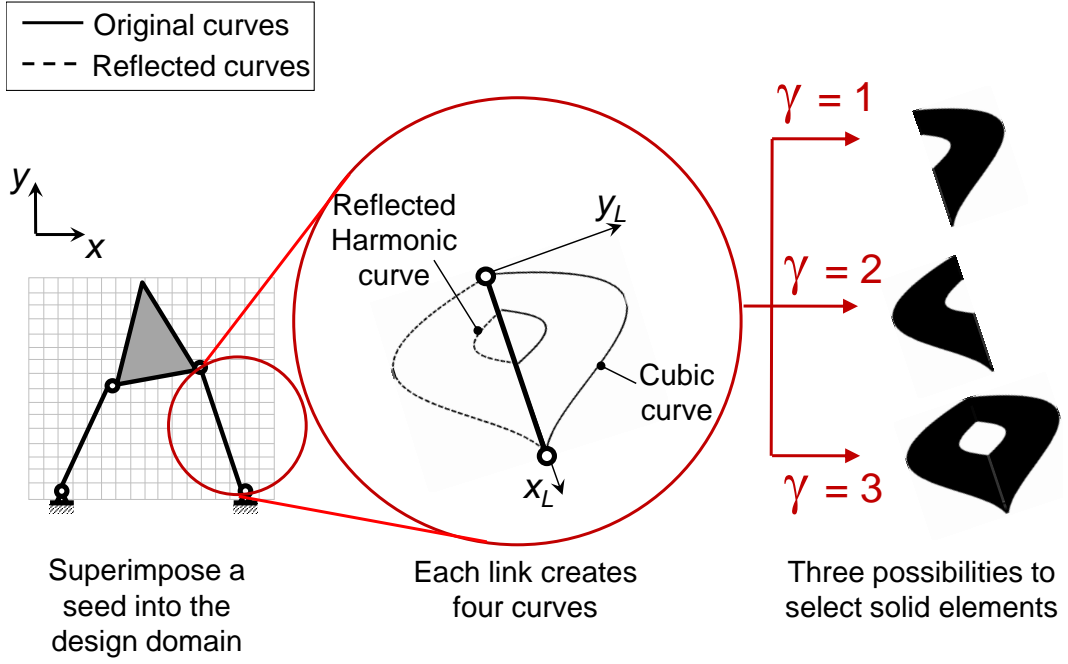
Figure 3.1: The procedure to implement the mechanism-based approach. In this example, a four-bar linkage seed is superimposed onto a mesh of void elements. Each link of the seed is represented with four curves and based on the value of the variable γ, different combinations of solid elements can be generated.

The number of holes for $\gamma = 3$ is equal to $2n_h - 1$ where n_h is a positive integer that represents the number of troughs and peaks of the harmonic curve. The cubic curves can be described by using three parameters - the link length, L, and another two parameters, α and β. These three parameters define the coordinates of the stationary point $(x_{L,\text{max}}, y_{L,\text{max}})$ such that $x_{L,\text{max}} = \alpha_c L$ and $y_{L,\text{max}} = \beta_c L$. With the boundary conditions $(0,0)$ and $(L,0)$ in the $x_1 - y_1$ frame, the cubic curves' equations are:

$$y_L = \pm(a_c x_L^3 + b_c x_L^2 + c_c x_L + d_c) \quad \text{where}$$
$$a_c = -\beta_c \frac{2\alpha_c - 1}{(\alpha_c(\alpha_c - 1))^2},$$
$$b_c = \beta_c \frac{3\alpha_c^2 - 1}{(\alpha_c(\alpha_c - 1))^2 L} \tag{3.1}$$
$$c_c = -(a_c L^2 + b_c L) \quad \text{and} \quad d_c = 0.$$

Equation (3.1) with the plus sign represents the original cubic curves. Four independent parameters s_h, n_h, e_h and h are used to define the harmonic curves. The parameters s_h and e_h determine the starting and ending point of the curve respectively and h determines the amplitude of the curve. If $(s_h + e_h) \geq 1$ or $h = 0$, no harmonic curves are produced and thus no holes are formed. Figure 3.2 shows the corresponding parameters for the original curves and $n_h = 1$ for the harmonic curve as there is only one peak. The equations of the harmonic curves for $s_h L \leq x_1 \leq L - e_h L$ are:

$$y_L = \pm h \sin\left[\frac{2\pi}{\lambda_h}(x_L - s_h L)\right] \tag{3.2}$$

where λ_h is the wavelength and it is expressed as:

$$\lambda_h = 2 \frac{L - (s_h L + e_h L)}{n_h}. \tag{3.3}$$

Note that Eq. (3.2) with the plus sign represents the original harmonic curves. A corresponding topology is produced when all the links follow the above-mentioned description and a particular representation example is shown in Fig. 3.3 An advantage for introducing γ is that it enables a wider range of topology that are able to be generated by the continuous cubic and harmonic curves. In com-

(a) Parameters for the cubic curve

(b) Parameters for the Harmonic curve
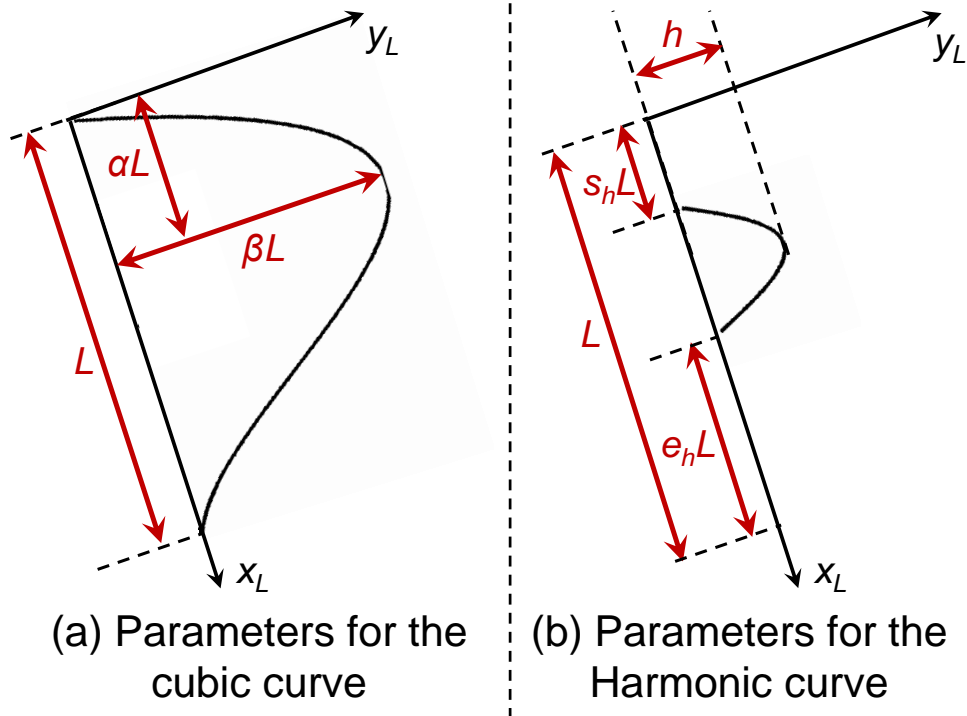
Figure 3.2: The design variables required to map the cubic and harmonic curves. (a) The design variables, α, β and L, will define the curvature of the cubic curves. (b) The design variables, h, s_h, e_h and L, will define the curvature of the harmonic curves.

Illustration for Mechanism-based approach

Geometrical properties
of seed

Mapping

The created compliant
mechanism
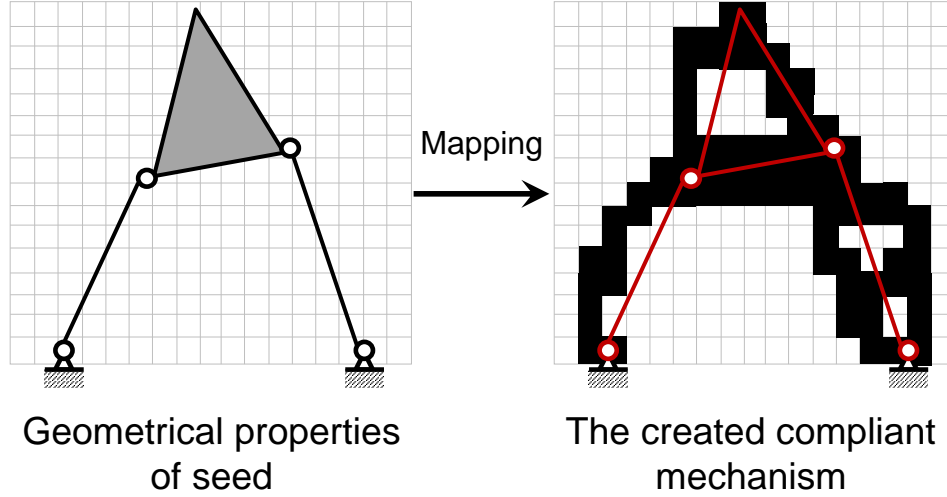
Figure 3.3: A corresponding compliant mechanism is formed based on the curves' parameters, and the seed's topology and posture. The black and white elements represent the solid and void elements, respectively.

parison, the second mapping has the potential to create topologies that are more complex but this will require more computational time and resources. Thus, if the computational resources permits, the second mapping might be a better option to represent the linkages of the seed.

Regardless of the way to represent the links, this algorithm will not produce disconnected solid elements because the links of the traditional mechanism are always physically connected to one another. In addition, topologies created via the mechanism-based approach are not limited by its seeds because if any links' length approaches zero during the optimization process, even the seeds' "topology" can be changed. This effectively allows the mechanism-based approach to have a more flexible way to perform the optimization process. The optimization problem will be solved by using G.A. and each chromosome contains the information of the design variables (the position of the links' tip, and possibly the curves' parameters). Based on the specified fitness function, G.A. will grad-

40

ually evolve these solutions until an optimum solution is found. As G.A. is used as the solver, the possibility of arriving at the global solution is higher than the gradient-based methods. However, it should also be noted that in comparison to gradient-based methods, more computational time and power are required to achieve this. Note that generally methods like SIMP, ESO and homogeneous will require minutes to complete while our method may require a few hours.

3.2 Design of a Small Scale Flexure-based Mobile μ-grippers

The performance of the mechanism-based approach is investigated via a test problem - synthesizing a millimeter-scale mobile gripper known as a μ-gripper . This μ-gripper is designed to function as an untethered small-scale device that can perform effectively micro-manipulation by grabbing and manipulating micro-scale objects. The conceptual design of the μ-gripper is shown in Fig. 3.4, where each arm of the μ-gripper has a rigid component and a flexure (compliant mechanism). The function of the rigid component is to grab and manipulate micro-objects while the compliant mechanism allows the μ-gripper to achieve its desired deflections.

The desired motion of the compliant mechanism can be seen in Fig. 3.4 where the flexure can provide a large x-axis translational deflection when it is subjected to a torque in the z-axis. In order to create this torque, $\mathbf{M}_z$, via magnetic actuation, the rigid component has a magnetic moment that is parallel to its y-axis body frame (Fig. 3.4); the actuating torque can be generated by placing the μ-gripper at the center of an electromagnetic coil system and use this system to supply an external magnetic field that is parallel to the x-direction ($\mathbf{B}_x$) (see Fig. 3.5). The
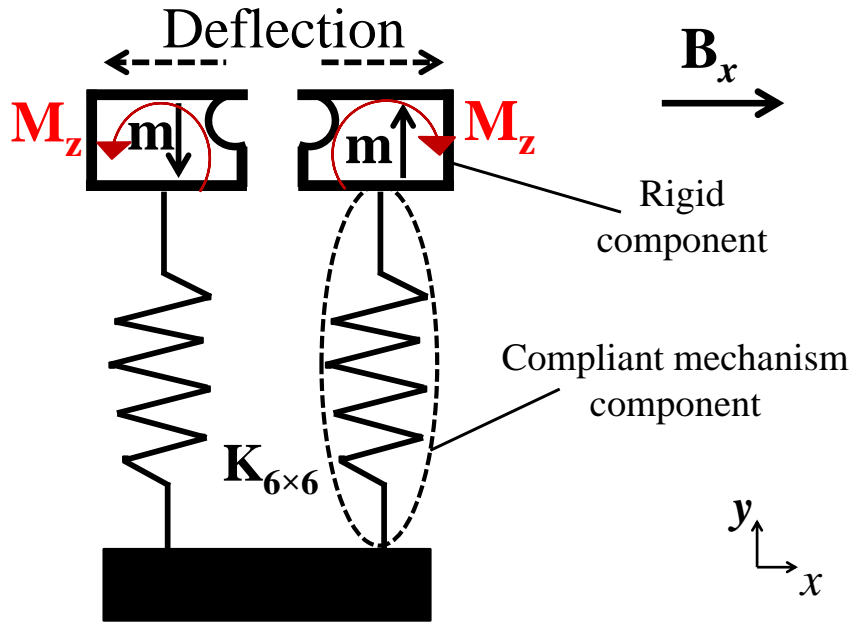
Figure 3.4: The conceptual design of the μ-gripper. The gripper has two arms and each arm has a rigid and a compliant mechanism component. The compliant mechanism component is represented by a spring with stiffness in all 6 axes. The rigid component is magnetized in the body frame's y-axis direction and it will experience a torque about the z-axis when a magnetic field that is along the body frame's x-axis is applied. Ideally, upon actuated, the compliant mechanism component should have a large translational deflection along the body frame's x-axis. Furthermore, the compliant mechanism component should have high stiffness for all other directions.
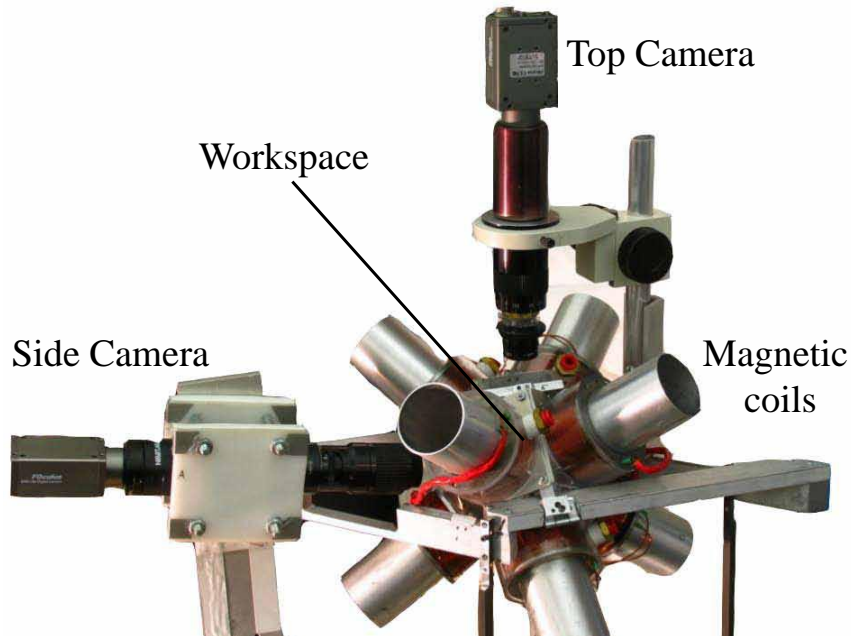
Figure 3.5: The magnetic coil system that is used to actuate the μ-grippers. The μ-grippers are located within the workspace indicated in the figure. There are two cameras - side and top, to provide vision feedback.

electromagnetic coil system is composed by eight independent coils that function as electromagnets. By varying the electrical current of each coil, we can independently control the magnetic field and its spatial gradients in the workspace, allowing us to in turn control the μ-gripper. Other than the desired compliance, the μ-gripper should exhibit high stiffness in all other directions so that it can easily reject mechanical disturbances when it is grabbing and transporting other objects. This implies that the flexure has only 1-degree-of-freedom.

Based on the degree-of-freedom of the flexure, we have used the Grübler equation [81] to select two appropriate traditional mechanisms as seeds. The selected seeds are the 6-bar Watt- and Stephenson-Chains, and their topologies can be seen in Fig. 3.6(b). These mechanisms are chosen because they can be constrained to generate compliant mechanisms with symmetrical features that can help to reduce the parasitic compliances.

43
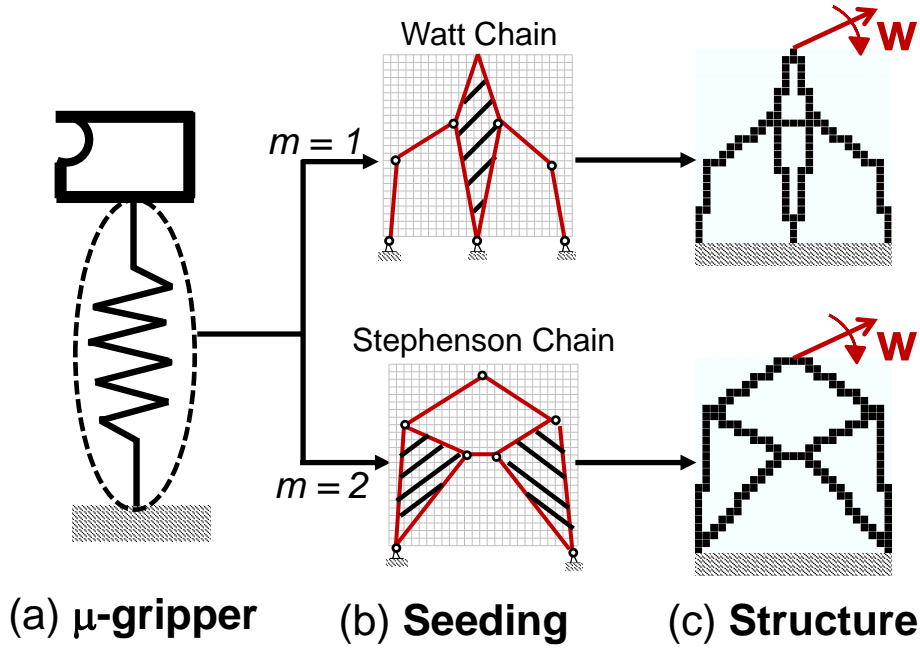
Figure 3.6: Implementing the mechanism-based approach on the (a) μ-gripper. (b) shows the design domain of the flexure being discretized into a mesh of 25×25 identical finite elements. The area of the design domain is 1.25 mm $\times$ 1.25 mm. Based on the valuable of m, different seeds will be used to represent the flexure. A Watt chain seed is used when $m = 1$ while a Stephenson chain is used when $m = 2$. (c) shows the obtained structure created via their corresponding seed.

During the optimization process, the topologies can be evolved by varying the position of the seeds' link tip. The topology of the seeds can also be changed if any link lengths are reduced to zero. As the position of the links' tip are the design variables, they are encoded in G.A.'s chromosomes. To reduce computational resources, we represent the linkages of the seeds with straight lines in this test problem (first way of mapping).

The design domain for each of the μ-gripper's compliant mechanism component is bounded within an area of 1.25 mm $\times$ 1.25 mm with 50 μm thickness. The design domain's dimensions is chosen to facilitate fabrication via photolithography and replica molding. The utilized material is a flexible elastomer material (ST-1087, BJB Enterprises), with Young's modulus and Poisson ratio estimated

to be 9.8 MPa and 0.45 respectively. The design domain is discretized into a mesh of 25×25 identical 20-node quadratic finite element where each element can only be either solid or void, and they are all initially selected as void.

The stiffness characteristics of the μ-gripper can be evaluated by using FEA to determine the deformation characteristics of its loading point (indicated by the point where an arbitrary wrench, $\mathbf{w}$, is applied on the gripper (see Fig. 3.6)). To implement FEA, we shall first define the translational deformation of any arbitrary point within a finite element, $\vec{u}$, to be the product of the shape function matrix, $\mathbf{N}$, and the nodal deformation vector $\mathbf{u}_e$:

$$\vec{u} = \begin{bmatrix} u \\ v \\ w \end{bmatrix} = \mathbf{N}\mathbf{u}_e$$

$$\text{where} \quad \mathbf{N} = \begin{bmatrix} N_1 & 0 & 0 & ... & 0 \\ 0 & N_1 & 0 & ... & 0 \\ 0 & 0 & N_1 & ... & N_{20} \end{bmatrix} \quad \text{and} \quad \mathbf{u}_e = \begin{bmatrix} u_1 \\ v_1 \\ w_1 \\ \vdots \\ w_{20} \end{bmatrix} \quad (3.4)$$

Note that u, v and w represent the deformation in the $x-$, $y-$ and $z-$axis respectively. Subsequently, the strain vector of the point, ϵ_e, can be obtained by partial differentiating corresponding rows in Eq. (3.4):

45

$$\boldsymbol{\epsilon}_e = \begin{bmatrix} \frac{\partial u}{\partial x} \\[6pt] \frac{\partial v}{\partial y} \\[6pt] \frac{\partial w}{\partial z} \\[6pt] \frac{\partial v}{\partial z} + \frac{\partial w}{\partial y} \\[6pt] \frac{\partial u}{\partial z} + \frac{\partial w}{\partial x} \\[6pt] \frac{\partial v}{\partial x} + \frac{\partial u}{\partial y} \end{bmatrix} = \mathbf{B}\mathbf{u}_e,$$

$$\text{where } \mathbf{B} = \begin{bmatrix} \frac{\partial}{\partial x} & 0 & 0 \\[6pt] 0 & \frac{\partial}{\partial y} & 0 \\[6pt] 0 & 0 & \frac{\partial}{\partial z} \\[6pt] 0 & \frac{\partial}{\partial z} & \frac{\partial}{\partial y} \\[6pt] \frac{\partial}{\partial z} & 0 & \frac{\partial}{\partial x} \\[6pt] 0 & \frac{\partial}{\partial x} & \frac{\partial u}{\partial y} \end{bmatrix} \begin{bmatrix} N_1 & 0 & 0 & ... & 0 \\[6pt] 0 & N_1 & 0 & ... & 0 \\[6pt] 0 & 0 & N_1 & ... & N_{20} \end{bmatrix}. \qquad (3.5)$$

Note that the matrix $\mathbf{B}$ is the commonly used deformation matrix in FEA. By using Hooke's law, the stress vector at that point, $\boldsymbol{\tau}_e$, can be expressed as:

$$\boldsymbol{\tau}_e = \mathbf{D}\boldsymbol{\epsilon}_e = \mathbf{D}\mathbf{B}\mathbf{u}_e,$$

$$\text{where } \mathbf{D} = \frac{E}{(1+v)(1-2v)} \begin{bmatrix} 1-v & v & v & 0 & 0 & 0 \\[6pt] v & 1-v & v & 0 & 0 & 0 \\[6pt] v & v & 1-v & 0 & 0 & 0 \\[6pt] 0 & 0 & 0 & \frac{1-2v}{2} & 0 & 0 \\[6pt] 0 & 0 & 0 & 0 & \frac{1-2v}{2} & 0 \\[6pt] 0 & 0 & 0 & 0 & 0 & \frac{1-2v}{2} \end{bmatrix}. \qquad (3.6)$$

Note that $\mathbf{D}$ is also known as the compliance matrix in solid mechanics. The element's total strain energy, S_e, is:

$$S_e = \frac{1}{2} \iiint \boldsymbol{\tau}_e^{\mathrm{T}} \boldsymbol{\epsilon}_e \ \mathrm{d}V = \frac{1}{2} \mathbf{u}_e^{\mathrm{T}} \left[\iiint \mathbf{B}^{\mathrm{T}} \mathbf{D} \mathbf{B} \mathrm{d}V \right] \mathbf{u}_e = \frac{1}{2} \mathbf{u}_e^{\mathrm{T}} \mathbf{K}_{\mathrm{FE}} \mathbf{u}_e,$$

$$\text{where} \ \ \mathbf{K}_{\mathrm{FE}} = \left[\iiint \mathbf{B}^{\mathrm{T}} \mathbf{D} \mathbf{B} \mathrm{d}V \right]. \tag{3.7}$$

The variable V represents the volume of the finite element and $\mathbf{K}_{\mathrm{FE}}$ represents the stiffness matrix for one element. The FEA global $n \times n$ stiffness matrix for the gripper, $\mathbf{K}_{\mathrm{gripper}}$, can then be obtained by summing all elements' stiffness matrix:

$$\mathbf{K}_{\mathrm{gripper}} = \sum_{i=1}^{\text{all elements}} \left(s_i \mathbf{K}_{\mathrm{FE},i} \right). \tag{3.8}$$

The variable s represents the state of the finite element, if element i is solid, s_i = 1; if it is void, $s_i = 10^{-6}$ (to prevent numerical instabilities). The loading point will be loaded with six unit wrenches, i.e. three unit forces along the x-, y- and z-axes, and three unit torques about the x-, y- and z-axes. The corresponding work functions for these wrenches are simply the deformation of the loading point that is parallel to the unit wrench. Note that the rotational deformation of the loading point can be derived from the infinitesimal element. Using Fig. 3.7 as illustration aid, the angular displacement in the z-direction of the loading point is:

$$\theta_z = \frac{1}{2}(\alpha - \beta) = \frac{1}{2}(\frac{\partial v}{\partial x} - \frac{\partial u}{\partial y})$$
$$\therefore \theta_z = \frac{1}{2} \left[\sum_{i=1}^{8} \left(\frac{\partial N_i}{\partial x} v_i - \frac{\partial N_i}{\partial y} u_i \right) \right]. \tag{3.9}$$

Likewise, the rotational displacement in the x and y-axes can be obtained as:

47
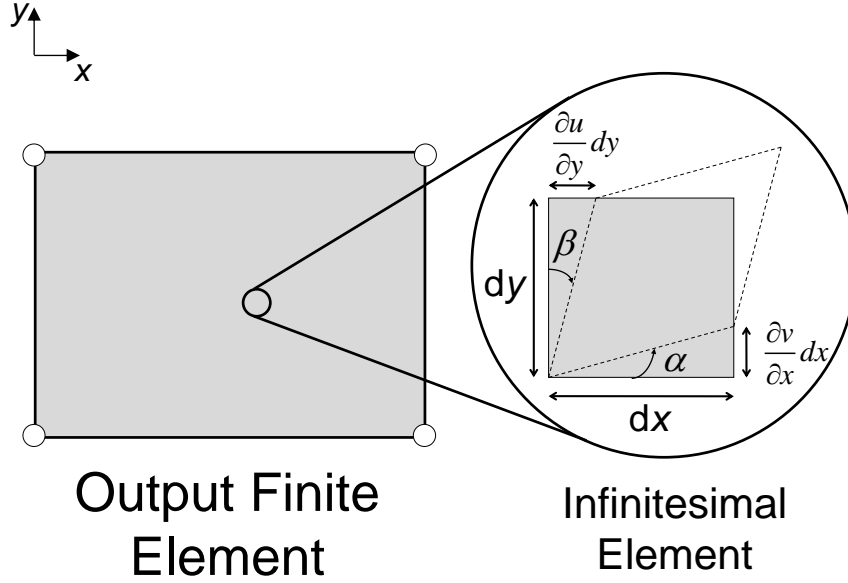
Figure 3.7: A graphical representation of rotary deflection for any point within the finite element. By zooming into the infinitesimal element of a finite element, the average rotary deflections about the z-axis of any given point is $\frac{1}{2}(\alpha - \beta)$.

$$
\begin{aligned}
\theta_x &= \frac{1}{2}\left[\sum_{i=1}^{8}\left(\frac{\partial N_i}{\partial y}w_i - \frac{\partial N_i}{\partial z}v_i\right)\right] \\
\theta_y &= \frac{1}{2}\left[\sum_{i=1}^{8}\left(\frac{\partial N_i}{\partial z}u_i - \frac{\partial N_i}{\partial x}w_i\right)\right].
\end{aligned}
\tag{3.10}
$$

The translation and rotational work functions are represented by $\phi_{\text{T},j}$ and $\phi_{\text{R},j}$, $j \in [x, y, z]$, respectively. The global nodal deformation vector is represented by $\mathbf{u}_{\text{gripper}}$ and thus the six work functions are expressed as:

$$
\begin{aligned}
\phi_{\text{T},x} &= \mathbf{u}_{\text{gripper}}^{\text{T}}\mathbf{f}_x & \phi_{\text{R},x} &= \mathbf{u}_{\text{gripper}}^{\text{T}}\mathbf{m}_x \\
\phi_{\text{T},y} &= \mathbf{u}_{\text{gripper}}^{\text{T}}\mathbf{f}_y & \phi_{\text{R},y} &= \mathbf{u}_{\text{gripper}}^{\text{T}}\mathbf{m}_y \\
\phi_{\text{T},z} &= \mathbf{u}_{\text{gripper}}^{\text{T}}\mathbf{f}_z & \phi_{\text{R},z} &= \mathbf{u}_{\text{gripper}}^{\text{T}}\mathbf{m}_z.
\end{aligned}
\tag{3.11}
$$

By partial-differentiating the work functions with respect to the global nodal deflections, the six loading vectors are represented in FEA format as $\mathbf{f}_x$, $\mathbf{f}_y$, $\mathbf{f}_z$, $\mathbf{m}_x$, $\mathbf{m}_y$ and $\mathbf{m}_z$, respectively. After applying the boundary conditions, the corresponding deformation vectors are obtained by pre-multiplying the six loading vectors with the structure's inverse stiffness matrix. The six 6×1 position vectors which describe the position and orientation deformations at the loading point can be obtained by using N_i, and u_i, v_i and w_i from the corresponding global nodal deformation vectors. This is represented by pre-multiplying the six global nodal deformations vectors with a constant $6 \times n$ matrix $\mathbf{A}$.

$$\therefore \mathbf{C}_{\text{gripper, } 6\times6} = \mathbf{A}\mathbf{K}_{\text{gripper}}^{-1}[\mathbf{f}_x \ \ \mathbf{f}_y \ \ \mathbf{f}_z \ \ \mathbf{m}_x \ \ \mathbf{m}_y \ \ \mathbf{m}_z]. \tag{3.12}$$

The matrix, $\mathbf{C}_{\text{gripper, } 6\times6}$, represents the compliance matrix of the compliant mechanism. The six columns of the matrix represent the rigid-body deflections induced by corresponding loadings. The first three rows of $\mathbf{C}_{\text{gripper, } 6\times6}$ represent the translational deflection while the last three rows represent the rotary deflection. As the actuating compliance of the μ-gripper is represented by C_{61} in $\mathbf{C}_{\text{gripper, } 6\times6}$, we will use the following fitness function to optimize its stiffness characteristics:

$$\text{minimize } F_{\mathbf{gripper}} = \frac{C_{51}C_{15} \left[\prod_{\delta=1}^{3} C_{\delta\delta}\right] \left[\prod_{\eta=4}^{6} C_{\eta\eta}^2\right]}{|C_{61}|^8} \tag{3.13}$$

$$\text{subject to: } \mathbf{K}_{\text{gripper}}\mathbf{u}_{\text{gripper}} = \mathbf{f}_{\text{gripper}},$$

The numerator of the fitness function is composed by the product of prominent off-axis compliances that will be minimized by the optimization process. The rotary parasitic compliances, i.e. C_{44}, C_{55} and C_{66}, are regarded as more

49

important for robust gripper operations, thus they have a higher exponential to represent a greater emphasis. The denominator of the fitness function aims to maximize the actuating compliance, C_{61}, and its exponent is raised to eight because there are eight different components in the numerator. The governing FEA equation for evaluating the stiffness characteristics of the μ-gripper is represented by the equality constraint. This optimization process is conducted with a population of 100 chromosomes. Each of the chromosomes include the design variables m, the position of the links' tip. The optimization took 4-5 hours to converge within 50 generations as shown in Fig. 3.8 and the solution is shown in Fig. 3.9(b). Thanks to the nature of the mechanism-based approach, the obtained solution did not have any 'grey' or disconnected solid elements. Furthermore, it is interesting to note that the topology has evolved from the six-bar seeds into a non-uniform thickness beam; this implies that the search space of the mechanism-based approach is not limited by the topologies of the initial seeds. Finally, by smoothening the jagged edges to remove the stress concentration, we obtained the final design of the μ-gripper (Fig. 3.9(c)).

The performance of the gripper is evaluated by comparing it with a thin-beam design that is developed via human intuition (Fig. 3.9(d)). The thickness of the thin-beam was adjusted to match the actuating compliance with the gripper; this allows an easier comparison between these two designs. The $\mathbf{C}_{\text{gripper},6\times6}$ of the optimized design, $\mathbf{C}_{\text{Opt},6\times6}$, and the intuitively-designed beam-type μ-gripper, $\mathbf{C}_{\text{Int},6\times6}$, are evalu-

ated via FEA to be:

$$
\mathbf{C}_{\text{Opt},6\times6} =
\begin{bmatrix}
19.3 & & & & & \\
0 & 3.57 \times 10^{-2} & & & \mathbf{SYM} & \\
0 & 0 & 7.81 & & & \\
0 & -530 & 8.06 \times 10^3 & 1.17 \times 10^7 & & \\
900 & 0 & 0 & 0 & 1.87 \times 10^7 & \\
-1.71 \times 10^4 & 0 & 0 & 0 & 0 & 1.77 \times 10^7
\end{bmatrix}
$$

$$
\mathbf{C}_{\text{Int},6\times6} =
\begin{bmatrix}
14.0 & & & & & \\
0 & 6.22 \times 10^{-2} & & & \mathbf{SYM} & \\
0 & 0 & 9.11 & & & \\
0 & -941 & 1.12 \times 10^4 & 2.00 \times 10^7 & & \\
1.72 \times 10^3 & 0 & 0 & 0 & 3.55 \times 10^7 & \\
-1.71 \times 10^4 & 0 & 0 & 0 & 0 & 3.04 \times 10^7
\end{bmatrix}
$$

$$(3.14)$$

A superior design is one that has more components with lower magnitude in their compliance matrix as this implies that it can better reject disturbances. Based on the compliance matrices for both designs, it is apparent that the optimal structure have better stiffness characteristics as eight out of nine components are better(smaller). Some of these components are even approximately two times better - demonstrating the effectiveness of the mechanism-based approach.

3.2.1 Experimental results for the μ-gripper

In order to evaluate the accuracy of the FEA comparison in Eq. (3.14), an up-scale prototype had been constructed as shown in Fig. 3.11(a). We had selected a larger prototype because it would be easier to measure its deflections and input
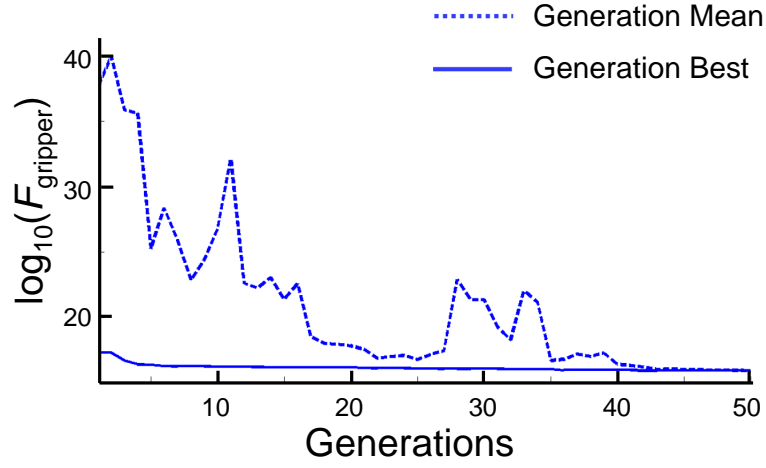
Figure 3.8: The convergence plot for the μ-gripper. The optimization process is shown to converge as the fitness value for the generation mean and generation best converges to one another eventually.
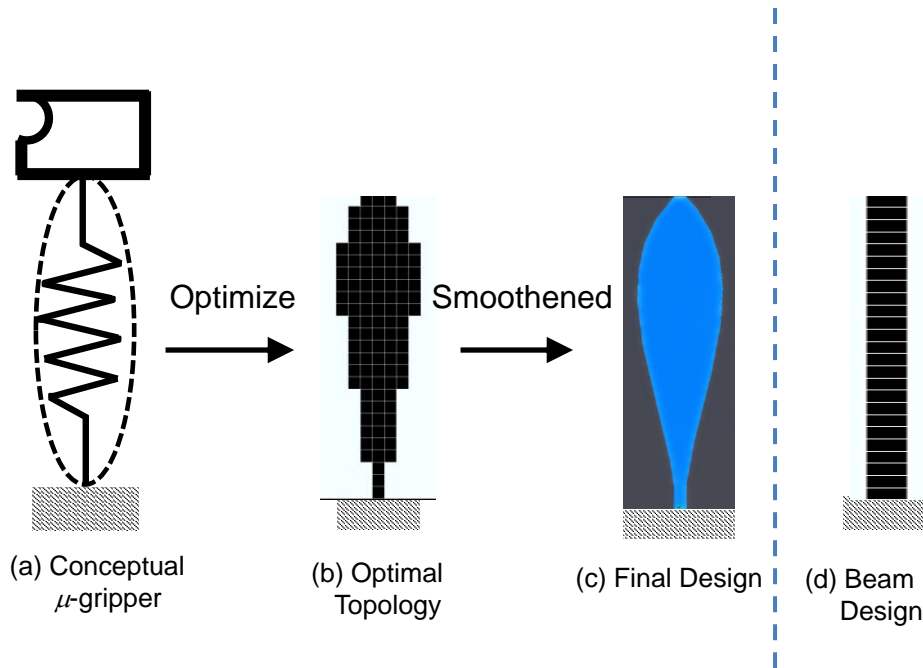
Figure 3.9: A comparison between the optimized gripper with an human-intuitively created beam design. (b) is the optimized gripper. (c) smoothen the sharp corners of (b) to prevent stress concentration. (d) is the human-intuitively created beam design.
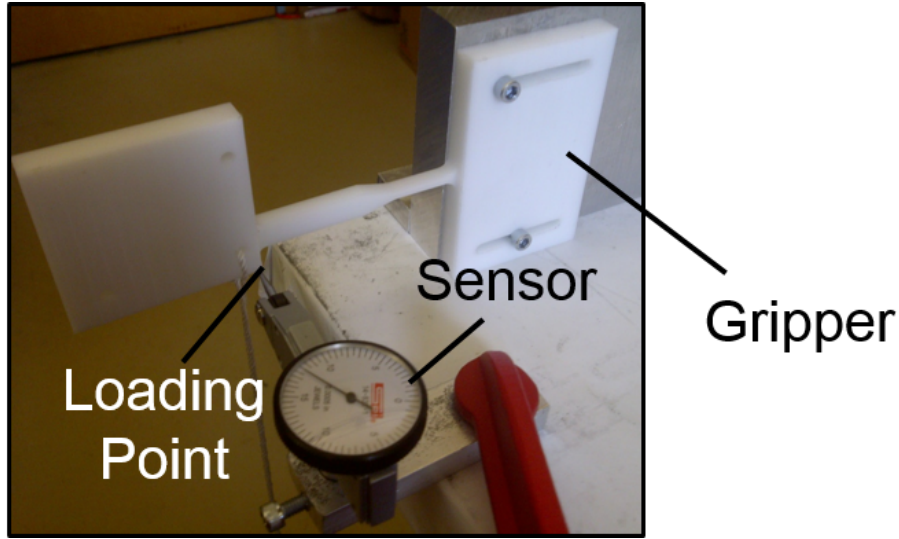
Figure 3.10: The experimental set up for the large-scale prototype. After applying dead weights at the loading point of the prototype, the deflection of the gripper will be measured by the sensor (dial).

forces experimentally. As the accuracy of the FEA will not be affected by the size of the prototype, this implies that if the compliances of the up-scale prototype can match its FEA prediction, the FEA comparison for the μ-grippers' stiffness characteristics will be valid too.

The up-scale prototype was constructed with acetal, and its Young's modulus and Poisson ratio were estimated to be 3.1 GPa and 0.45, respectively. Precise force loading was applied on the prototype by hanging calibrated weights, and the induced deflections were measured by a dial gauge indicator. The compliances of the prototype were determined experimentally from the slope of their load against deflection plots. By changing the orientation of the prototype and the location of the dial, different compliances could be evaluated. Eight compliances, C_{11}, C_{22}, C_{33}, C_{44}, C_{55}, C_{66}, C_{61} and C_{43} had been validated. For all the evaluated compliances, three sets of data were collected and each set had 5 data points. As an example, Fig. 3.11(b) showed the deflection plot for the prototype's actuating compliance, and the complete experimental data and simulation results
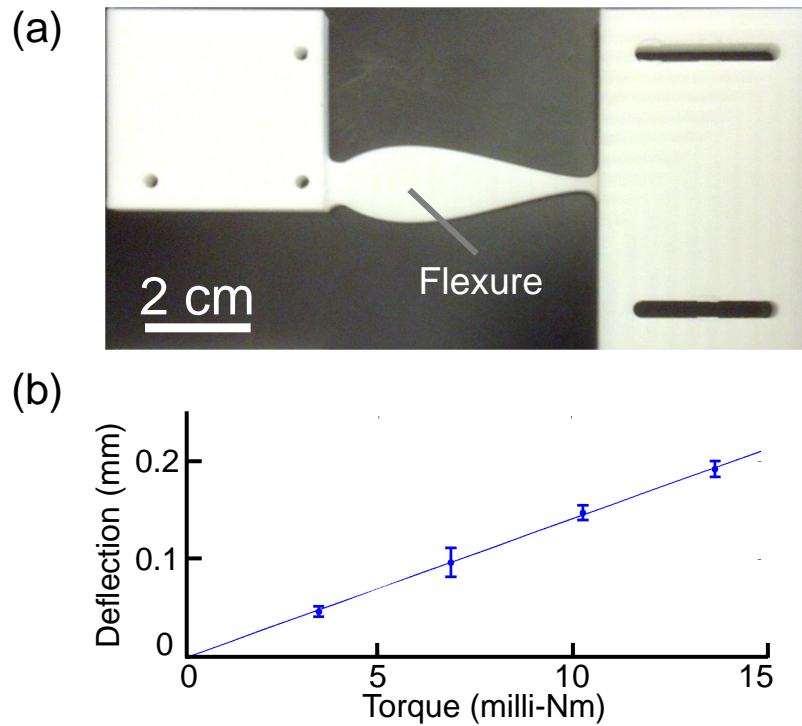
Figure 3.11: The experimental result for the large-scale prototype shown in (a). (b) Experimental data for the actuating compliance of the prototype is shown as an example. The slope of the plot represents the experimental actuating compliance is -14.1×10^{-3} m/(Nm) and it agrees with the FEA prediction of -16.1×10^{-3} m/(Nm) within 12% deviation. Each datapoint represents the mean from three measurements, and error bars indicate standard deviation.

were shown in the following two equations:

$$\mathbf{C}_{\text{upscale, experiments, } 6\times6} = \begin{bmatrix} 0.98 \times 10^{-3} & & & & & \\ 0 & 1.50 \times 10^{-6} & & & & \\ 0 & 0 & 0.434 \times 10^{-3} & & & \\ 0 & 0 & 8.56 \times 10^{-3} & 0.27 & & \\ 0 & 0 & 0 & 0 & 0.402 & \\ -16.1 \times 10^{-3} & 0 & 0 & 0 & 0 & 0.35 \end{bmatrix}$$

(3.15)

$$\mathbf{C}_{\text{upscale, FEA, } 6\times6} = \begin{bmatrix} 0.834 \times 10^{-3} & & & & & \\ 0 & 1.85 \times 10^{-6} & & & & \\ 0 & 0 & 0.471 \times 10^{-3} & & & \\ 0 & 0 & 8.40 \times 10^{-3} & 0.335 & & \\ 0 & 0 & 0 & 0 & 0.343 & \\ -14.1 \times 10^{-3} & 0 & 0 & 0 & 0 & 0.423 \end{bmatrix}.$$

(3.16)

Based on the experimental results, the maximum deviation between the experiments and FEA predictions was 20%, and the mean deviation was computed to be 15%. The small deviation between the experiments and predictions for the upscale prototype suggested that the comparison made in Eq. (3.14) for the at-scale μ-gripper was accurate as well - suggesting the superior stiffness characteristics of the optimal compliant mechanism over the thin-beam design.

While we did not evaluate the stiffness characteristics of the at-scale grippers, we had constructed these grippers with photolithography and replica molding. To fabricate μ-grippers from soft elastomer with included magnetic particles, a
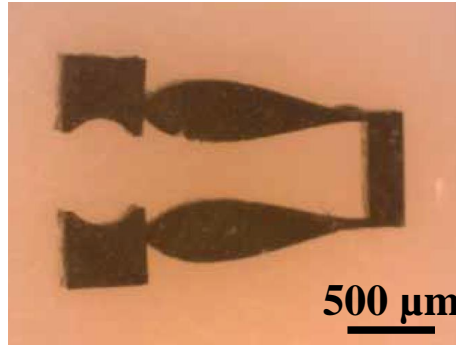
Figure 3.12: At-scale fabricated μ-grippers with optimized flexure designs.

replica molding technique was used. The process included shape definition by photolithography, replica molding to achieve flexible elastomer gripper shapes, and a magnetization process. The μ-grippers were made from a flexible elastomer material (ST-1087, BJB Enterprises) to allow for larger deflections given the same magnetic actuation. By pouring the uncured liquid elastomer that is mixed with magnetic particles (NdFeB) into the mold, the desired shape of the gripper can be fabricated after the elastomer cured. Because the cured elastomer encompasses the magnetic particles, it would be possible to magnetize the μ-gripper and allow it to be responsive towards magnetic actuation. The design required that each gripper tip be magnetized in opposite directions. This could be accomplished by deforming the μ-gripper arms $90°$ prior to exposing the gripper with a large magnetizing field (~ 1.2 T). This would magnetize the $\mu-$gripper, allowing it to open and close its rigid components by adjusting the magnitude of the magnetic field ($\mathbf{B}_x$) shown in Fig. 3.4. Note that when the magnetic field is applied, the rigid component will generate a magnetic torque that will in turn bend and deform the compliant component. The manufactured μ-gripper was shown in Fig. 3.12.

When the fabricated μ-gripper was placed in the magnetic coil system, it

56
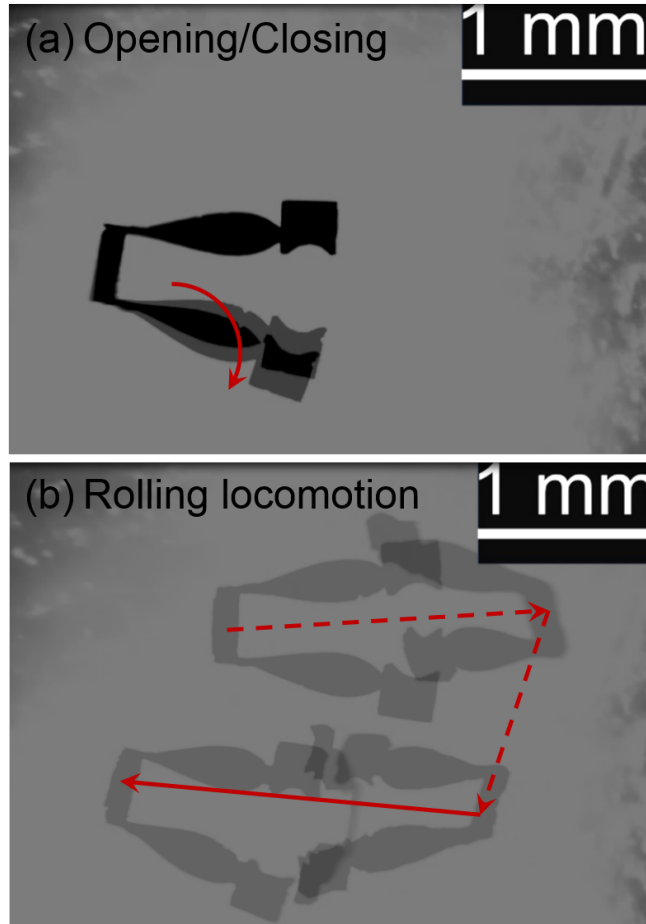
Figure 3.13: At-scale fabricated μ-grippers (a) opening and closing its grippers and (b) rolling on the substrate.

could move on a planar surface by using a rolling locomotion. This locomotion could be made possible because its base (represented by the ground in Fig. 3.9) was also magnetized and could respond to the magnetic actuation. When the μ-gripper was subjected to a magnitude fields of 10 mT, it could create gripping motions by making the 2D deflection indicated in Fig. 3.4. Some snapshots during the actuation are shown in Fig. 3.13 .

3.3 Summary

This chapter introduces a new topological optimization algorithm known as the mechanism-based approach. In contrast to existing topological optimization techniques, this proposed algorithm is able to eliminate infeasible designs that have either disconnected solid elements or ambiguous 'grey' elements, while having a flexible way to change the structure's topology during the optimization process. The mechanism-based approach maps the geometrical characteristics of a traditional mechanism as a seed to represent the topology of a compliant mechanism. As the links of the seed are always physically connected, the obtained topology will never produce disconnected solid elements. Furthermore, as the selection of the solid elements is done in a discrete manner, the possibility of having ambiguous "grey" elements is eliminated. Topologies of the compliant mechanism are not restrained by the seed as even the seed can be evolved during the optimization process. This is demonstrated during the synthesis process for the μ-gripper as the seed changes from six-bar linkages into a beam with non-uniform thickness. Convergence plot for the synthesis of the μ-gripper had also indicated that the mechanism-based approach can converge smoothly. Furthermore, the obtained design has shown improvement over an intuitive design, illustrating the potential of the proposed algorithm. Thus, the advantages of the mechanism-based approach can be summarized as:

- The generated topology does not have disconnected solid elements

- The optimization procedure was done in a discrete manner, thus there are no ambiguous "grey" elements

- Convergence plot indicates that the algorithm can converge and evolve gradually

- By using a global optimization solver, G.A., the mechanism-based approach has a higher probability to arrive a global solution compared to other gradient-based techniques

- The topology of the compliant mechanism is not fixed by the seed, even the 'topology' of the seed can be changed

- By using two curves to represent one link of the seed, it is possible to add holes within the linkage representation

The disadvantage of this algorithm is that the optimization procedure requires more computational power and time. However, as the design process is generally conducted as off-line programming, computational time is not a critical factor.

Chapter 4

Synthesis of a 3<u>P</u>PR Flexure-based Parallel Mechanism

This chapter further investigates the effectiveness of the proposed topological optimization algorithm - the mechanism-based approach. In particular, the algorithm will create compliant joints that can be assembled into a $X - Y - \theta_z$ FPM. The effectiveness of the algorithm will be evaluated by comparing the synthesized FPM's stiffness characteristics with a similar FPM that is composed by traditional compliant joints. We have selected the synthesis of a $X - Y - \theta_z$ FPM to illustrate the effectiveness of our method because this structure has the potential to be deployed across many applications pertaining to micro/nano-alignment, biomedical science, SEM, x-ray lithography and many other similar technologies [9, 50, 51]. The chapter is organized as follows: Section 4.1 introduces the overall configuration of the FPM and Section 4.2 will present the synthesis process for the compliant joints. This is followed by Section 4.3 where the joints will be assembled into the FPM. Lastly, section 4.4 will provide a summary for the chapter.

4.1 Overall Configuration

Based on the rigid-body-replacement method, there are three possible parallel-kinematic configurations that can realize a $X - Y - \theta_z$ FPM. The three configurations are the 3-legged revolute-revolute-revolute (3RRR), the 3-legged prismatic-revolute-revolute (3PRR), and the 3-legged prismatic-prismatic-revolute (3PPR). We will select the 3PPR configuration because compliant prismatic joints are generally more deterministic than the compliant revolute joints. The schematic of the 3PPR architecture is shown in Fig. 4.1 where the end-effector is articulated by three identical parallel sub-chains that are arranged in a rotary symmetrical manner. Each sub-chain has an active prismatic joint (P) that is serially connected to a passive prismatic-revolute (PR) joint. The active P joint is placed nearer to the fixed base to prevent the weight of the actuator from contributing to the overall moving masses of the FPM.

Based on Fig. 4.1, we fix a global frame, {g}, at the center of the mechanism when it is at the home pose. Next, we attach a mobile frame, {m}, to the moving platform where it coincides with {g} when the mechanism is at the home pose. This frame can have an arbitrary translational displacement, $\mathbf{r}_e = [xe \quad ye]^T$, and a rotational displacement about the z-axis, θ_z. A corresponding local frame, i.e. {1}, {2} and {3}, will be assigned to each sub-chain, and their origins are fixed at the home position of their active P joint. The orientation of the frames {1}, {2} and {3} have a relative z-axis rotation angle of $[\alpha_1, \quad \alpha_2, \quad \alpha_3] = [\pi/3, \quad \pi, \quad -\pi/3]$ from the global frame, respectively.

The inverse kinematics analysis that correlates the displacement of the active P joints with the end-effector's motion can be determined by using simple vector analyses. As these analyses are similar for all the sub-chains, we will only analyze sub-chain 1 as an example (see Fig. 4.2). In this figure, the magnitude for the

62
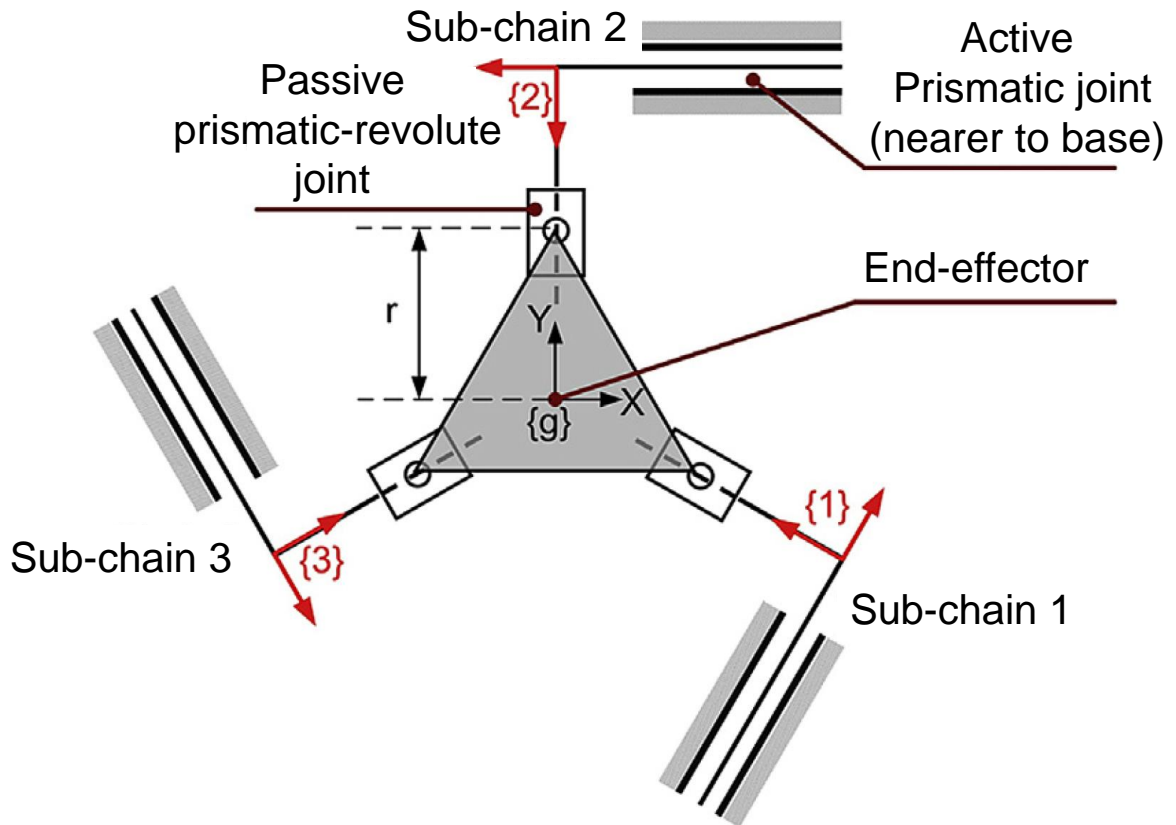
Figure 4.1: The selected overall configuration for the FPM: A 3PPR configuration. The FPM has three symmetrical sub-chains that are arranged in a rotary symmetrical manner. Each sub-chain consists of an active P joint and a passive PR joint. The active joint is placed closer to the fixed base. The variable r represents the distance between the end-effector and the PR joint.
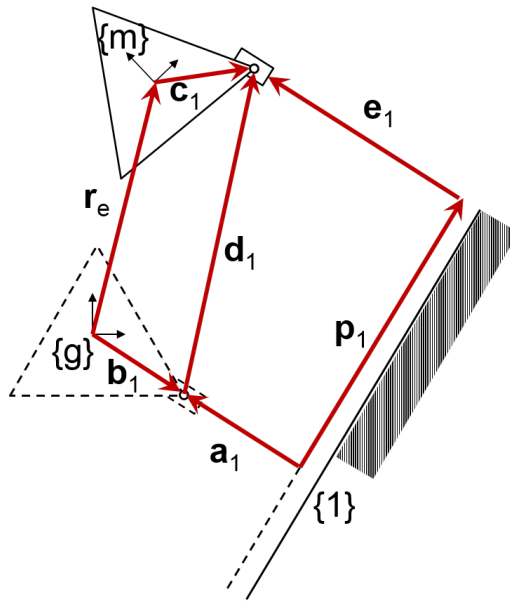
Figure 4.2: Using sub-chain 1 as an example to derive the inverse kinematics of the FPM. After the end-effector is displaced translationally with $\mathbf{r}_e$ and have a rotational deflection of θ_z, we can use the vectors indicated here to determine the magnitude of $\mathbf{p}_1$. For simplicity, we have also assigned a global frame indicated by $\{g\}$, a mobile frame $\{m\}$ that is attached to the end-effector and a local frame for sub-chain 1 (indicated by $\{1\}$).

vector $\mathbf{b}_i$ will be r while the magnitude of the active $\underline{\text{P}}$ joint's displacement is represented by p_1. To make our analysis clearer, we will put superscripts for the vectors to indicate their prescribed frame. For example, a vector $^{\{g\}}\mathbf{r}$ means that this vector is viewed in the global frame. According to Fig. 4.2, the vector $\mathbf{d}_1$ can be computed to be:

$$^{\{g\}}\mathbf{d}_1 = ^{\{g\}}\mathbf{r}_e + \mathbf{R}_z(\theta_z)(^{\{m\}}\mathbf{c}_1) - ^{\{g\}}\mathbf{b}_1 \tag{4.1}$$

When the mechanism is in its home pose, $^{\{m\}}\mathbf{c}_1 = ^{\{g\}}\mathbf{b}_1$ and $\mathbf{R}_z$ is a standard rotational matrix give as:

$$\mathbf{R}_z = \begin{bmatrix} \cos(\theta_z) & -\sin(\theta_z) & 0 \\ \sin(\theta_z) & \cos(\theta_z) & 0 \\ 0 & 0 & 1 \end{bmatrix}. \tag{4.2}$$

Since both the vectors $^{\{1\}}\mathbf{a}_1$ and $^{\{1\}}\mathbf{e}_1$ do not have x-axis components and $^{\{1\}}\mathbf{p}_1$ does not have a y-axis component, the calculation of p_1 is best done in frame 1. Therefore, we can simply compute p_1 by:

$$^{\{1\}}\mathbf{p}_1 = ^{\{1\}}\mathbf{a}_1 + [\mathbf{R}_z^{\mathrm{T}}(\alpha_1)]\,^{\{g\}}\mathbf{d}_1 - ^{\{1\}}\mathbf{e}_1$$

$$\therefore \ ^{\{1\}}p_1 = \frac{x_e}{2} + \frac{\sqrt{3}}{2}y_e + r\sin(\theta_z) \approx \frac{x_e}{2} + \frac{\sqrt{3}}{2}y_e + r\theta_z \tag{4.3}$$

Using similar analyses for sub-chains 2 and 3, the relationship between the end-effector's output motion, x, y, and θ_z, and the displacement of the active prismatic joints, p_1, p_2, and p_3, can be summarized as:

65

$$\begin{bmatrix} p_1 \\ p_2 \\ p_3 \end{bmatrix} = \begin{bmatrix} \frac{1}{2} & \frac{\sqrt{3}}{2} & r \\ -1 & 0 & r \\ \frac{1}{2} & -\frac{\sqrt{3}}{2} & r \end{bmatrix} \begin{bmatrix} x \\ y \\ \theta_z \end{bmatrix}. \tag{4.4}$$

4.2 Synthesizing compliant PR and P̲ joints

Based on the selected 3P̲PR FPM configuration, there are two types of compliant joints - the PR and P joints. Thus, in this section, we will show that they can be synthesized via the mechanism-based approach.

4.2.1 Synthesis of a PR compliant joint

An ideal PR compliant joint can provide a large x-axis translation and also a large z-axis rotation when its loading point is subjected to a F_x force and a M_z torque, respectively. Mathematically, this implies that its actuating compliances, C_{11} and C_{66}, should be maximized while other off-axis components in the $\mathbf{C}_{PR,6\times6}$ must be minimized to achieve optimal stiffness properties. As the PR joint has 2 degrees-of-freedom (2 actuating compliances), we have selected a five-bar linkage as the seed for the mechanism-based approach. The coupler point of the seed, which is also its loading point, is constrained to move along the top row elements while two fixed points were located at the base (Fig. 4.3(a)).

The synthesis of the PR compliant joint was broken down into two stages to reduce the computational time. The first stage was performed through a coarse mesh while the second stage will further refine the design with a fine mesh. In both stages, the design domain of the PR joint is constrained within a 50 mm × 20 mm × 10 mm volume, which is discretized into a mesh of 3-D 8-node bilinear finite elements. The utilized material is assumed to be aluminum, and its Young's

Modulus and Poisson ratio are estimated to be 71 GPa and 0.33, respectively. Thus, the stiffness matrices in FEA format for one finite element, $\mathbf{K}_{\text{FE},i}$, and the overall structure of the PR joint, $\mathbf{K}_{\text{PR},n \times n}$, are given as:

$$\mathbf{K}_{\text{FE},i} = \iiint \mathbf{B}^{\text{T}} \mathbf{D} \mathbf{B} \, \mathrm{d}V, \quad \mathbf{K}_{\text{PR},n \times n} = \sum_{i=1}^{\text{all elements}} s_i \mathbf{K}_{\text{FE},i}, \tag{4.5}$$

where s_i represents the state of the ith finite element in the design domain; $s_i = 1$ represents a solid element and $s_i = 10^{-6}$ represents a void element. To optimize the stiffness characteristics, we use the following fitness function for both stages:

$$\text{minimize } F_{\text{pr}}(\mathbf{x}_{\text{PR}}) = \frac{\Pi_{\delta=2}^{6} \Pi_{\eta=1}^{\delta} C_{\delta\eta}}{[C_{11}]^{19} [C_{66}]^{19}}, \tag{4.6}$$

$$\text{subject to: } \mathbf{K}_{\text{PR},n \times n} \mathbf{u}_{\text{PR},n \times 1} = \mathbf{f}_{\text{PR},n \times 1}.$$

The numerator in the fitness function aims to minimize the off-axis compliance components while the denominator will maximize the actuating compliances. As there are 19 off-axis stiffness, the C_{11} and C_{66} components are raised to the exponential of 19. It is necessary to raise the exponent to 19 because this allows the optimization process to minimize all the non-actuating compliance components while still allowing the actuating compliance to be maximized. The vector $\mathbf{x}_{\text{PR}}$ represents the variables for the mechanism-based approach and the equality constraint represents the FEA governing equation.

By evolving 500 chromosomes via 100 generations, the initial five-bar linkage gradually evolves into a three-bar topology during the first stage of optimization Fig. 4.3(b). During the optimization process, each chromosome includes the following design variables - the position of the links' tip and the curve parameters

shown in Section 3.1. While our method can simplify the seed's topology, we cannot increase its complexity. As a result, we cannot effectively evolve simple structures to mechanisms that have more complex topologies. By refining the design domain in the second stage of optimization, the optimized PR compliant joint is obtained after evolving 200 chromosomes via 50 generations (Fig. 4.3c). The optimal PR joint resembles a non-uniform beam supported by an arch. To further reduce the magnitude of the non-diagonal off-axis compliances, we adopted a symmetrical design for the final compliant PR joint (Fig. 4.3(d)). Both optimization processes have shown to converge as the mean fitness values in the convergence plots managed to converge with the best fitness values (Fig. 4.4). Note that the optimization process will stop after it cannot further evolve the best solution for another 20 generations or it had completed 100 generations of evolutions.

The obtained stiffness matrix of the compliant PR joint (inverse of $\mathbf{C}_{\text{PR}, \, 6\times6}$) is given as:

$$
\mathbf{K}_{\text{PR},6\times6} =
\begin{bmatrix}
1544 & & & & & \\
0 & 1.16 \times 10^7 & & & \textbf{SYM} & \\
0 & 0 & 4.89 \times 10^5 & & & \\
0 & 2.63 \times 10^4 & 0 & 232 & & \\
0 & 0 & 0 & 0 & 1.32 & \\
0 & 0 & 0 & 0 & 0 & 1.10
\end{bmatrix}.
\tag{4.7}
$$

4.2.2 Synthesis of $\underline{\mathbf{P}}$ joint

Similar to the synthesis of the PR joint, the active $\underline{\text{P}}$ compliant joint is synthesized via two optimization stages. In both stages, the Young's Modulus, Poisson ratio

68

(a) 5-bar linkage seed   (b) 3-bar structure   (c) Optimal PR joint

(d) The final design of PR joint
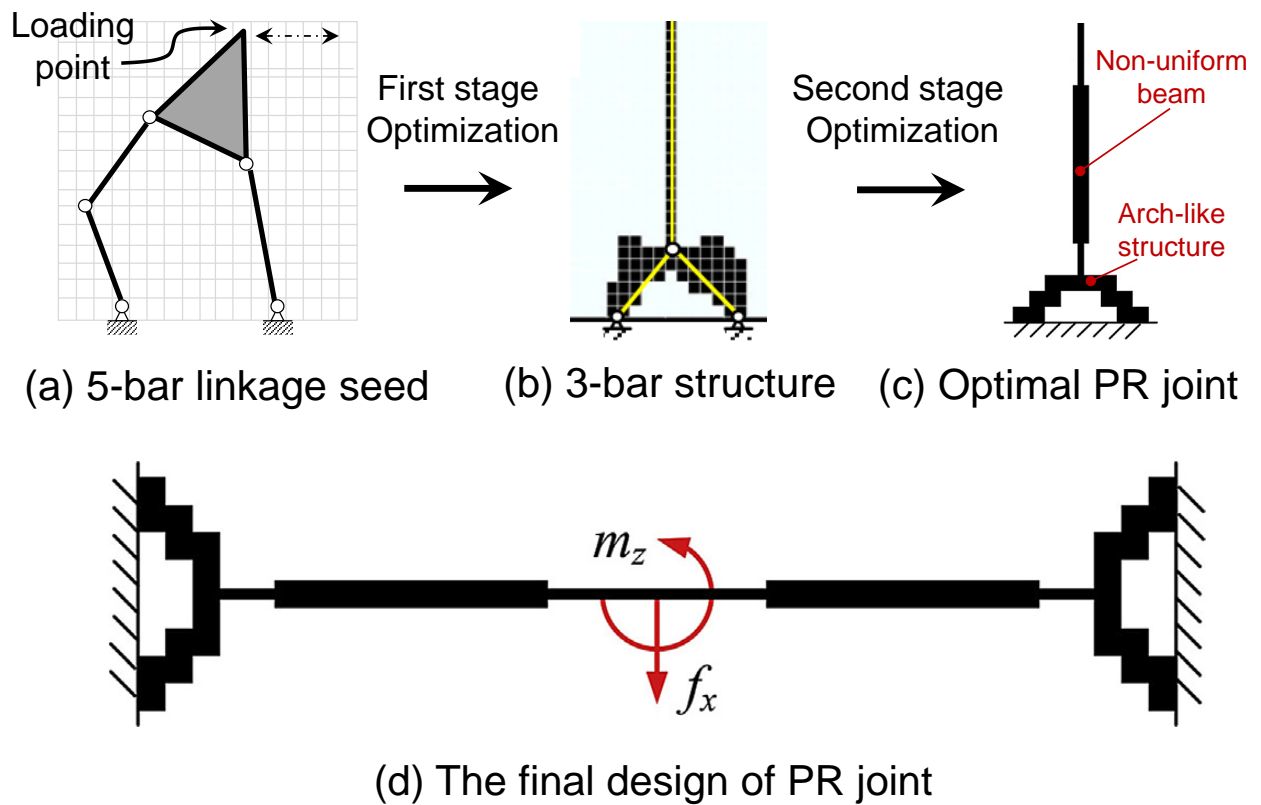
Figure 4.3: The synthesis process for the PR compliant joint. (a) A five-bar link-age seed is used for the mechanism-based approach. (b) The topology of the PR joint has evolved from the five-bar linkage into a three-bar structure after the first stage of optimization. Two link lengths has been reduced to zero, changing the topology of the seed. (c) The design has been further refined via the second stage optimization. The solution resembles a non-uniform beam, which is supported by an arch. (d) The final design of the PR joint. The joint is made symmetrical to further reduce the non-diagonal off-axis compliances.
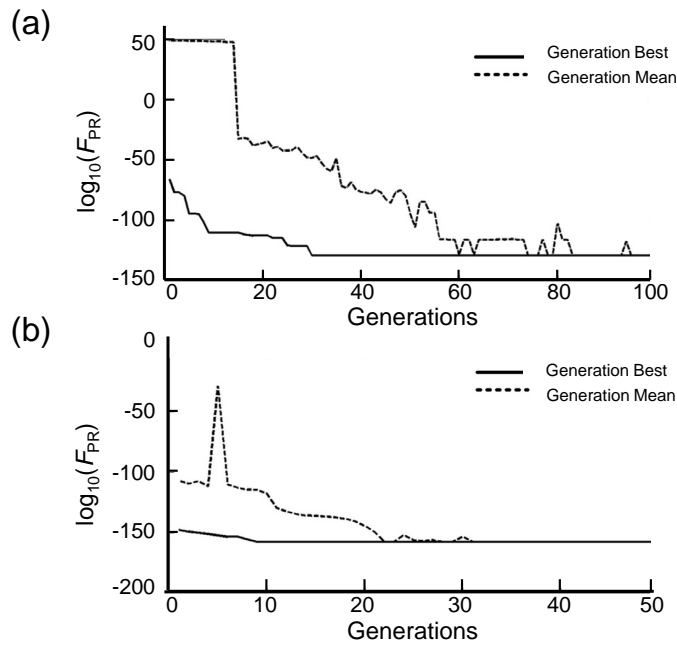
Figure 4.4: The convergence plot for the two stages of optimization processes for the compliant PR joint. (a) and (b) represent the convergence plots for the first and second stages of optimization, respectively. The optimization processes were shown to converge as both plots show that their mean and best fitness values managed to converge.

and utilized finite elements are similar to those of the PR compliant joint. The width of the design domain, however, is changed to 25 mm. As the active $\underline{P}$ compliant joint needs to deliver a large $x-$axis translation motion when its loading point is subjected to a F_x force, its actuating compliance, C_{11}, must be high while the rest of the components in the $\mathbf{C}_{\underline{P},6\times6}$ must be low. Thus, we use the following fitness function to optimize the compliant $\underline{P}$ joint's stiffness characteristics:

$$\text{minimize } F_\mathrm{p}(\mathbf{x}_p) = \frac{\Pi_{\delta=2}^{6}\Pi_{\eta=1}^{\delta}C_{\delta\eta}}{[C_{11}]^{20}}$$

$$\text{subject to: } \mathbf{K}_{\mathrm{P},n\times n}\mathbf{u}_{\mathrm{P},n\times1} = \mathbf{f}_{\mathrm{P},n\times1}.$$

(4.8)

The actuating compliance, C_{11}, has an exponent of 20 because there are 20 off-axis stiffness components. It is necessary to raise the exponent to 20 because this allows the optimization process to minimize all the non-actuating compliance components while still allowing the actuating compliance to be maximized. The vector $\mathbf{x}_\mathrm{P}$ represents the variables while the equality constraint represents the FEA governing equation. As the compliant $\underline{P}$ has only 1-degree-of-freedom, we will use a four-bar linkage as the seed for the mechanism-based approach (Fig. 4.5(a)). The coupler point of the seed, which is also its loading point, is located at the top row's central element. The seed is fixed by two points that are located at the bottom row. The first stage of optimization was carried out by evolving a population of 400 chromosomes via 100 generations. From Fig. 4.5(b), the solution still has a 4-bar topology but the limbs had become parallel with one another. Subsequently, the second stage of optimization further refines the solution with a finer mesh. Consequently, the optimal $\underline{P}$ compliant joint is obtained after the G.A. solver has evolved a population of 200 chromosomes via 50 generations. As shown in Fig. 4.5(c), the optimal $\underline{P}$ compliant joint resembles a tapered-shape
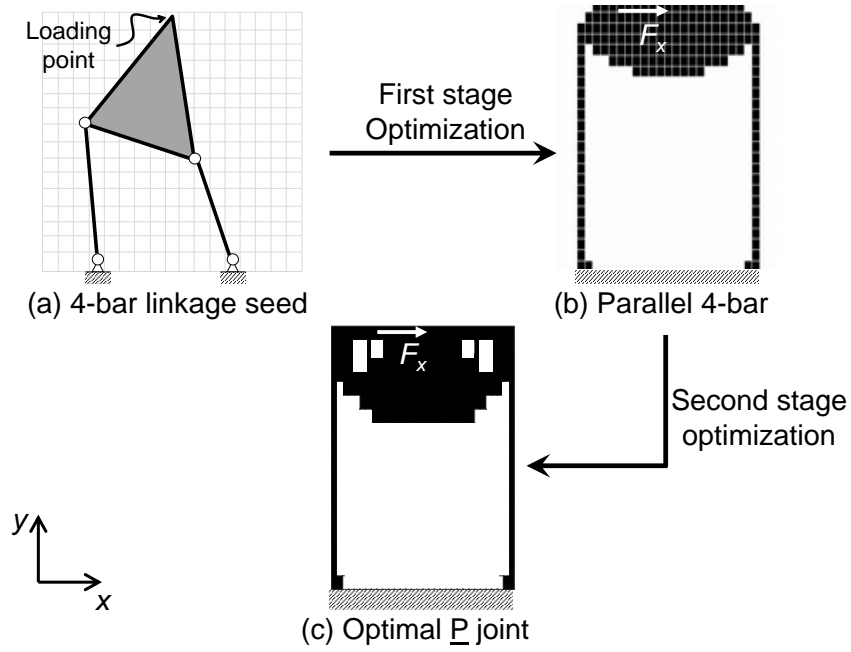
Figure 4.5: The synthesis process for the compliant P̲ joint. (a) A 4-bar linkage seed is used for the mechanism-based approach. (b) The solution obtained after the first stage of optimization. (c) The optimized design after the second stage optimization.

rigid-link supported by two thin beams. The optimization processes have converged and their convergence plots are plotted in Fig. 4.6.

The obtained stiffness matrix of the compliant P̲ joint (inverse of $\mathbf{C}_{\underline{P},\,6\times6}$) is given as:

$$
\mathbf{K}_{P,6\times6} =
\begin{bmatrix}
1338 & & & & & \\
0 & 9.72 \times 10^6 & & & \mathbf{SYM} & \\
0 & 5.94 \times 10^5 & 3.92 \times 10^5 & & & \\
0 & 2.84 \times 10^4 & -6205 & 350 & & \\
0 & 0 & 0 & 0 & 53.6 & \\
0 & 0 & 0 & 0 & 0 & 90.3
\end{bmatrix}. \tag{4.9}
$$

72
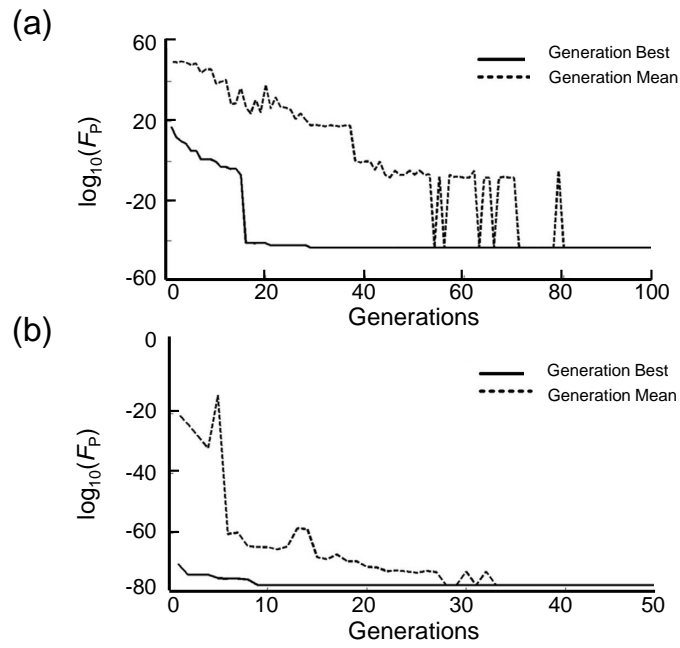
Figure 4.6: The convergence plot for the two stages of optimization processes for the active compliant P̲ joint. (a) and (b) represent the convergence plots for the first and second stages of optimization, respectively. The optimization processes were shown to converge as both plots show that their mean and best fitness values managed to converge.

4.3 The 3PPR FPM

The design of the optimal compliant joints obtained from the previous section will be used to construct a 3PPR FPM as shown in Fig. 4.7. For practical issues, we have smoothened out the sharp edges of the joints to prevent stress concentration. In order to achieve millimeters stroke range, we have selected electromagnetic voice-coil (VC) as the linear actuators. It is estimated that each VC actuator needs to generate a continuous force of at least 30 N, and the required dimensions of such a VC actuator is estimated to be at least ⬲ 60 mm × 60 mm. Thus, the dimensions of each sub-chain has been assigned to a design domain of 90 mm × 90 mm so that it can encase a VC actuator. The proposed FPM will be monolithically cut from a SUS316 stainless steel workpiece (19 mm thickness), and the Young's Modulus and Poisson ratio of the material are estimated to be 200 GPa and 0.33, respectively.

To optimize the stiffness characteristics for the end-effector, a size optimization is used to determine the optimal space distribution between the compliant joints. This is because by increasing L_3, it will increase the off-axis stiffness of the PR joints but will also decrease the actuating compliance of the active compliant P joint (refer to Fig. 4.7). In order to retain the actuating compliance of these joints, this optimization does not alter the thickness of the beams. Based on the configuration shown in 4.1, the stiffness matrix of each compliant joint obtained via the proposed topology optimization technique are expressed in terms of their local sub-chain frame. These sub-chain frames are illustrated in Fig. 4.1 where $\{1\}$, $\{2\}$, and $\{3\}$ have a z-axis rotation angle of $[\phi_1 \quad \phi_2 \quad \phi_3] = [\pi/3 \quad \pi \quad \pi/3]$ with respect to the global frame $\{g\}$, respectively. Based on the classical mechanism stiffness modeling approach [14,22], the compliance matrix of sub-chain j, $\mathbf{C}_{SC,j,6\times6}$, at the PR joint loading point can be determined by:
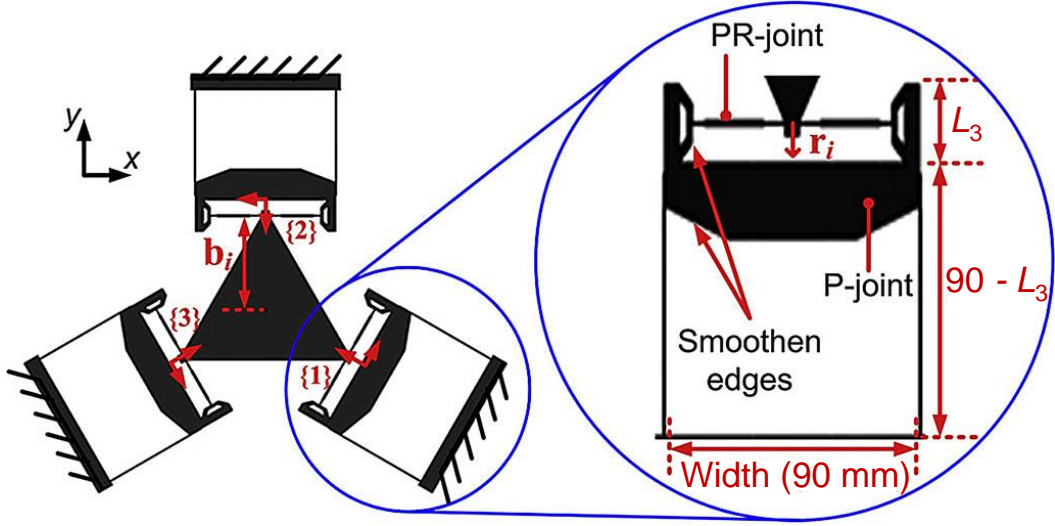
Figure 4.7: The schematic drawing for the 3$\underline{\text{P}}$PR FPM. The values L_3 and r_j are shown.

$$\mathbf{C}_{\mathrm{SC},j,6\times6} = \mathbf{C}_{\mathrm{PR},j,6\times6} + \mathbf{J}_j \left[\mathbf{C}_{\mathrm{P},j,6\times6}\right] \mathbf{J}_j^{\mathrm{T}},$$

$$\text{where} \quad \mathbf{J}_j = \begin{bmatrix} \mathbf{I}_{3\times3} & \hat{\mathbf{r}}_j \\ \mathbf{0}_{3\times3} & \mathbf{I}_{3\times3} \end{bmatrix}. \tag{4.10}$$

The matrix $\mathbf{J}_j$ refers to the Jacobian matrix, and the matrices $\mathbf{I}_{3\times3}$, $\mathbf{0}_{3\times3}$ and $\hat{\mathbf{r}}_j$ represent the identity, zero and the skew-symmetry matrices of the position vector, $\mathbf{r}_j$, respectively. Note that $\mathbf{r}_j$ represents the displacement vector from the loading point of sub-chain j to its compliant $\underline{\text{P}}$ joint's loading point (Fig. 4.7). After the chains' stiffness matrices are identified, the stiffness matrix of the end-effector, $\mathbf{K}_{\mathrm{ee},6\times6}$, can be computed:

$$\mathbf{K}_{\mathrm{ee},6\times6} = \sum_{j=1}^{3} \mathbf{Ad}_{\mathrm{T},j}^{-\mathrm{T}} \left[\mathbf{C}_{\mathrm{SC},j,6\times6}\right]^{-1} \mathbf{Ad}_{\mathrm{T},j}^{-1}, \tag{4.11}$$

75

$$\text{where} \quad \mathbf{Ad}_{\mathbf{T},j} = \begin{bmatrix} \mathbf{R}_z(\phi(j)) & \hat{\mathbf{b}}_j \mathbf{R}_z(\phi(j)) \\ \mathbf{0}_{3\times 3} & \mathbf{R}_z(\phi(j)) \end{bmatrix}. \tag{4.12}$$

The matrix $\mathbf{Ad}_{\mathbf{T},j}$ refers to the adjoint matrix, which consists of a rotational matrix $\mathbf{R}_z$ and a skew-symmetry matrix $\hat{\mathbf{b}}_j$ that represents the displacement vector from the end-effector to the loading point of the jth sub-chain (Fig. 4.7). As the main objective is to optimize the stiffness ratio of the proposed FPM, i.e. maximizing off-axis diagonal stiffness while minimizing the actuating stiffness in $\mathbf{K}_{ee,6\times 6}$, the fitness function becomes

$$\text{minimize} \ F_{\text{ee}}(L_3) = \frac{K_{xx} K_{yy} K_{\theta z \, \theta z}}{K_{zz} K_{\theta x \, \theta x} K_{\theta y \, \theta y}} \tag{4.13}$$

After using G.A to evolve a population of 10 chromosomes via 10 generations, the optimal solution of L_3 was found to be 20 mm. The final stiffness matrix of the optimized FPM, $\mathbf{K}_{\text{opt, ee}}$, is given as:

$$\mathbf{K}_{\text{opt,ee},6\times 6} = \begin{bmatrix} 2.82\times 10^4 & & & & & \\ 0 & 2.82\times 10^4 & & & \text{SYM} & \\ 0 & 0 & 8.93\times 10^5 & & & \\ 0 & -250 & 0 & 2.46\times 10^3 & & \\ 250 & 0 & 0 & 0 & 2.46\times 10^3 & \\ 0 & 0 & 0 & 0 & 0 & 41.4 \end{bmatrix}. \tag{4.14}$$

4.3.1 Discussion

In comparison with the stiffness ratios that range between 0.5 to 50 in the literature [7, 8, 9, 46, 50, 51, 52, 53], the optimized FPM's translational and rotational stiffness ratio are considered high as they are computed to be $\frac{K_{zz}}{K_{xx}} = \frac{K_{zz}}{K_{yy}} = \frac{8.93\times 10^5}{2.82\times 10^4} = 32$ and $\frac{K_{\theta x \theta x}}{K_{\theta z \theta z}} = \frac{K_{\theta y \theta y}}{K_{\theta z \theta z}} = \frac{2.46\times 10^3}{41.4} = 60$, respectively. However, as we specifically like to compare the effectiveness of the synthesized compliant

(a) 3P̲PR FPM with optimal joints

(b) 3P̲PR FPM with conventional joints
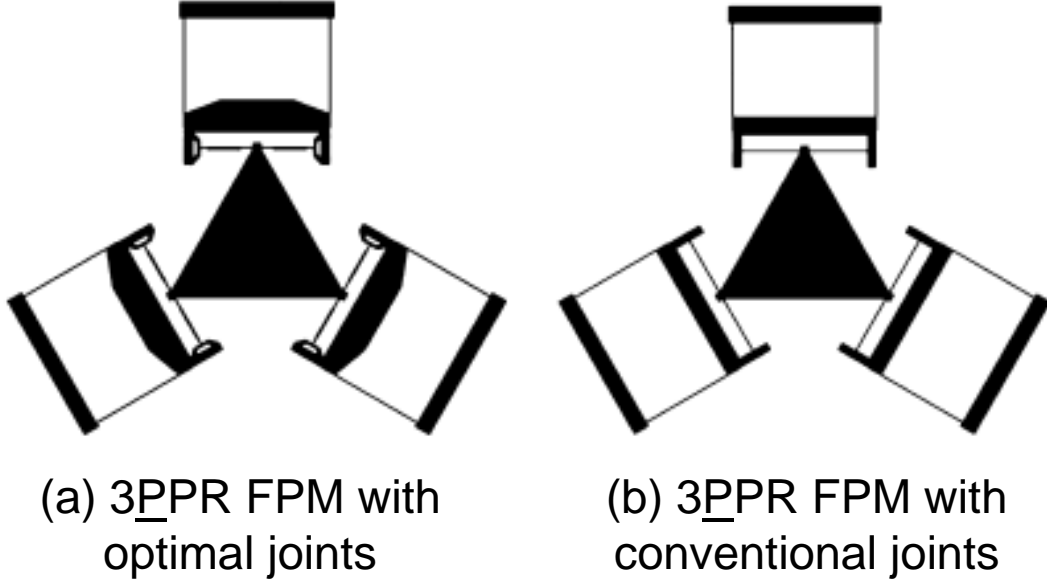
Figure 4.8: 3PPR FPMs articulated by compliant joints with (a) optimized topologies versus and (b) conventional topologies.

joints compared to traditional compliant joints, we have created a similar 3P̲PR FPM that is composed by compliant joints with traditional topologies (Fig. 4.8a). Termed as the conventional FPM (Fig. 4.8b), its compliant PR joint is a cantilever beam that has both ends fixed to a conventional compliant P̲ joint. The design of this stage uses the same optimal space distribution for the compliant P̲ and PR joints. Instead of making a physical prototype for the conventional FPM, it is more economical to conduct the comparison via FEA. To have a fair comparison, we have designed both FPMs to have one identical actuating compliance, and thus we have selected the compliance about the z-axis to be identical. For the conventional FPM, the flexure thickness of the traditional PR joints is selected as 0.6 mm to match the compliance about the z-axis of the optimized FPM.

By inverting the matrix in Eq. (4.14), the compliance matrix of the optimized

FPM is:

$$\mathbf{C}_{\text{opt,ee},6\times6} = \begin{bmatrix} 3.55 \times 10^{-5} & & & & & \\ 0 & 3.55 \times 10^{-5} & & & \textbf{SYM} & \\ 0 & 0 & 1.12 \times 10^{-6} & & & \\ 0 & -3.61 \times 10^{-6} & 0 & 4.06 \times 10^{-4} & & \\ 3.61 \times 10^{-6} & 0 & 0 & 0 & 4.06 \times 10^{-4} & \\ 0 & 0 & 0 & 0 & 0 & 2.42 \times 10^{-2} \end{bmatrix}.$$

Using a similar FEA solver, the compliance matrix of the conventional FPM, $\mathbf{C}_{\text{con, ee}}$, is given as:

$$\mathbf{C}_{\text{con,ee},6\times6} = \begin{bmatrix} 1.86 \times 10^{-5} & & & & & \\ 0 & 1.86 \times 10^{-5} & & & \textbf{SYM} & \\ 0 & 0 & 1.96 \times 10^{-6} & & & \\ 0 & -7.1 \times 10^{-6} & 0 & 5.41 \times 10^{-4} & & \\ 7.1 \times 10^{-6} & 0 & 0 & 0 & 5.41 \times 10^{-4} & \\ 0 & 0 & 0 & 0 & 0 & 2.42 \times 10^{-2} \end{bmatrix}.$$

(4.15)

Subsequently, the ratio between Eqs. (4.15) and (4.15) is

$$\mathbf{R}_{\text{comp}} = \mathbf{C}_{\text{opt,ee}} \odot \mathbf{C}_{\text{con,ee}} = \textbf{diag}\begin{bmatrix} 1.91 & 1.91 & 0.57 & 0.75 & 0.75 & 1 \end{bmatrix}, \qquad (4.16)$$

where $\odot$ represents the element-wise divisor operation. The ratio between $\mathbf{C}_{\text{opt, ee}}$ and $\mathbf{C}_{\text{con,ee}}$ in Eq. (4.16) have only considered the diagonal components as they are more critical. Here, the values of $R_{\text{comp,11}}$ and $R_{\text{comp,22}}$ are 1.91 (around 2) and this suggests that the actuating compliance of the optimized FPM is almost 2 times better than its conventional counterpart. Physically, this comparison suggests that the translational actuating compliance along the x- and y-axes of the

optimized FPM are almost two times greater than the conventional FPM. Note that $R_{\text{comp,66}}$ is 1 because both FPMs have the same actuating compliance about the z-axis. On the other hand, $R_{\text{comp,33}}$, $R_{\text{comp,44}}$ and $R_{\text{comp,55}}$ are all less than 1. This comparison suggests that the off-axis stiffness along the translational z-axis of the optimized FPM is almost twice of the conventional FPM. It also suggests that the off-axis stiffness about the x- and y-axes of the optimized FPM are higher than the conventional FPM. In summary, this comparison shows that the stiffness characteristic of the optimized FPM is superior than a similar conventional FPM.

4.4 Experimental results

4.4.1 Compliant Joints

As the effectiveness of the optimization processes depends heavily on the accuracy of the FEA, we would experimentally evaluate the actuating stiffness characteristics of the compliant joints here. In particular, the translational compliances for both the compliant P̲ and PR joints would be characterized. Likewise, the actuating rotational compliance of the PR joint would also be evaluated. Note that as these experiments were only used to evaluate the accuracy of the FEA, we did not smoothen the sharp edges of the joints yet.

Evaluation for translational compliance of compliant joints

In these experiments, we would evaluate the translational compliance of the joints. The fixed points of the compliant joints were constrained by a fixed plate and their loading points were mounted by a linear actuator. By varying the input current to the actuator, different magnitudes of force could be applied to the joints. Upon loading, the applied force and linear deflections of the joints would
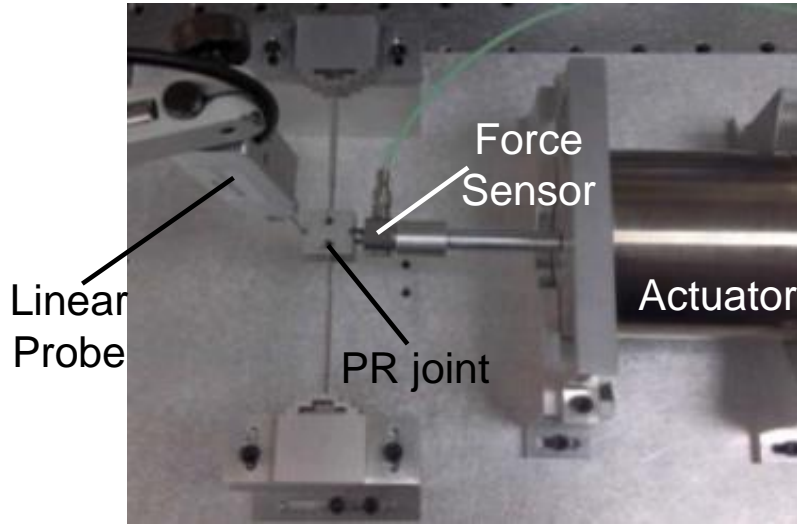
Figure 4.9: The experimental setup to evaluate the translational compliance of the joints. The setup for the compliant PR joint was used as an example. The joint would produce a translational deflection when the actuator supplied an input force. The deflection and magnitude of the input force would be measured by the linear probe and the force sensor, respectively.

be measured by a force sensor and a linear probe, respectively (see Fig. 4.9 for the experimental setup). Note that the force sensor was located between the joints and the actuator.

For both experiments, three sets of data were collected; each set consisted of 10 data points. The compiled data for the PR and $\underline{P}$ joints' experiments were shown via the scatter plots that had a corresponding best fit line in Fig. 4.10(a) and (b), respectively. Based on the gradient of the best fit lines, the PR and $\underline{P}$ joints had a compliance of 6.00×10^{-4} m/N and 7.04×10^{-4} m/N, respectively. These experimental results agreed with the FEA simulation where the predicted compliance for the PR and $\underline{P}$ joints were 6.68×10^{-4} m/N and 7.47×10^{-4} m/N (based on Eq. (4.7) and Eq. (4.9)), respectively. The deviation between the FEA predictions and experimental results for the PR and $\underline{P}$ joints were 10% and 6%
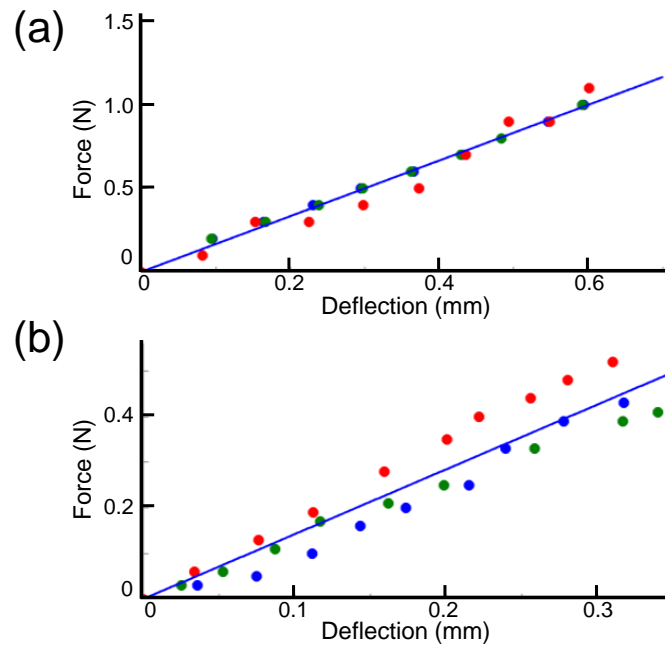
Figure 4.10: The experimental data for evaluating the translational compliance of the joints. (a) Experimental results for PR joint's linear deflection where the input force was plotted against the deflection. The slope of the best fit line was 1.66 N/mm. (b) Experimental results for P joint's linear deflection where the input force was plotted against the deflection. The slope of the best fit line is 1.42 N/mm.

respectively and they may be caused by manufacturing errors. However, these deviations were negligible and this suggested that the FEA predictions had high credibility for the translational compliance.

Evaluation for angular compliance of PR joint

The actuating angular compliance of the PR joint was investigated with these experiments. Similar to the previous experiments, the fixed points of the PR joint were constrained by a fixed plate. In order to apply an external torque to the loading point, we used a stepper motor to replace the linear actuator (Fig. 4.11). Different magnitudes of torques could be applied to the joint by varying the current supplied to the actuator. During the experiments, the linear deflections of a specific point (defined as point A) and the applied torque would be measured by using a linear probe and a torque sensor, respectively. By dividing point A's linear deflection with a prior known moment arm (20 mm), the angular deflection could be obtained.

In these experiments, three sets of 10 data points had been collected. The compiled data was represented by the scatter plot, and a best fit line had been plotted (Fig. 4.12). Based on the gradient of the best fit line, the angular compliance of the PR joint was evaluated to be 0.834 rad/(Nm) and this agreed with the FEA prediction of 0.909 rad/(Nm) (based on Eq. (4.7)). The deviation between the experiments and FEA simulation was only 9%, and could simply be due to manufacturing errors. However, since the deviation was small, this suggested that the FEA accuracy had relatively high credibility.
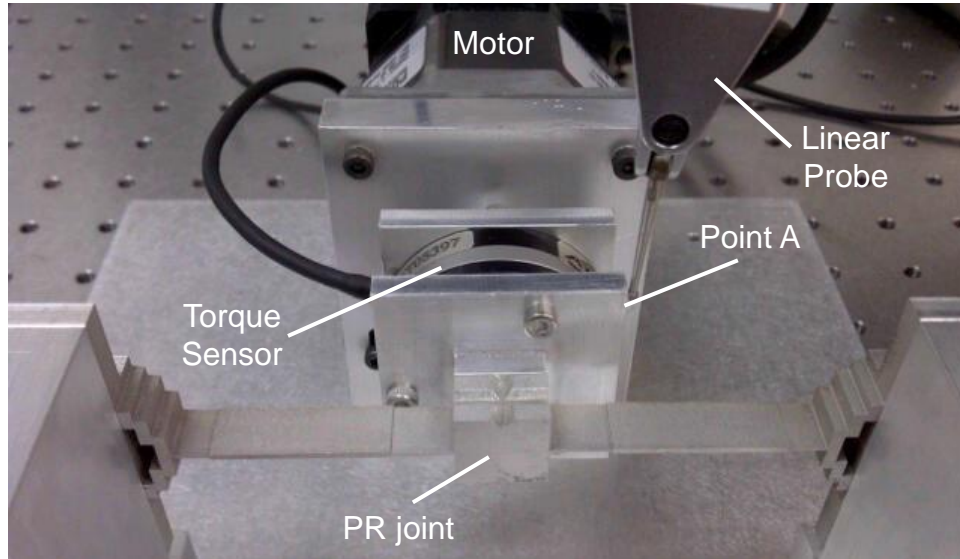
Figure 4.11: The experimental setup to evaluate the rotational compliance of the PR joint. The joint would produce a rotational deflection when the actuator supplied an input torque. The linear deflection and magnitude of the input torque would be measured by the linear probe and the force sensor, respectively. By dividing the linear deflection with a prior known moment arm, the angular deflection could be determined.
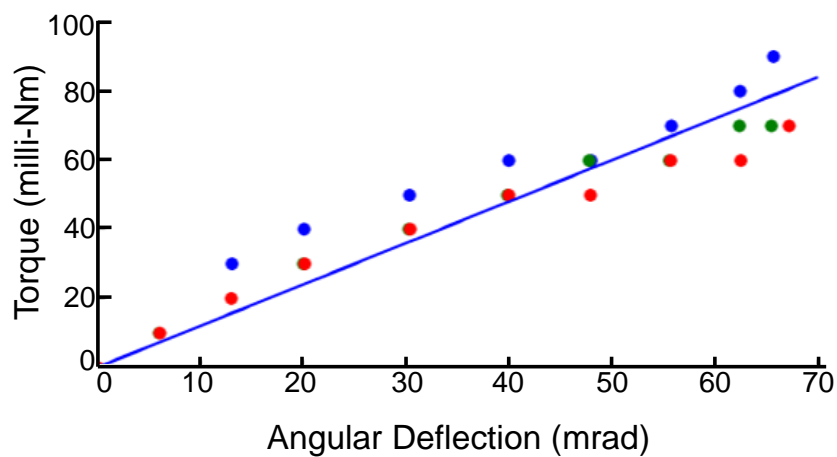
Figure 4.12: Experimental results for PR joint's angular deflection where the input torque was plotted against the angular deflection. The slope of the best fit line was 1.19 N m/rad.

4.4.2   3P̲PR

A monolithic prototype of the optimized FPM was also developed as shown in Fig. 4.13a. To validate the accuracy of the predicted compliance matrix in Eq. (4.15), we would evaluate the actual stiffness characteristic of the prototype experimentally. In these experiments, the deflections of the FPM would be recorded by a high resolution 3-Dimensional (3D) scanner (GOM, model: ATOS Triple scan) as shown in Fig. 4.13b. The deflections of the FPM would be induced by the picomotors (a type of linear actuators) and these loadings were simultaneously recorded by a 6-axes Force/Torque (F/T) sensor (ATI, model: MINI40; resolution: 0.01N or Nm). The F/T sensor was mounted to the end-effector and covered by a precise cut square cover. The square cover served as a reference datum for the picomotors' loading points and scanning landmark for the 3D scanner. Note that the recorded deflections were images of the corresponding motions of the square cover induced by the external loadings.

The FPM's end-effector had three actuating compliances, i.e. C_{xx} - the translation displacement along the x-axis due to F_x loading, C_{yy} - the translation displacement along the y-axis due to F_y loading, and $C_{\theta_z \theta_z}$ - the angular displacement about the z-axis due to M_z loading. Figure 4.14(a) plots the experimental C_{xx}. From the collected data points, the gradient of the best fit line in Fig. 4.14(a) showed that this compliance was 3.8×10^5 m/N. As compared to the C_{xx} of $\mathbf{C}_{\text{opt, ee}}$, the deviation is only 8.6%. The experimental results for C_{yy} were also plotted in Fig. 4.14(b). Using the gradient of the best fit line, this compliance was estimated to be 3.48×10^5m/N. When compared to the C_{yy} of $\mathbf{C}_{\text{opt, ee}}$, the deviation is only 2%. Lastly, from Fig. 4.14(c), the $C_{\theta_z \theta_z}$ compliance was identified as 2.63×10^2 rad/Nm. By comparing with $C_{\theta_z \theta_z}$ of $\mathbf{C}_{\text{opt,ee}}$, the deviation is also small (8.7%).

84
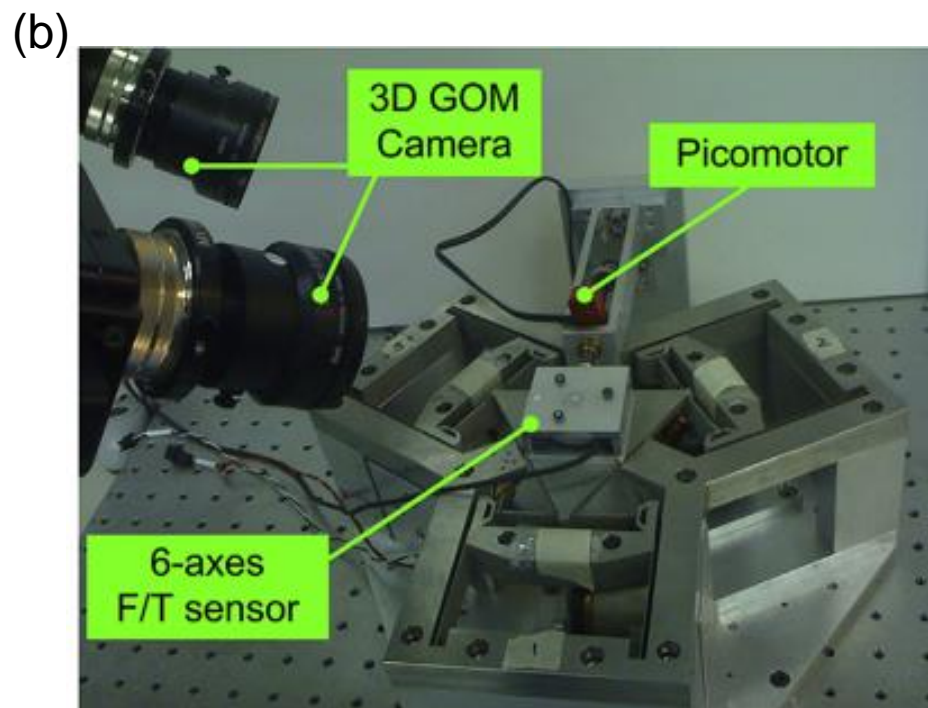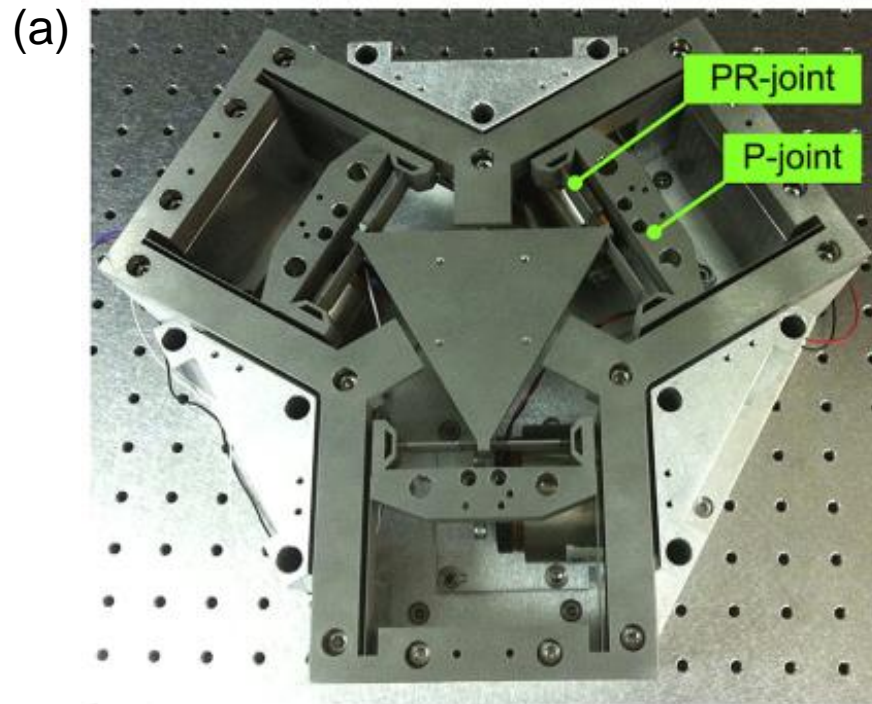
Figure 4.13: (a) A prototype of the optimized 3PPR FPM and (b) the experimental setup to evaluate the stiffness of the FPM. The 3D GOM camera was used to record the end-effector's deflections. The external loads were induced by the picomotor and the loads were recorded by the 6-axes F/T sensor.
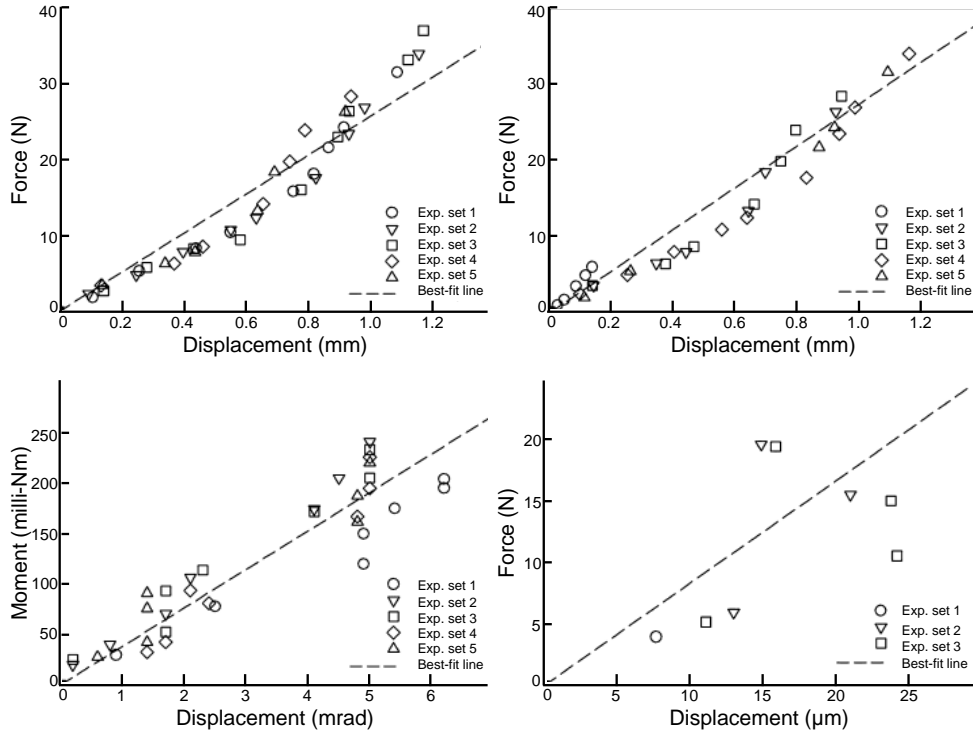
Figure 4.14: (a) Experimental results of the FPM's compliance along the x-axis due to F_x loading. (b) Experimental results of the FPM's compliance along the y-axis due to F_y loading. (c) Experimental results of the FPM's compliance about the z-axis due to M_z loading. (d) Experimental results of the FPM's compliance along the z-axis due to F_z loading.

The off-axis stiffness of the FPM were also investigated experimentally. Unfortunately, the rotational displacement about the x- and y-axes were too small to be recorded by the 3D scanner. Hence, we would only present the experimental data for the compliance along the z-axis - C_{zz}. These experimental results were plotted in Fig. 4.14(d) and the experimental C_{zz} was estimated to be 1.20×10^6 m/N. As compared to the C_{zz} of $\mathbf{C}_{\text{opt,ee}}$, the deviation was 7.1%. Although $C_{\theta_x\theta_x}$ and $C_{\theta_y\theta_y}$ could not be validated via this investigation, the collected experimental results and various comparisons with theoretical predictions were sufficient to suggest that the predicted stiffness characteristic agreed with the actual stiffness characteristic of the developed prototype.

86

4.5 Summary

This chapter further investigates the effectiveness and feasibility of the proposed topological optimization algorithm - the mechanism-based approach. This is carried out by first using the algorithm to create a $\underline{P}$ and a PR compliant joint. The obtained joints have feasible designs as there are neither disconnected solid elements nor ambiguous 'grey' elements within them. Furthermore, the convergence plots also indicate that the optimization processes are able to converge. The joints are then assembled into a 3$\underline{P}$PR FPM that can deliver a X-Y-θ motion. The effectiveness of the joints are evaluated by comparing it with a similar 3$\underline{P}$PR FPM that is assembled by traditional compliant joints. By comparing the stiffness ratios of these two FPMs via FEA, it has been shown that the FPM with optimized joints exhibits superior stiffness ratios. Our experimental results suggested that this FEA comparison was credible because the deviations between the actual and predicted stiffness for the optimized FPM were less than 9%.

Chapter 5

Design Methodology for Structural Optimal FPMs

This chapter introduces the methodology that can synthesize multi-degrees-of-freedom FPMs with optimal stiffness and dynamic properties. The proposed methodology will be demonstrated on another $X - Y - \theta_z$ centimeter-scale FPM. However, instead of pre-specifying the sub-chains' topology, we will use the proposed methodology to determine the optimal topology, shape and size for the sub-chains. The proposed methodology is discussed in Section 5.1 while a generic dynamic model will be derived in Section 5.2. By using the methodology and model, Section 5.3 will use the mechanism-based approach to synthesize a $X - Y - \theta_z$ FPM. The properties of this FPM will be evaluated experimentally in Section 5.4 and a summary will be provided in Section 5.5.

5.1   Design Methdology

A universal design methodology for integrating the kinematic and structural optimization approaches to synthesize multi-degrees-of-freedom FPMs with optimal

dynamic and stiffness properties will be shown here. We hypothesized that this can be achieved if the mechanism-based approach can be utilized to optimize the topology, shape and size for the sub-chains of a FPM.

The required steps to construct such an FPM can be divided into three steps as shown in Fig. 5.1. The FPM's design requirements, such as its required degrees-of-freedom and size constraints, are listed in Step 1. Based on the desired degrees-of-freedom, Step 2 uses the rigid-body-replacement method to synthesize the FPM's overall topology. This can be achieved by using the design guidelines for parallel robots to determine the required number and type of sub-chains [82, 83]. Step 2 is essential as it simplifies the formulations to implement structural optimization techniques on a compliant mechanism with multi-degrees-of-freedom.

Subsequently, based on the FPM's size constraints, Step 3 designs the sub-chains by identifying their optimal topology, shape and size sequentially. This is achieved by using the mechanism-based approach to automatically synthesize the sub-chains as a whole. The sub-chains' topology and shape are first identified by undergoing two optimizations that maximize the FPM's stiffness ratios, as shown in Steps 3(a) and (b). Note that these two steps do not include inertia effects as their objective is to select an optimal configuration for the FPM to achieve its desired kinematics.

Based on the obtained topology and shape, Step 3(c) will determine the sub-chains' size by optimizing the FPM's dynamic properties. As the stiffness ratios of the FPM may be compromised in Step 3(c), suitable stiffness constraints should be applied. For example, by considering the desired workspace and actuation capabilities, the maximum allowable actuating stiffness for the FPM can be determined. This computation can be achieved by using similar kinetostatic anal-

90

```
┌─────────────────────────────────────────────────┐
│         Step 1. Design Specification            │
│  (Desired degrees-of-freedom and size constraints) │
└─────────────────────────────────────────────────┘
                         │
                         ▼
┌─────────────────────────────────────────────────┐
│       Step 2. Overall Topology Synthesis        │
│      (Determine number and type of sub-chains)    │
└─────────────────────────────────────────────────┘
                         │
                         ▼
┌─────────────────────────────────────────────────┐
│          Step 3. Sub-chain Synthesis            │
│  ┌───────────────────────────────────────────┐  │
│  │        (a) Topological Optimization        │  │
│  │      (Maximize FPM's Stiffness Ratios)     │  │
│  └───────────────────────────────────────────┘  │
│                      │                           │
│                      ▼                           │
│  ┌───────────────────────────────────────────┐  │
│  │          (b) Shape Optimization           │  │
│  │      (Maximize FPM's Stiffness Ratios)     │  │
│  └───────────────────────────────────────────┘  │
│                      │                           │
│                      ▼                           │
│  ┌───────────────────────────────────────────┐  │
│  │           (c) Size Optimization           │  │
│  │    (Optimize FPM's Dynamic Properties)     │  │
│  └───────────────────────────────────────────┘  │
└─────────────────────────────────────────────────┘
```
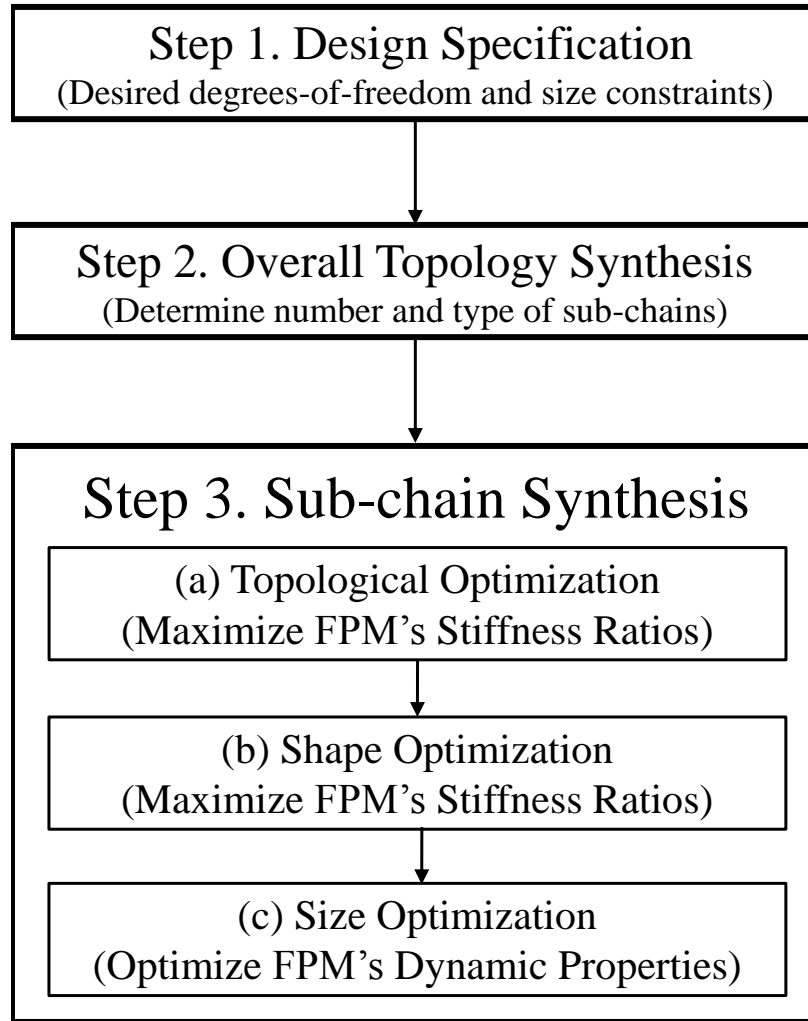
Figure 5.1: The synthesis steps: Based on the desired kinematic requirements, the overall topology of FPM will be identified. This is followed by identifying the optimal topology, shape and size of the sub-chains sequentially. The topological and shape optimizations will maximize the FPM's stiffness ratios while the size optimization will optimize the dynamic properties of the FPM.

yses to those performed in [9, 84]. Likewise, by using the maximum allowable actuating stiffness and minimum required stiffness ratios, the minimum allowable off-axis stiffness can be computed.

Although the synthesis process resembles the building block approach [78], there is one distinct difference. Similar to the kinematic approach, the building block method aims to identify feasible topologies for the compliant mechanism. Thus, there may be multiple feasible topologies, and the selected topology may not have optimal performance. The proposed methodology, however, aims to identify an optimal topology, shape and size for the FPMs' sub-chains such that the FPM's dynamic and stiffness properties can be optimized.

5.2   A Generic Dynamic Model for FPMs

In order to execute the dynamic optimization process shown in Step 3(c) in Fig. 5.1, a generic model that can accurately predict an arbitrary FPM's dynamic properties have to be derived. An analytical closed-form model, however, would be too difficult to derive if the geometries of the sub-chains are too complex. Alternatively, if a full FEA is implemented, the entire optimization process would be too computationally expensive. In view of this, a new semi-analytical dynamic model is developed to facilitate the dynamic optimization process for FPMs. We will use FEA to obtain key parameters for our closed form model. The procedure to derive the dynamic model for the FPMs' end-effector can be divided into two stages:

- Stage 1: Obtain the lump mass and stiffness matrices that describe the rigid-body motion of the sub-chains' loading point via simplifying the full FEA model. Note that the loading point of the sub-chains is also their connecting point to the end-effector.

- Stage 2: Use the lump mass and stiffness matrices of the sub-chains to obtain the equations of motion for the FPM's end-effector via the Lagrangian method.

Stage 1 can be carried out by first discretizing each sub-chain into a mesh of finite elements. The FEA structural stiffness matrix for the jth sub-chain can be expressed as $\mathbf{K}_{\text{SC},n\times n,j} = \sum_{i=1}^{\text{all elements}} \mathbf{K}_{\text{FE},i}$. Likewise, its structural FEA mass matrix, $\mathbf{M}_{\text{SC},n\times n,j}$ can be obtained by assembling each finite element's mass matrices, $\mathbf{M}_{\text{FE},i}$. By extracting essential qualities from $\mathbf{M}_{\text{SC},n\times n,j}$, the lump mass matrix $\mathbf{M}_{\text{SC},6\times 6,j}$ can be determined. The extracting process is commonly known as dynamic condensation in FEA. There are several known dynamic condensation techniques such as the Guyan reduction [85], IRS [86] and the SEREP [87] methods but they generally conserve the motion in their FEA nodes instead of the rigid-body motion of the structure. Thus, a modified dynamic condensation method that has similar characteristics as the Guyan reduction is presented in the subsequent sub-section.

Once $\mathbf{M}_{\text{SC},6\times 6,j}$ is identified, stage 2 determines the FPM's effective lumped 6×6 mass matrix, $\mathbf{M}_{\text{ee},6\times 6}$, by using the Lagrangian equation. The matrix $\mathbf{M}_{\text{ee},6\times 6}$ would account for the amalgamated inertia properties of the central platform, $\mathbf{M}_{\text{platform},6\times 6}$, and the sub-chains. The lump stiffness of the end-effector, $\mathbf{K}_{\text{ee},6\times 6}$, can be obtained by using Eq.s (5.17) and (5.18) respectively. Subsequently, based on the obtained $\mathbf{M}_{\text{ee},6\times 6}$ and $\mathbf{K}_{\text{ee},6\times 6}$, the six lowest natural frequencies of the FPM can be determined.

5.2.1 Stage 1 of semi-analytical dynamic model

The presented model is general for any FPM that has l non-identical parallel sub-chains as shown in Fig. 5.2. The jth sub-chain will be discretized into a

mesh of finite elements. The mass matrix of the ith finite element, $\mathbf{M}_{\text{FE},i}$, and the assembled mass matrix, $\mathbf{M}_{\text{SC},n\times n,j}$, can be expressed as:

$$\mathbf{M}_{\text{FE},i} = \iiint \rho\, \mathbf{N}^{\text{T}}\mathbf{N}\mathrm{d}V, \quad \mathbf{M}_{\text{SC},n\times n,j} = \sum_{i=1}^{\text{all elements}} \mathbf{M}_{\text{FE},i}. \tag{5.1}$$
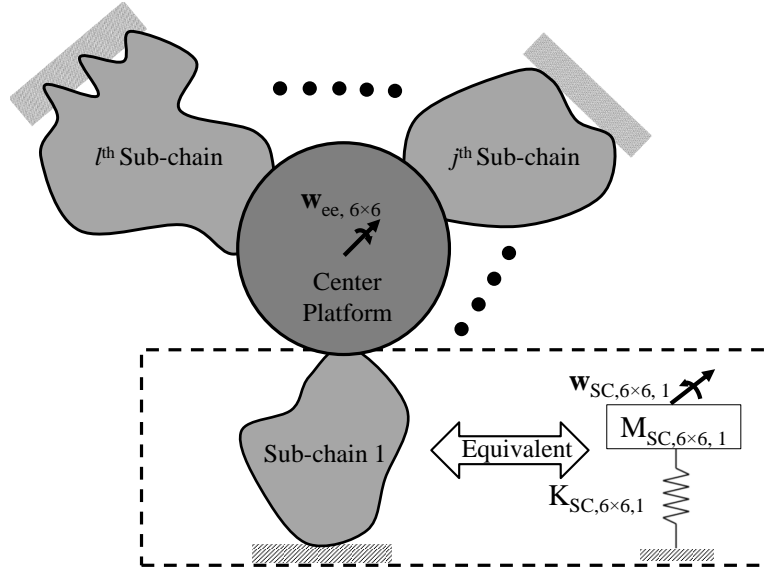
Figure 5.2: A generic FPM that has l arbitrary, parallel sub-chains attached to the central platform (represented by the circle). In the general configuration, the end-effector of the FPM is subjected to an arbitrary external wrench $\mathbf{w}_{\text{ee},6\times6}$. The wrench exerted on the jth sub-chain by the rigid platform is represented by the variable $\mathbf{w}_{\text{SC},6\times6,j}$. Each sub-chain can be represented by a corresponding 6×6 mass and stiffness matrix.

The matrix $\mathbf{N}$ represents the shape function matrix in FEA while the variable, ρ, represents the density of the finite element. The wrench, $\mathbf{w}_{\text{SC},6\times1,j}$, exerted on the loading point of the jth sub-chain can be described in the FEA format, $\mathbf{w}_{\text{SC},n\times1,j}$, by the span of the basis $[\mathbf{f}_x, \mathbf{f}_y, \mathbf{f}_z, \mathbf{m}_x, \mathbf{m}_y, \mathbf{m}_z]$:

$$\mathbf{w}_{\text{SC},n\times1,j} = q_1\mathbf{f}_x + q_2\mathbf{f}_y + q_3\mathbf{f}_z + q_4\mathbf{m}_x + q_5\mathbf{m}_y + q_6\mathbf{m}_z. \tag{5.2}$$

The corresponding nodal deformation, $\mathbf{u}_{\text{SC},n\times1,j}$, can be described as:

$$\mathbf{u}_{\text{SC},n\times1,j} = \mathbf{K}^{-1}_{\text{SC},n\times n,j}\mathbf{w}_{\text{SC},n\times1,j} = \mathbf{U}_{\text{SC},n\times6}\mathbf{q}, \text{ where}$$

$$\mathbf{U}_{\text{SC},n\times6,j} = \mathbf{K}^{-1}_{\text{SC},n\times n,j}[\mathbf{f}_x \quad \mathbf{f}_y \quad \mathbf{f}_z \quad \mathbf{m}_x \quad \mathbf{m}_y \quad \mathbf{m}_z],$$

(5.3)

and the vector $\mathbf{q} = [q_1 \quad q_2 \quad q_3 \quad q_4 \quad q_5 \quad q_6]^{\text{T}}$. Since $\mathbf{U}_{\text{SC},n\times6,j}$ is independent of time, the rate of change of the nodal deformation with respect to time, $\dot{\mathbf{u}}_{\text{SC},n\times1,j}$, can be expressed by:

$$\dot{\mathbf{u}}_{\text{SC},n\times1,j} = \mathbf{U}_{\text{SC},n\times6,j}\dot{\mathbf{q}}. \tag{5.4}$$

Thus, the kinetic energy of the jth sub-chain, T_j, is $T_j = \frac{1}{2}\dot{\mathbf{u}}^{\text{T}}_{\text{SC},n\times1,j}\mathbf{M}_{\text{SC},n\times n,j}\dot{\mathbf{u}}_{\text{SC},n\times1,j}$. In order to obtain an equivalent lump mass matrix of the jth sub-chain, $\mathbf{M}_{\text{SC},6\times6,j}$, the kinetic energy of the lump mass model has to be equal to the kinetic energy of the jth sub-chain in the FEA format:

$$\begin{aligned} T_j &= \frac{1}{2}\dot{\mathbf{u}}^{\text{T}}_{\text{SC},n\times1,j}\mathbf{M}_{\text{SC},n\times n,j}\dot{\mathbf{u}}_{\text{SC},n\times1,j} \\ &= \frac{1}{2}\dot{\mathbf{u}}^{\text{T}}_{\text{SC},6\times1,j}\mathbf{M}_{\text{SC},6\times6,j}\dot{\mathbf{u}}_{\text{SC},6\times1,j}. \end{aligned}$$

(5.5)

The vectors $\mathbf{u}_{\text{SC},6\times1,j}$ and $\dot{\mathbf{u}}_{\text{SC},6\times1,j}$ represent the rigid-body deflection of the jth sub-chain's loading point and its rate of change with time, respectively. Based on the compliance matrix, $\mathbf{u}_{\text{SC},6\times1,j}$ and $\dot{\mathbf{u}}_{\text{SC},6\times1,j}$ can be expressed as:

$$\mathbf{u}_{\text{SC},6\times1,j} = \mathbf{C}_{\text{SC},6\times6,j}\mathbf{q}, \quad \dot{\mathbf{u}}_{\text{SC},6\times1,j} = \mathbf{C}_{\text{SC},6\times6,j}\dot{\mathbf{q}}. \tag{5.6}$$

By substituting Eq. (5.4) and Eq. (5.6) into Eq. (5.5), and comparing the lump mass matrix with the FEA mass matrix, the lump mass matrix of the jth sub-chain
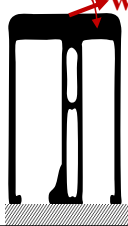
is expressed as:

$$\mathbf{M}_{\text{SC},6\times6,j} = \mathbf{C}_{\text{SC},6\times6,j}^{-\text{T}} \mathbf{U}_{\text{SC},n\times6,j}^{\text{T}} \mathbf{M}_{\text{SC},j} \mathbf{U}_{\text{SC},n\times6} \mathbf{C}_{\text{SC},6\times6,j}^{-1}. \tag{5.7}$$

The six lowest natural frequencies of the sub-chain can be obtained by using the lump mass and compliance matrices. In order to validate the effectiveness of the derived lump mass matrix, the six lowest natural frequencies of 20 arbitrary structures are evaluated with these lump matrices. Subsequently, these results are compared with the ones obtained from a full FEA analysis. It is found that although the lump matrices model is not able to conserve all six lowest frequencies of the structure, the first three to four lowest natural frequencies can be conserved reasonably well. This is especially true for the fundamental natural frequency where the deviation between the lumped model and a full FEA is always less than 3%. Table 5.1 shows two examples of such comparisons. It should be noted that the presented dynamic condensation method has similar characteristics compared to the Guyan reduction method. For example, this method can also accurately preserve several lowest natural frequencies that correspond to translational mode shapes. Due to its resemblance to the Guyan reduction method, this method may not be able to preserve natural frequencies that correspond with rotational mode shapes. This limitation could be caused by our assumption listed in Eq. (5.6), where the rate of change of the twist is assumed to be directly proportionate to $\dot{\mathbf{q}}$. While this assumption may be true for the fundamental natural frequency, Eq. (5.6) may not be able to capture essential information for the higher vibrational mode shapes. As a result, this may cause a large deviation for the higher modes of vibration. However, this dynamic condensation method is sufficient for this thesis as we can optimize a fundamental natural frequency that corresponds to a translational mode shape. Note that if each sub-chain's fundamental natural fre-

quency can be conserved, the fundamental natural frequency of the FPM can be predicted accurately.

Table 5.1: The six lowest natural frequencies of two random structures that are predicted by the lumped matrices model are shown in the center column. The right column shows the six lowest frequencies obtained via a full FEA respectively. Although the lumped matrices model cannot preserve the natural frequencies of all six modes, the first few modes of the natural frequencies of the structure had been fairly well approximated. This is especially true for the fundamental natural frequencies that are encased in the rectangular boxes.

Examples	Model (Hz)	Full FEA (Hz)
$\mathbf{W}_{\text{SC},6\times1}$	1,301	1,296
	1,743	1,593
	3,183	3,083
	16,571	5,421
	25,168	12,464
	59,323	13,170
$\mathbf{W}_{\text{SC},6\times1}$	3,912	3,912
	7,029	7,078
	7,085	9,497
	12,450	13,266
	33,615	68,483
	48,166	212,132

5.2.2 Stage 2 of semi-analytical dynamic model

The equations of motions for the FPM can be determined via the Lagrangian method. This can be achieved by deriving the total kinetic energy, strain energy, and work done on the FPM. The total kinetic energy of the FPM, T_{total}, can be described as:

$$T_{\text{total}} = \frac{1}{2}\{\dot{\mathbf{r}}_{\text{ee},6\times1}^{\text{T}}\mathbf{M}_{\text{platform},6\times6}\dot{\mathbf{r}}_{\text{ee},6\times1} + \sum_{j=1}^{l}\dot{\mathbf{u}}_{\text{SC},6\times1,j}^{\text{T}}\mathbf{M}_{\text{SC},6\times6,j}\dot{\mathbf{u}}_{\text{SC},6\times1,j}\}. \quad (5.8)$$

The variables, $\dot{\mathbf{r}}_{\text{ee},6\times1}$ and $\mathbf{M}_{\text{platform},6\times6}$, refers to the platform's twist and inertia, respectively. The relationship of $\dot{\mathbf{r}}_{\text{ee},6\times1}$ and the twist of each sub-chain's loading point can be described as:

$$\dot{\mathbf{r}}_{\text{ee},6\times1} = \mathbf{J}_j \dot{\mathbf{u}}_{\text{SC},6\times1,j}. \tag{5.9}$$

By substituting Eq. (5.9) into Eq. (5.8), the total kinetic energy can be expressed as:

$$T_{\text{total}} = \frac{1}{2}\dot{\mathbf{r}}_{\text{ee},6\times1}^{\text{T}}\{\mathbf{M}_{\text{platform},6\times6} + \sum_{j=1}^{l}\mathbf{J}_j^{-\text{T}}\mathbf{M}_{\text{SC},6\times6,j}\mathbf{J}_j^{-1}\}\dot{\mathbf{r}}_{\text{ee},6\times1}. \tag{5.10}$$

The total strain energy, S_{total}, can be expressed as:

$$\begin{aligned}
S_{\text{total}} &= \frac{1}{2}\sum_{j=1}^{l}\mathbf{u}_{\text{SC},6\times1,j}^{\text{T}}\mathbf{K}_{\text{SC},6\times6,j}\mathbf{u}_{\text{SC},6\times1,j} \\
&= \frac{1}{2}\mathbf{r}_{\text{ee},6\times1}^{\text{T}}\{\sum_{j=1}^{l}\mathbf{J}_j^{-\text{T}}\mathbf{K}_{\text{SC},6\times6,j}\mathbf{J}_j^{-1}\}\mathbf{r}_{\text{ee},6\times1}.
\end{aligned} \tag{5.11}$$

The work done, W, induced by the external wrench, $\mathbf{w}_{\text{ee},6\times1}$ can be expressed as:

$$W = \mathbf{w}_{\text{ee},6\times1}^{\text{T}}\mathbf{r}_{\text{ee},6\times1}. \tag{5.12}$$

Thus, by applying the Lagrangian equation with respect to the spatial coordinates of $\mathbf{r}_{\text{ee},6\times1}$, the closed-formed equations of motion for the FPM can be described as:

$$\mathbf{M}_{\text{ee},6\times6}\ddot{\mathbf{r}}_{\text{ee},6\times1} + \mathbf{K}_{\text{ee},6\times6}\mathbf{r}_{\text{ee},6\times1} = \mathbf{w}_{\text{ee},6\times1},$$

$$\text{where } \mathbf{K}_{\text{ee},6\times6} = \sum_{j=1}^{l} \mathbf{J}_j^{-\text{T}}\mathbf{K}_{\text{SC},6\times6,j}\,\mathbf{J}_j^{-1},$$

$$\mathbf{M}_{\text{ee},6\times6} = \mathbf{M}_{\text{platform},6\times6} + \sum_{j=1}^{l} \mathbf{J}_j^{-\text{T}}\mathbf{M}_{\text{SC},6\times6,j}\,\mathbf{J}_j^{-1}, \text{ and} \tag{5.13}$$

$$\mathbf{M}_{\text{SC},6\times6,j} = \mathbf{C}_{\text{SC},6\times6,j}^{-\text{T}}\mathbf{U}_{\text{SC},n\times6,j}^{\text{T}}\mathbf{M}_{\text{SC},j}\mathbf{U}_{\text{SC},n\times6}\mathbf{C}_{\text{SC},6\times6,j}^{-1}.$$

The six lowest natural frequencies of the FPM can be determined by solving the eigenvalues, ω_n, of the following equation:

$$\left| -\omega_n^2\mathbf{M}_{\text{ee},6\times6} + \mathbf{K}_{\text{ee},6\times6}\right| = 0. \tag{5.14}$$

5.3 Synthesis of a $X-Y-\theta_z$ FPM

Using the mechanism-based approach and the generic dynamic model, the proposed design methodology will be illustrated via the synthesis of an $X - Y - \theta_z$ FPM. Aluminum is used for the FPM and its Young's modulus and Poisson ratio are assumed to be 71 GPa and 0.33, respectively. The design requirements for this FPM are:

- A desired workspace of $1.2 \text{ mm} \times 1.2 \text{ mm} \times 6°$.
- Optimize the stiffness ratios of the FPM (at least > 80).
- Maximize the FPM's bandwidth (at least fundamental natural frequency > 60 Hz).

The minimum allowable stiffness ratios and bandwidth were selected to ensure that there is at least a 30% improvement over similar compliant mechanisms [7, 8, 46, 52]. This $X - Y - \theta_z$ FPM has the potential to be applied across var-

ious high precision applications pertaining to micro/nano-alignment, biomedical science, SEM, x-ray lithography and many other similar technologies [9, 50, 51].

5.3.1 Overall topology synthesis

The overall topology of the FPM is determined by using the rigid-body-replacement method. As mentioned in Chapter 4, there are three possible parallel robot configurations that can realize the required $X - Y - \theta_z$ planar motion. They are the 3-legged-Prismatic-Prismatic-Revolute, 3-legged-Prismatic-Revolute-Revolute and 3-legged-Revolute-Revolute-Revolute configurations. Despite having different combination of joints, all the three configurations have three 3-degrees-of-freedom sub-chains. Thus, the selected configuration for this FPM also has three identical, 3-degrees-of-freedom sub-chains to articulate a rigid end-effector. The sub-chains were arranged in a rotary symmetrical manner so that the payload can be divided equally. This configuration is shown in the left portion of Fig. 5.3 where the sub-chains are represented by springs with stiffness properties in all 6-axes. In contrast with Chapter 4, however, we do not specify the topology of the sub-chains. Instead we will use the mechanism-based approach to obtain the optimal topology for the sub-chains.

The design domain of a sub-chain is constrained within a 50 mm $\times 50$ mm area with a plate thickness of 20 mm. Note that the plate thickness is selected to be 20 mm because it gets increasingly difficult to fabricate flexures with more than 20 mm plate thickness. The loading point of the sub-chain is indicated by the location where it is subjected to an arbitrary wrench, $\mathbf{w}_{SC,6\times1}$, by the rigid platform as shown in Fig. 5.3. The bottom portion of the design domain is fixed to the ground.

The design of the sub-chains is determined by undergoing three optimization
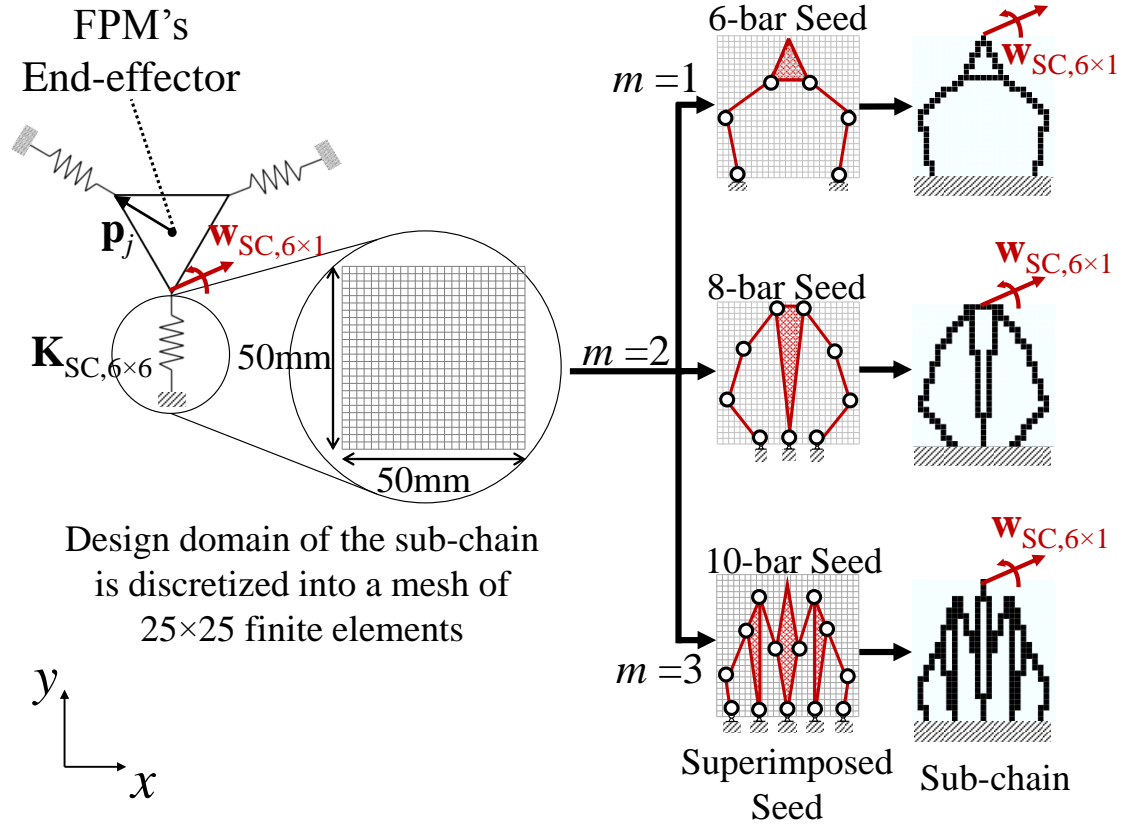
Figure 5.3: The conceptual design of the $X - Y - \theta_z$ FPM and the procedure to implement the mechanism-based approach. The FPM's rigid platform is represented by the triangle shown at the extreme left and the end-effector is located at the center of the platform. The end-effector is articulated by three identical sub-chains and the design domain of each sub-chain is discretized into a mesh of 25×25 identical finite elements. Based on the discrete variable m, a seed will be selected to generate a sub-chain. A sub-chain is created by converting the finite elements, which are in contact with the selected seed, into solid elements. The loading point of the sub-chain is indicated by the location where it is subjected to an arbitrary wrench, $\mathbf{w}_{SC,6\times1}$, by the platform. The bottom portion of the sub-chain is fixed to the ground.

processes in the following subsections. The static and dynamic analyses of the FPM, are performed with FEA. The selected mesh density always satisfies two conditions. Firstly, it enables each optimization process to complete within 4-6 hours. Secondly, the mesh density can predict the behavior of the sub-chain accurately. This is validated by using the mesh to pre-evaluate the mechanical behavior of several non-uniform beams before the optimization processes.

5.3.2   Topological optimization for sub-chains

The optimal topology for the sub-chains that can maximize the FPM's stiffness ratios is determined by using the mechanism-based approach. Thus, the design domain of each sub-chain is discretized into a mesh of finite elements, 25×25 identical 20-node quadratic elements, as shown in Fig. 5.3. Each element can only exist as either solid or void, and initially they are all void.

Subsequently, as each sub-chain has 3 degrees-of-freedom, we select three classical 3-degrees-of-freedom mechanisms with the simplest closed-loop configurations: the 6-, 8- and 10-bar linkages as the seeds. Closed-loop mechanisms are chosen as they have more complicated configurations than their open-loop counterparts, and if required they can evolve into serially-connected structures.

As there is more than one available seed, a discrete design variable, m, is used to select a seed that will be superimposed onto the void design domain. The superimposed seed will create a sub-chain by converting the finite elements that are in contact with it into solid elements (refer to Chapter 3 for the first way of mapping to represent the links), as shown on the right portion of Fig. 5.3. In order to minimize the FPM's off-axis parasitic motions, the seeds are always constrained to be symmetrical. The position and orientation of the seed's links are determined by the design variables - the position of the links' tip. Thus, in

this optimization, m and the position of the links' tip are encoded as the genetic material (design variables) in the genetic algorithm. Note that the topology of the seed can be changed if any link length of the seed approaches to zero during the optimization process.

Once a sub-chain has been created, its stiffness properties are determined via FEA. The stiffness matrices for the ith finite element, $\mathbf{K}_{\text{FE},i}$, and the jth sub-chain, $\mathbf{K}_{\text{SC},n\times n,j}$, are given as:

$$\mathbf{K}_{\text{FE},i} = \iiint \mathbf{B}^{\text{T}}\mathbf{D}\mathbf{B}\,\mathrm{d}V,\quad \mathbf{K}_{\text{SC},n\times n,j} = \sum_{i=1}^{\text{all elements}} s_i\mathbf{K}_{\text{FE},i}. \tag{5.15}$$

For convenience, the matrices $\mathbf{B}$ and $\mathbf{D}$ are restated to be the deformation matrix in FEA and compliance matrix in solid mechanics, respectively. Likewise, the variables s and V represent the state and volume of each finite element, respectively. If element i is void, a small number (10^{-6}) is assigned to s_i, instead of 0, to prevent numerical instability. If the element is solid, $s_i = 1$. The variable, $n \gg 6$, represents the dimension of $\mathbf{K}_{\text{SC},n\times n,j}$. The resultant FEA governing equation is:

$$\mathbf{K}_{\text{SC},n\times n,j}\mathbf{u}_{\text{SC},n\times 1,j} = \mathbf{f}_{\text{SC},n\times 1,j}. \tag{5.16}$$

The vectors $\mathbf{u}_{\text{SC},n\times 1,j}$ and $\mathbf{f}_{\text{SC},n\times 1,j}$ represent the nodal deformations and nodal force loadings of the jth sub-chain, respectively. The stiffness properties of the jth sub-chain can be determined by evaluating the loading point's rigid-body deflection when it is subjected to six orthogonal unit loads. These loads are expressed in the FEA format: $\mathbf{f}_x$, $\mathbf{f}_y$, $\mathbf{f}_z$, $\mathbf{m}_x$, $\mathbf{m}_y$ and $\mathbf{m}_z$. The loadings $\mathbf{f}_x$, $\mathbf{f}_y$ and $\mathbf{f}_z$ represent unit force loadings in the x, y and z directions, respectively. Likewise, the loadings $\mathbf{m}_x$, $\mathbf{m}_y$ and $\mathbf{m}_z$ represent unit torque loadings in the x, y and z directions,

respectively. The 6×6 compliance matrix for the jth sub-chain, $\mathbf{C}_{\text{SC},6\times6,j}$, can be expressed as:

$$\mathbf{C}_{\text{SC},6\times6,j} = \mathbf{A}\mathbf{U}_{\text{SC},n\times6,j},$$

$$\text{where } \mathbf{U}_{\text{SC},n\times6,j} = \mathbf{K}_{\text{SC},n\times n,j}^{-1}[\mathbf{f}_x \quad \mathbf{f}_y \quad \mathbf{f}_z \quad \mathbf{m}_x \quad \mathbf{m}_y \quad \mathbf{m}_z].$$

(5.17)

The six columns of the matrix $\mathbf{U}_{\text{SC},n\times6,j}$ represent the nodal deflections induced by corresponding loadings. The matrix, $\mathbf{A}$, extracts relevant nodal deflections to determine the rigid-body deflection of the loading point. The first three rows of $\mathbf{C}_{\text{SC},6\times6,j}$ represent the translational deflection while the last three rows represent the rotary deflection. The 6×6 stiffness matrix of the jth sub-chain, $\mathbf{K}_{\text{SC},6\times6,j}$, can be obtained by inverting $\mathbf{C}_{\text{SC},6\times6,j}$. This FEA is found to be accurate although the void elements are represented with $s_i = 10^{-6}$ instead of 0. This was checked by first creating multiple random sub-chains and evaluate their stiffness properties by using $s_i = 10^{-6}$ for the void elements. Subsequently, the stiffness properties of these sub-chains were re-evaluated by reducing $s_i = 10^{-9}$ for the void elements. The deviation between these two types of analyses is found to be less than 2% for all these random sub-chains.

Once the sub-chains' stiffness properties are identified, the end-effector's 6×6 stiffness matrix, $\mathbf{K}_{\text{ee},6\times6}$, can be expressed as:

$$\mathbf{K}_{\text{ee},6\times6} = \sum_{j=1}^{3}\{\mathbf{J}_j^{-\text{T}}\mathbf{K}_{\text{SC},6\times6,j}\mathbf{J}_j^{-1}\}, \quad \mathbf{J}_j = \begin{bmatrix} \mathbf{I}_{3\times3} & \hat{\mathbf{p}}_j \\ \mathbf{0}_{3\times3} & \mathbf{I}_{3\times3} \end{bmatrix}.$$

(5.18)

The matrix, $\mathbf{J}_j$, represents the Jacobian matrix for the jth sub-chain. The 3×3 skew-symmetric matrix, $\hat{\mathbf{p}}_j$, represents the position vector from the end-effector to the jth sub-chain as illustrated in Fig. 5.3. Note that before Eq. (5.18) is executed, the coordinate frame of all the $\mathbf{K}_{\text{SC},6\times6,j}$ are expressed in the global

coordinate frame that is shown in Fig 5.3.

The stiffness ratios of $\mathbf{K}_{ee,6\times6}$ are maximized by evolving the sub-chains' topology via this optimization problem:

$$\text{minimize} \quad f = \frac{K_{xx}K_{yy}K_{\theta z\theta z}}{K_{zz}K_{\theta x\theta x}K_{\theta y\theta y}}$$

$$\text{subject to:} \quad \mathbf{K}_{\text{SC},n\times n,j}\mathbf{u}_{\text{SC},n\times 1,j} = \mathbf{f}_{\text{SC},n\times 1,j}.$$

(5.19)

The equality constraint represents the FEA governing equation. After using genetic algorithm to evolve a population of 100 chromosomes via 40 generations, the optimal topology for the sub-chains is identified and shown in Fig. 5.4(h). The evolutionary process is illustrated in Fig. 5.4 and this optimization process is shown to converge as the best and mean fitness plots in Fig. 5.5 converge to the same value. Note that Fig. 5.4a-b are sample candidate solutions from the first generation. The total computational time is about four hours and the obtained topology is simple.

A simple topology, however, does not suggest that complicated topologies should be excluded during the synthesis process. Note that the solution is not known a priori, and it would be beneficial to increase the optimization search space by including these complicated topologies. It should also be noted that although the search space can be increased by having more seeds, this will also require more computational cost and time. Thus, by considering the computational cost, we only select three seeds.

5.3.3 Shape optimization for sub-chains

The stiffness ratio of the FPM can be further enhanced by letting the optimal topology of the sub-chain to undergo a shape optimization. This sub-section
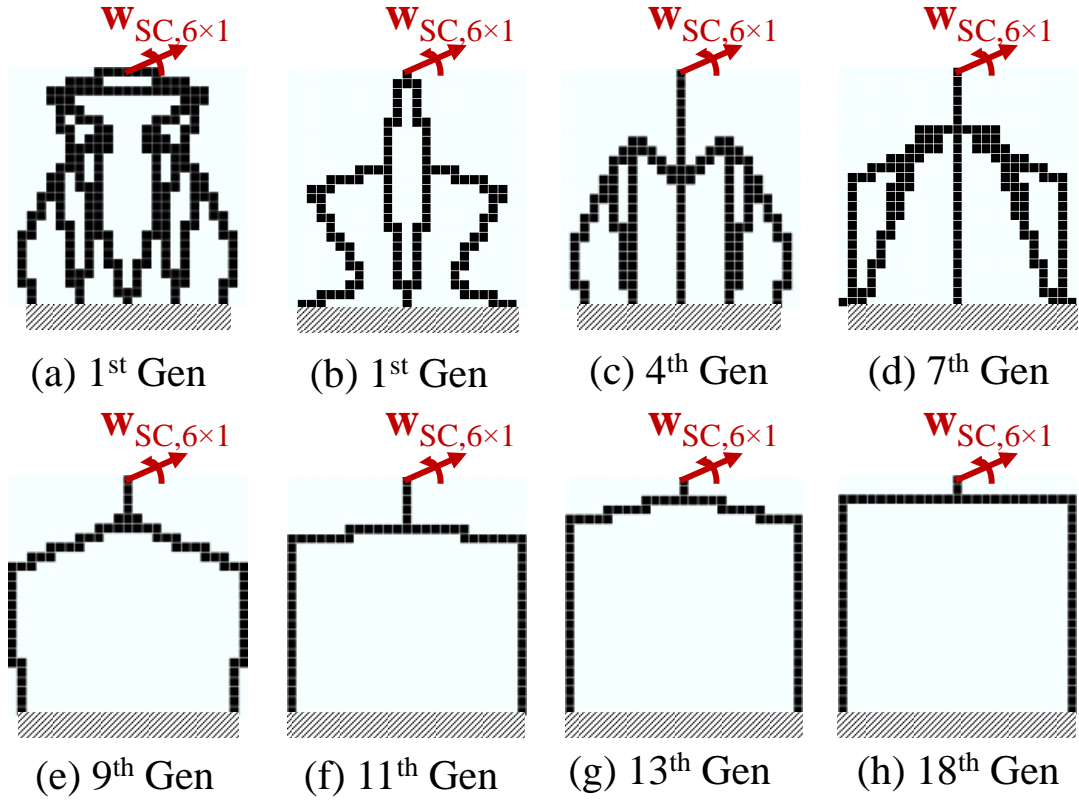
Figure 5.4: The evolutionary process to obtain the sub-chains' optimal topology. (a) and (b) are sample chromosomes in the first generation while (c) - (h) shows the solutions obtained in various generations. The final solution, (h), is obtained in the 18th generation.

Figure 5.5: The convergence plots for the topological optimization. The optimization process had converged as the best fitness and the mean fitness plots eventually converge to the same value.

shows how the curvature of each link in Fig. 5.4(h) is optimized.

Similar to the previous optimization process, the design domain of the sub-chains is first discretized into a mesh of 50×50 identical 8-node bi-linear finite elements as shown in Fig. 5.6(a). All the elements can either be solid or void and they are initially all selected as void here. The optimal topology obtained in Fig. 5.4(h) is then used as a seed to superimpose onto the void mesh of elements as shown in Fig. 5.6(b). The seed's link lengths in this optimization, however, would remain constant. Furthermore, instead of using straight lines, each link of the seed is represented by an area bounded by a straight line and a cubic curve as shown in Fig. 5.6(c)-(d) (refer to Chapter 3 for second way of mapping for the links). Note that we have excluded the harmonic curves to reduce computational time. As the sub-chains are geometrically symmetrical, this shape mapping would only be required to carry out on the left-half plane of the seed. Elements that are in contact with the seed are selected as solid elements. The features on the right-half plane are obtained by making a reflection about the symmetrical axis as shown in Fig. 5.6(e). This essentially creates a sub-chain as shown in Fig. 5.6(f). The stiffness properties of the FPM's end-effector are then evaluated via equations (5.15) to (5.18).

The profile of the curve is specified with three parameters, L, α and β as shown in Fig. 5.6(c). The parameter L represents the link length and it is predetermined by the previous optimization process. The parameters α_c and β_c are the design variables that specify the location and height of the stationary point of the curve, respectively. By varying these design variables, the seed's links can generate different curvatures. Thus, in this optimization, each chromosome in the G.A. encodes the curve parameters, α_c and β_c, as their genetic materials. Although the design variables are different, the fitness function and constraints for the shape
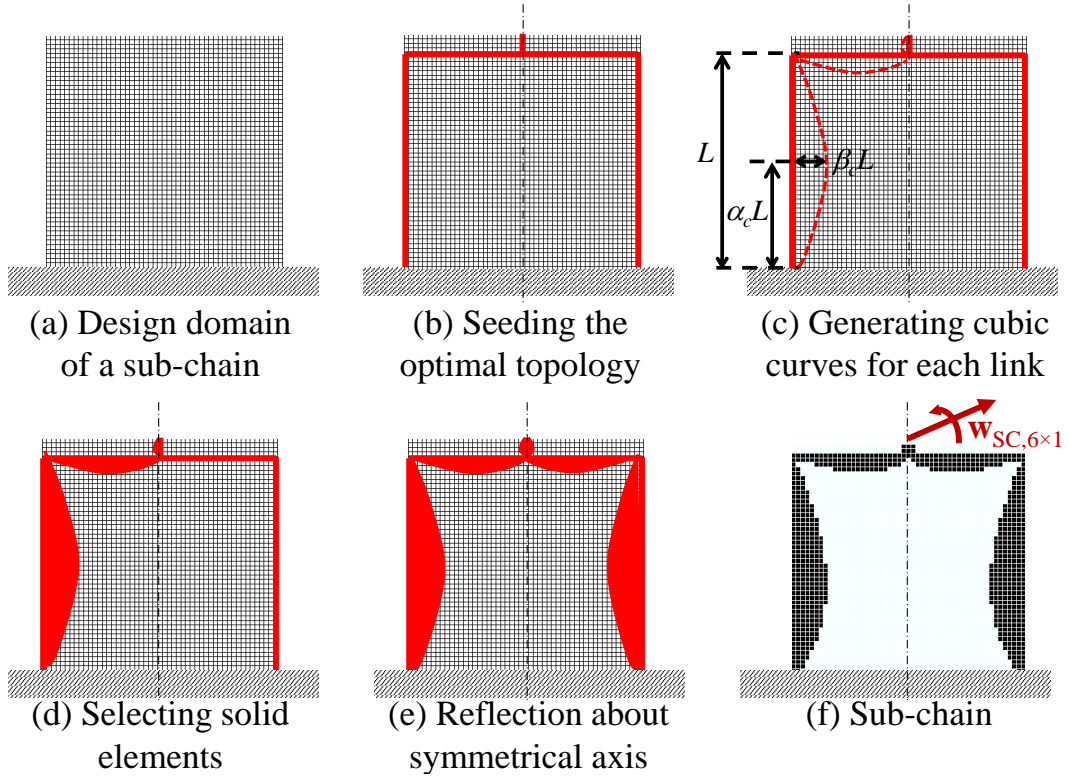
Figure 5.6: The procedure to implement shape optimization. (a) The design domain is discretized into a mesh of 50×50 identical finite elements which can be either solid or void. All of the elements are initially selected as void. (b) The optimal topology in Fig. 5.4(h) is superimposed onto the mesh. (c) Each link of the seed that is located on the left feature of the seed will produce an additional cubic curve. The location and height of the curve's stationary point are specified by the design variables α_c and β_c, respectively. (d) All the finite elements which are in contact with the area bounded by the cubic curve and the link are selected as solid elements. (e) A structure is formed by reflecting the left features about the symmetrical axis. (f) The generated sub-chain.

optimization are also formulated by Eq. (5.19).

The optimal shape is shown in Fig. 5.7(c) after G.A. evolves the curve parameters with 70 chromosomes via 50 generations. The evolutionary process is illustrated in Fig. 5.7. The optimization process is shown to converge as the best and mean fitness plots in Fig. 5.8 converge to the same value. The computational time is about 6 hours.

(a) 1ˢᵗ Gen   (b) 5ᵗʰ Gen   (c) 10ᵗʰ Gen
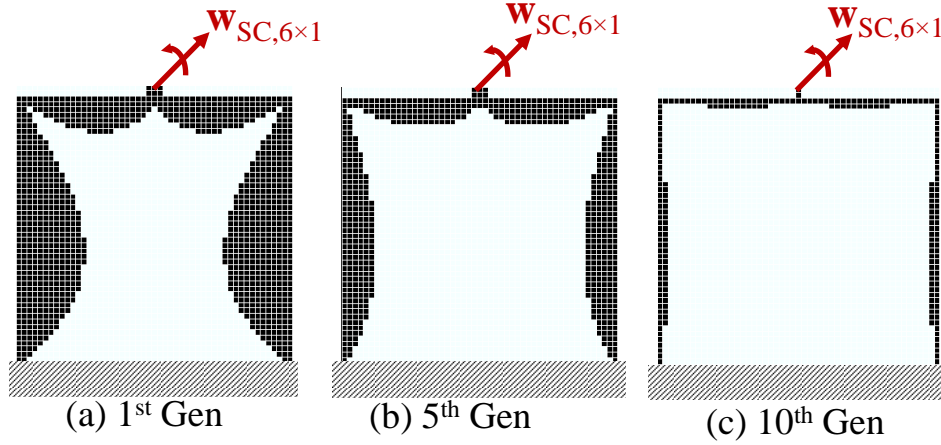
Figure 5.7: The evolutionary process to obtain the sub-chains' optimal shape based on its optimal topology. (a), (b) and (c) show the solutions obtained in the 1st, 5th and 10th generations, respectively. The final solution is obtained in the 10th generation.

It is found that the values of β_c for all the optimized cubic curves are small. Thus, the resultant shape for each link resembles a rectangle. However, despite having simple shapes, it does not suggest that the cubic curves are unnecessary. This is because the solution is not known a priori and if the cubic curves are removed, the search space for the shape optimization is inadvertently reduced.
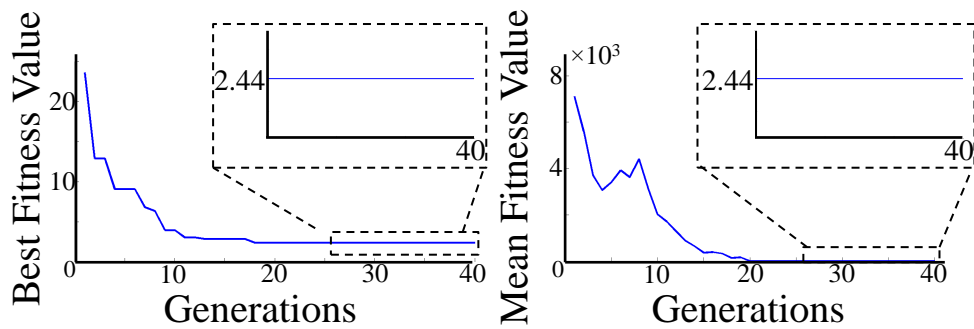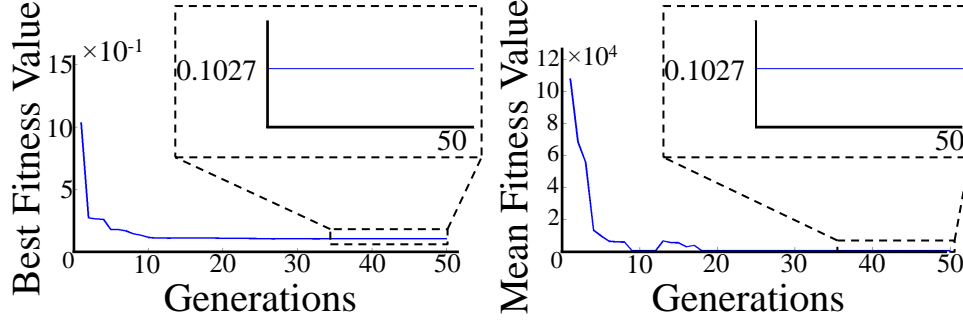
Figure 5.8: The convergence plots for the shape optimization. The optimization process is shown to converge as the best fitness and the mean fitness plots eventually converge to the same value.

5.3.4 Size optimization for sub-chains

The dynamic properties of the FPM will be optimized by using the obtained sub-chains to undergo a final size optimization. Specifically, this sub-section will optimize the flexural length and thickness of the sub-chains. Unlike previous optimizations, this optimization includes the inertia effects of the FPM as shown in Fig. 5.9. The inertias of the platform and the jth sub-chain are represented by the matrices $\mathbf{M}_{\text{platform},6\times6}$ and $\mathbf{M}_{\text{SC},6\times6,j}$, respectively. Each $\mathbf{M}_{\text{SC},6\times6,j}$ can be determined by the model provided in section 5.2.

The design variables, listed as t_i, are shown in Fig. 5.10(a). Thus, in this optimization, the chromosomes in genetic algorithm would encode the values of these design variables as their genetic material.

Each sub-chain is discretized into a mesh of 340 20-node quadratic finite elements. The FEA mass matrices of the ith finite element, $\mathbf{M}_{\text{FE},i}$, and j^{th} sub-chain, $\mathbf{M}_{\text{SC},n\times n,j}$, are given as:

$$\mathbf{M}_{\text{FE},i} = \iiint \rho \, \mathbf{N}^{\text{T}}\mathbf{N} \, \mathrm{d}V, \quad \mathbf{M}_{\text{SC},n\times n,j} = \sum_{i=1}^{\text{all elements}} \mathbf{M}_{\text{FE},i}. \qquad (5.20)$$

The matrix, $\mathbf{N}$, represents the shape function of the finite element while the

110
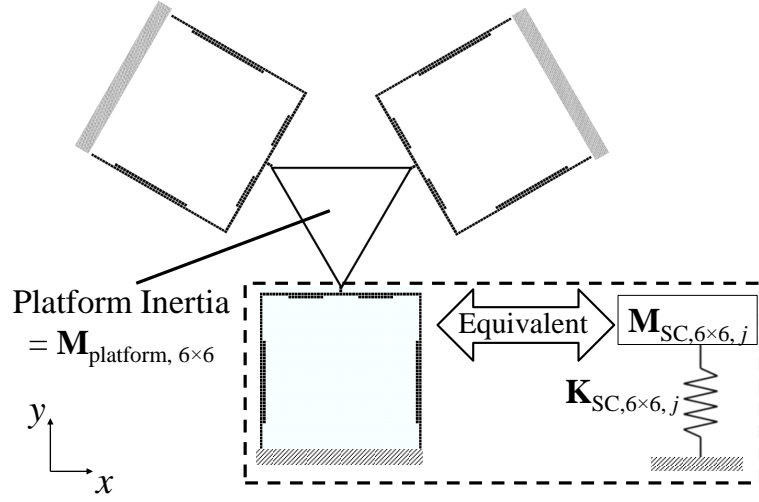
Figure 5.9: A schematic representative of the FPM's dynamic model. The platform inertia is represented by the mass matrix, $\mathbf{M}_{\text{platform},6\times6}$ while the inertia and stiffness matrices of each sub-chain can be represented as $\mathbf{M}_{\text{SC},6\times6,j}$ and $\mathbf{K}_{\text{SC},6\times6,j}$, respectively.

variable, ρ, represents the density of the element. The mass matrices, $\mathbf{M}_{\text{SC},6\times6,j}$, is given as:

$$\mathbf{M}_{\text{SC},6\times6,j} = \mathbf{C}_{\text{SC},6\times6,j}^{-\text{T}}\mathbf{U}_{\text{SC},n\times6,j}^{\text{T}}\mathbf{M}_{\text{SC},n\times n,j}\mathbf{U}_{\text{SC},n\times6}\mathbf{C}_{\text{SC},6\times6,j}^{-1}. \tag{5.21}$$

Using Eq. (5.21) and the Lagrangian method, the end-effector's equivalent inertia matrix, $\mathbf{M}_{\text{ee},6\times6}$, is:

$$\mathbf{M}_{\text{ee},6\times6} = \mathbf{M}_{\text{platform},6\times6} + \sum_{j=1}^{3}\mathbf{J}_j^{-\text{T}}\mathbf{M}_{\text{SC},6\times6,j}\,\mathbf{J}_j^{-1}. \tag{5.22}$$

Although the FPM has many natural frequencies, we will only maximize its fundamental natural frequency (bandwidth) as a proof-of-concept. It should, however, be noted that it is also possible to optimize the natural frequency of higher vibrational modes. The bandwidth, $\omega_{n,1}$, can be maximized via this opti-

mization:

$$\text{minimize}\, f_1 = \frac{1}{\omega_{n,1}}$$

$$\text{subjected to: } \left| -\omega_n^2 \mathbf{M}_{\text{ee},6\times 6} + \mathbf{K}_{\text{ee},6\times 6} \right| = 0$$

$$K_{xx} \leq 2.0 \times 10^4 \text{ N/m}, K_{yy} \leq 2.0 \times 10^4 \text{ N/m},$$

$$K_{zz} \geq 1.6 \times 10^6 \text{ N/m}, K_{\theta x \theta x} \geq 1.2 \times 10^3 \text{ Nm/rad},$$

$$K_{\theta y \theta y} \geq 1.2 \times 10^3 \text{ Nm/rad}, K_{\theta z \theta z} \leq 15 \text{ Nm/rad}.$$

$$(5.23)$$

The six lowest natural frequencies of the FPM can be determined by solving the eigenvalues, ω_n, in the equality constraint shown in Eq. (5.23). In order to achieve the required workspace with three actuators that can supply a maximum of 8 N, the maximum allowable actuating stiffness K_{xx}, K_{yy} and $K_{\theta z \theta z}$ can be determined. This computation can be achieved by using similar kinetostatic analyses that were demonstrated in [9, 84]. Furthermore, based on the required stiffness ratios (> 80), the minimum allowable off-axis stiffness, K_{zz}, $K_{\theta x \theta x}$ and $K_{\theta y \theta y}$, can be computed. Note that the stiffness ratios are feasible as they are within the 'upper bound' limits of the FPM. These 'upper bound' limits are determined by undergoing a size optimization with the fitness function and constraints listed in Eq. (5.19) instead of Eq. (5.23).

The optimal FPM is obtained, as shown in Fig. 5.10(b), after genetic algorithm evolves a population of 100 chromosomes via 100 generations. The jagged edges of the design have been smoothened to prevent stress concentration. The optimization process is shown to converge as the best and mean fitness plots in Fig. 5.11 converge to the same value. The total computational time is about 5 hours and the simulated stiffness properties of the FPM are:

112

t_1 t_2

t_i • • •

Size Optimization

Sub-chains with
Smoothened Edges

y

x

(a) Optimal Topology and
Shape of Sub-chain
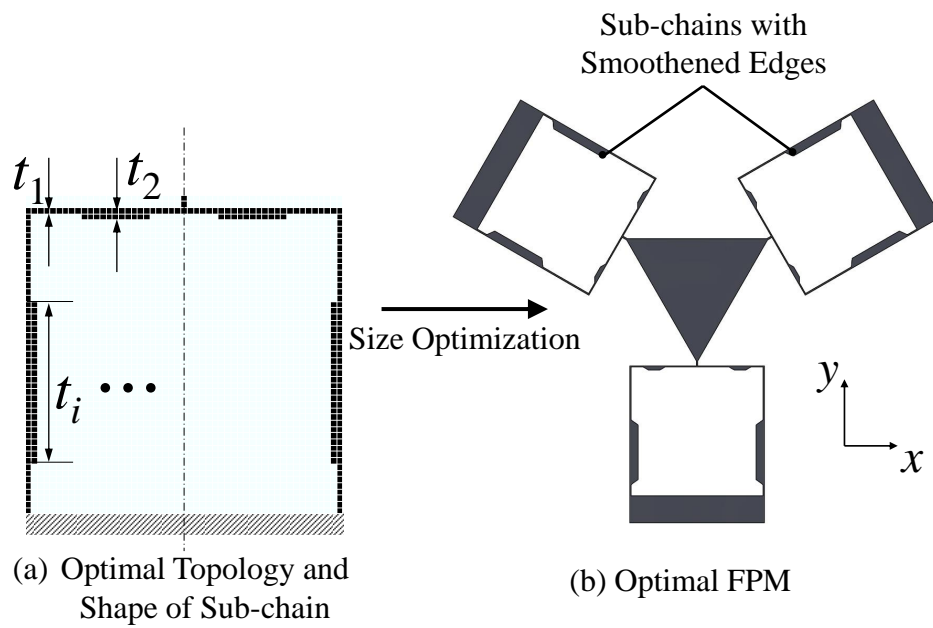
(b) Optimal FPM

Figure 5.10: The procedure to implement size optimization on the FPM. By undergoing another size optimization on the sub-chain shown in (a), the optimal FPM is obtained in (b).
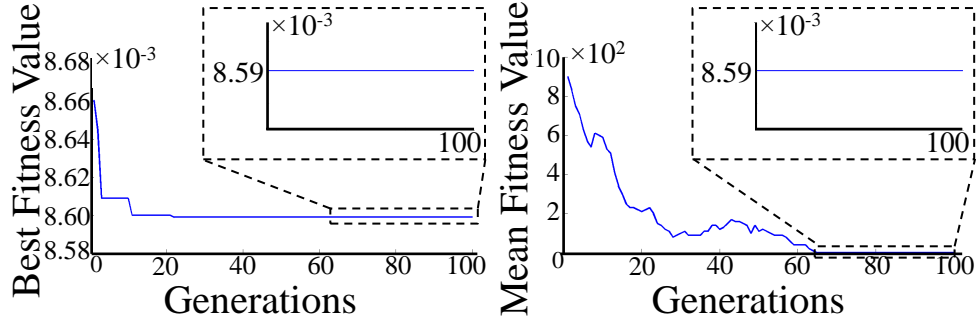
Figure 5.11: The convergence plots for the size optimization. The optimization process converges as the best fitness and the mean fitness plots eventually converge to the same value.

$$
\mathbf{K}_{ee,6\times 6} =
\begin{bmatrix}
2.0 \times 10^4 & & & & & \\
0 & 2.0 \times 10^4 & & & \mathbf{SYM} & \\
0 & 0 & 2.6 \times 10^6 & & & \\
0 & -545 & 0 & 1.3 \times 10^3 & & \\
545 & 0 & 0 & 0 & 1.3 \times 10^3 & \\
0 & 0 & 0 & 0 & 0 & 12
\end{bmatrix}.
\tag{5.24}
$$

The obtained K_{xx}, K_{yy}, K_{zz}, $K_{\theta x \theta x}$, $K_{\theta y \theta y}$, $K_{\theta z \theta z}$ are 2.0×10^4 N/m, 2.0×10^4 N/m, 2.6×10^6 N/m, 1.3×10^3 Nm/rad, 1.3×10^3 Nm/rad and 12 Nm/rad, respectively. The translational and rotational stiffness ratios are $K_{zz}/K_{xx} = K_{zz}/K_{yy} = 130$ and $K_{\theta x \theta x}/K_{\theta z \theta z} = K_{\theta y \theta y}/K_{\theta z \theta z} = 108$, respectively. The simulated bandwidth for the FPM is 117 Hz and it corresponds to the x-axis translational mode shape. Due to the FPM's rotary symmetrical configuration, the second lowest natural frequency is also equal to 117 Hz and it corresponds to the y-axis translational mode shape.

Stress analyses are conducted via Comsol simulations after the size optimization is completed and the jagged edges smoothened. These analyses are conducted by first computing the required wrench on the FPM's end-effector, $\mathbf{w}_{ee,6\times 6}$,

such that the FPM can achieve its desired workspace. This is computed by pre-multiplying the stiffness matrix in Eq. (5.24) to the maximum travel range of the desired workspace. Subsequently, the FPM's Von Mises stress induced by $\mathbf{w}_{ee,6\times6}$ is determined. Simulation results indicate that the maximum induced Von Mises stress is 126 MPa and it is lower than the yield stress and fatigue stress of the FPM. This implies that the FPM has approximately 10^8 lifecycles [88]. Note that we assume that the FPM can be constructed with aluminium 7075-T6, and its yield stress and fatigue stress are approximated to be 450 MPa and 159 MPa, respectively.

While it is possible to include fatigue and yield stress constraints in Eq. (5.23) during the optimization process, we have excluded such stress analyses to reduce computational costs.

5.3.5 Discussion

The obtained FPM had achieved stiffness ratios that were greater than 100, and a high bandwidth of 117 Hz. These properties have satisfied the required design criteria that are listed in the beginning of Section 5.3. The targeted workspace of the FPM can also be theoretically achieved as the actuating stiffness had been constrained based on the actuators' capabilities (as shown in Eq. (5.23)). Furthermore, as the maximum induced Von Mises stress is lower than the FPM's fatigue stress, this implies that the FPM can repeat approximately 10^8 cycles.

The obtained stiffness ratios had shown significant improvement over existing centimeter-scale compliant mechanisms with 3 degrees-of-freedom. The stiffness ratios of these compliant mechanisms are typically between $0.5 - 50$ [7, 8, 9, 46, 50, 51, 52, 53]. The stiffness ratios are also much more superior than the 3PPR FPM in Chapter 4 because the topology and shape of the sub-chains

have been optimized. Furthermore, the obtained bandwidth also has significant improvement over existing compliant mechanisms, which have translational and rotational deflections greater than 0.5 mm and $0.5°$, respectively. The bandwidth of these compliant mechanisms typically does not exceed 45 Hz [7, 8, 46, 52].

The configuration of the obtained FPM resembles the classical 3-legged-Prismatic-Prismatic-Revolute architecture. The two parallel vertical beams resemble a prismatic joint that slides horizontally, as shown in Fig. 5.12(a). The combination of the horizontal beam and the top vertical beam resemble the second prismatic joint and a revolute joint that provide vertical and rotational motions. These deformation characteristics are illustrated in Fig. 5.12(b) and Fig. 5.12(c), respectively. Once we have identified the active joints, it will be possible to use laser interferometry sensors to implement position control at the joint space level. By controlling the position of the active joints, we can use the kinematic formulations shown in Eq. (4.3) to control the orientation and position of the end-effector. However, as the focus of this thesis is on the design of the FPMs, the control aspects can only be explored as a future work.

Despite having a simple topology and shape for the FPM's sub-chains, it should be noted that this design is unique from other $X - Y - \theta_z$ FPMs in the literature. There may, however, exist more optimal solutions if more seeds, and higher order polynomial curves are used in the topological and shape optimizations, respectively. However, this would in turn require more computational time and cost.

Lastly, different topologies and shapes may be obtained if the fitness function in Eq. (5.19) is changed. This can be achieved by altering the stiffness components' indices where the optimization processes would place higher emphasis for components with higher indices.

116
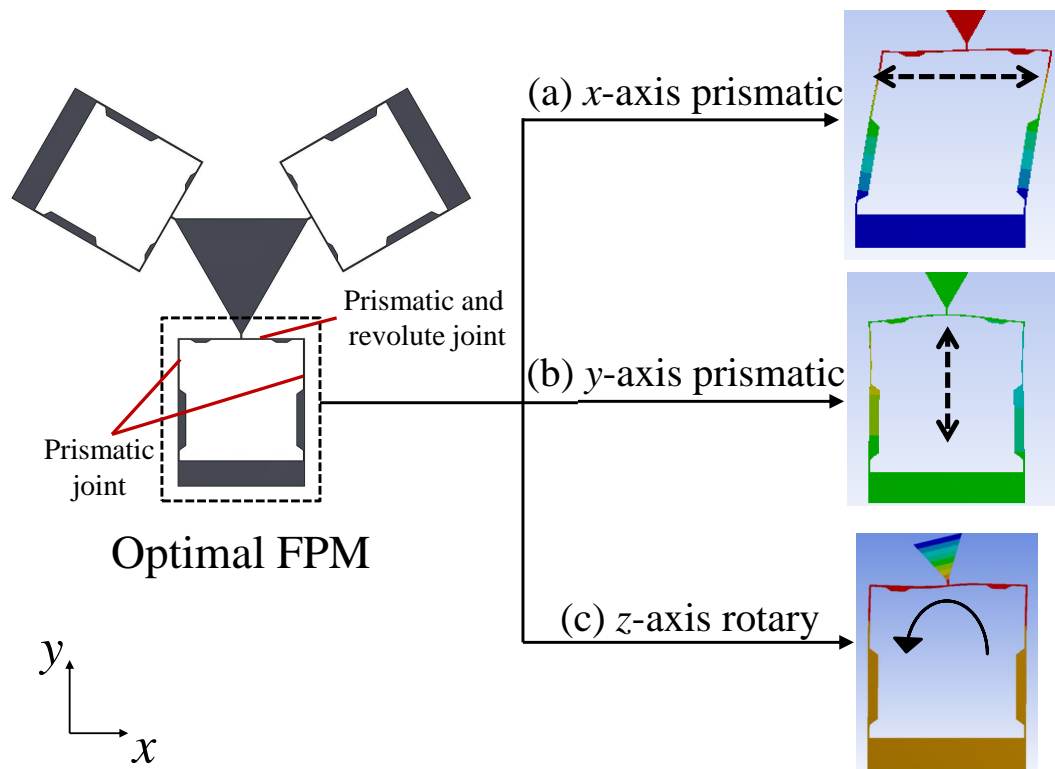
Figure 5.12: The obtained FPM resembles a 3-legged-Prismatic-Prismatic-Revolute configuration. The compliant joint motions of the sub-chains are shown on the right.

5.4 Experiments

As a proof-of-concept, a cheaper material, aluminum 6061, is used to construct our prototype. Its Young's modulus is 69 GPa and it is slightly lower than the simulated Young's modulus (71 GPa). Furthermore, due to manufacturing errors, the dimensions of the prototype are slightly different from the conceptual design shown in Fig. 5.10. By accounting for such changes, the FPM's updated simulated stiffness and dynamic properties are shown in Tables 5.2 and 5.3, respectively.

Two types of experiments, the stiffness and dynamic experiments were conducted on the prototype. The stiffness tests evaluated the stiffness properties and workspace of the FPM while the dynamic test evaluated its bandwidth. All these experiments were conducted on an anti-vibration table.

5.4.1 Stiffness experiments

Actuating Stiffness Evaluation

The FPM was connected to a linear positioner via a rigid rod. When the linear positioner applied a pushing force to the FPM, the deflection and pushing force on the FPM were measured by a micrometer and a load cell, respectively. Note that the stiffness of the rigid rod was at least 1000 times greater than the FPM's actuating stiffness. Thus, when the rigid rod was placed serially with the FPM, the deflections caused by the rigid rod were negligible. As the FPM had 3 degrees-of-freedom, three actuating stiffness - the x-axis force loading, y-axis force loading and z-axis moment loadings were evaluated. This experimental setup was shown in Fig. 5.13 by using the y-axis force loading as an illustration. The linear positioner was placed collinearly with the end-effector's y-axis. Similarly, the x-axis
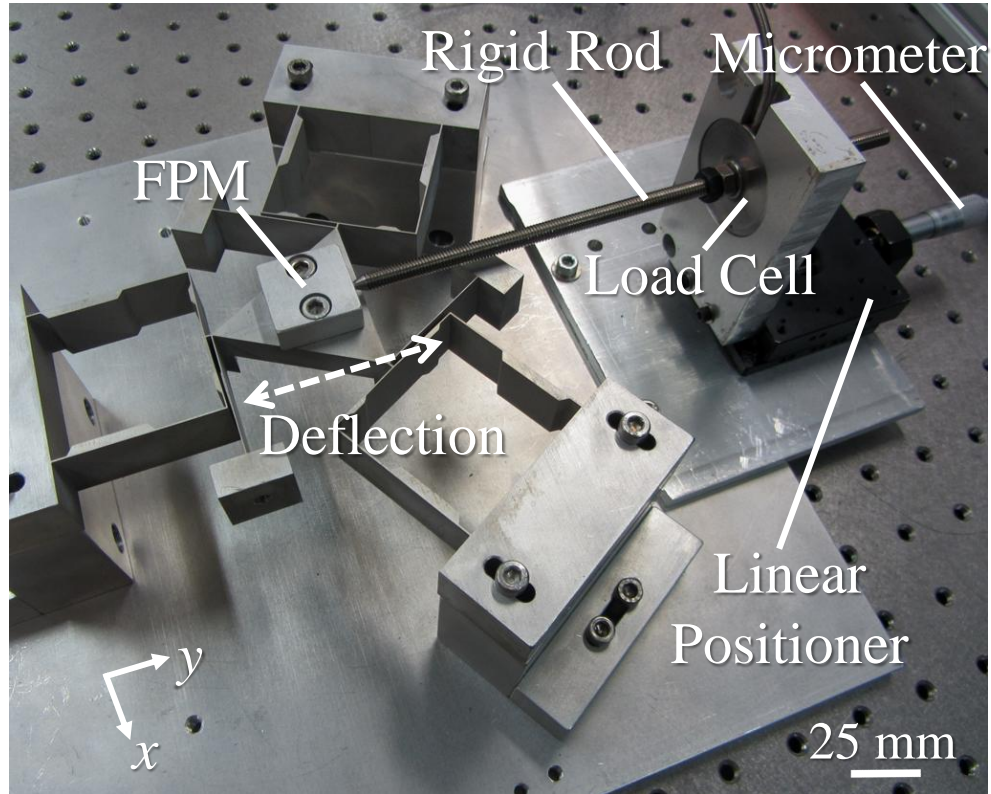
Figure 5.13: The experimental setup for evaluating the actuating stiffness of the FPM. A linear positioner is used to apply a pushing force to the FPM via a rigid rod. The linear deflection and applied force are measured by a micrometer and a load cell, respectively.

force loading was carried out by rotating the positioner $90°$ so that the positioner was aligned with the end-effector's x-axis. In the z-axis moment loadings, the positioner had an offset distance along the y-axis from the x-axis force loading configuration. This allowed the positioner to apply z-axis torques to the FPM.

For each experiment, three sets of five data points were collected. To prevent the backlash of the linear positioner, we do not allow it to move bi-directionally and have constrained its motion to become uni-directional for each set of experiment. The compiled data were represented by the plots shown in Fig. 5.15(a), (b) and (c). Based on the slope of the best fit lines, the experimentally obtained stiffness for the x-axis force loading, y-axis force loading and z-axis torque loading

were 1.89×10^4 N/m, 1.84×10^4 N/m and 10.8 Nm/rad, respectively. These results agree with the simulation results, where the corresponding stiffness are predicted to be 1.86×10^4 N/m, 1.86×10^4 N/m and 11.4 Nm/rad, respectively. The differences between the simulation results and experimental results were within 5% deviation.

Note that the pushing force would also induce an off-axis torque because the loading point of this force had a 5 mm z-axis length offset above its end-effector. However, the deflection induced by this off-axis torque was negligible. As an example, when a 1 N x-axis force was applied on the FPM, this force would also generate a 0.005 Nm torque in the y-axis. Based on the FPM's simulated stiffness properties, the translational deflection along the x-axis that was induced by the y-axis torque and x-axis force were 0.08 μm and 50 μm, respectively. In comparison, the deflection induced by the y-axis torque was 625 times less than the deflection induced by the x-axis force and thus could be neglected.

Off-axis Stiffness Evaluation

The rotational off-axis stiffness, $K_{\theta x \theta x}$ and $K_{\theta y \theta y}$, cannot be determined experimentally as their deflections were too small to be detected with our available equipments. Thus, the z-axis force loading, K_{zz}, was the only evaluated off-axis stiffness. Dead weights were placed on the FPM's platform to apply z-axis forces. The corresponding deflection was measured by a linear probe that had a resolution of 2 μm. Five sets of three data points were collected and the complied data was represented in Fig. 5.15(d). Based on the slope of the best fit line, the experimental stiffness value was 2.41×10^6 N/m. This result agreed with the simulation results, where the K_{zz} stiffness was predicted to be 2.5×10^6 N/m. The deviation between the experimental results and simulation results was within

4%.

Workspace Evaluation

The achievable workspace for the FPM was evaluated by using three 1-degree-of-freedom, bi-directional, linear actuators. As a proof-of-concept, the actuators were connected to the FPM's end-effector via simple beams as indicated in Fig. 5.14. Each beam was designed to have low bending stiffness along the directions indicated in Fig. 5.12(b) and (c), and high stiffness in other directions. When the actuators were connected to the beams, the beams' low stiffness directions functioned like the sub-chains' passive compliant joints. Based on Comsol's FEA simulations, the contribution of these stiffness had less than 5% effects on the stiffness properties indicated in Table 5.2. The beams' stiffness along the direction indicated in Fig. 5.12(a) was high so that the beams was able to move with the actuators as a rigid body. This direction served as the active compliant joint for each sub-chain. Furthermore, when the actuators were connected to the beams, the reduction in the FPM's open-loop bandwidth was less than 6% even when the moving mass of the actuators were considered. This analysis was also performed via Comsol's FEA simulations. The reduction in the open-loop bandwidth was low because the actuators had constrained one end of the beams such that they were only allowed to move along the active joint direction. This boundary condition helped to preserve the open-loop bandwidth of the FPM. Lastly, the dimensions of the thin beams were calculated to prevent buckling and other failure modes.

By driving the FPM with the actuators that could supply a maximum force of 8 N, it was found experimentally that the FPM was able to achieve its targeted workspace of 1.2 mm×1.2 mm× 6°. The actuated deflection of the FPM was
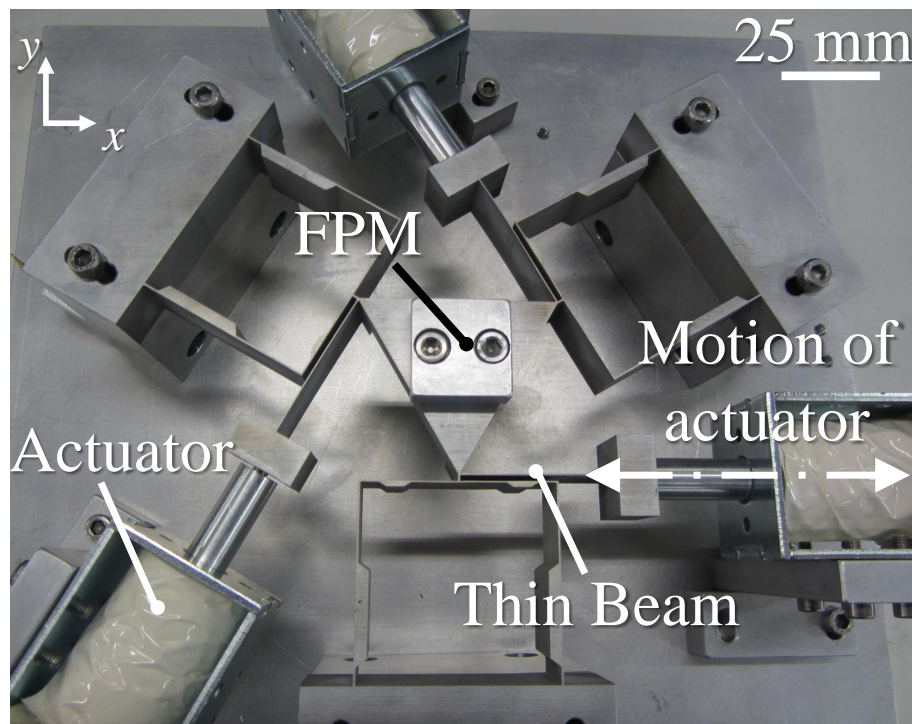
Figure 5.14: The end-effector of the FPM is directly driven by three 1-degree-of-freedom, linear actuators that are connected via simple beams. As an example, the motion of one of these actuators is indicated by the dash-dot arrow. As the end-effector has more than 1-degree-of-freedom, the motions that are unachievable by the actuators, are compensated by the compliance of the thin beams. An open-loop actuation of the prototype is shown in the supplementary video.

measured by a linear probe and a supplementary video illustrated simple open-loop actuation on the FPM.

5.4.2   Dynamic experiments

Based on the FEA in Section 5.3.4, the bandwidth of the FPM (without actuators) can be determined by evaluating the natural frequency that corresponded to either the x-axis translational or y-axis translational mode shapes. Thus, the FPM's end-effector was subjected to a knock along the y-axis to simulate an input impulse. The y-axis acceleration of the FPM was measured by an accelerometer. The frequency response of the FPM was obtained using a Fourier transform on the acceleration-time response. To obtain the standard displacement-time frequency response for the FPM, we superimpose a $\frac{1}{s^2}$ transfer function to the previous acceleration-time frequency response. The experiment was repeated six times to filter the induced noise obtained in each experiment and the average frequency response of the FPM was shown in Fig. 5.15(e). The bandwidth of the FPM was approximated by its resonance frequency, which was 102 Hz.

Similarly, the natural frequency that corresponded to the x-axis translational mode shape was determined by simulating an impulse along the x-axis. This process was repeated 6 times and the average frequency response was shown in Fig. 5.15(f). The resonance frequency for this mode shape was found to be 102.5 Hz. Lastly, the frequency response for the z-axis rotational mode shape was determined by first simulating an impulse that was parallel to the x-axis but with an offset distance, L_1, along the y-axis. This would create a torque impulse along the z-axis. As the accelerometer was placed parallel to the y-axis but with an offset distance, L_2, along the x-axis, it could determine the angular acceleration by dividing the measured acceleration with L_2. The experimental
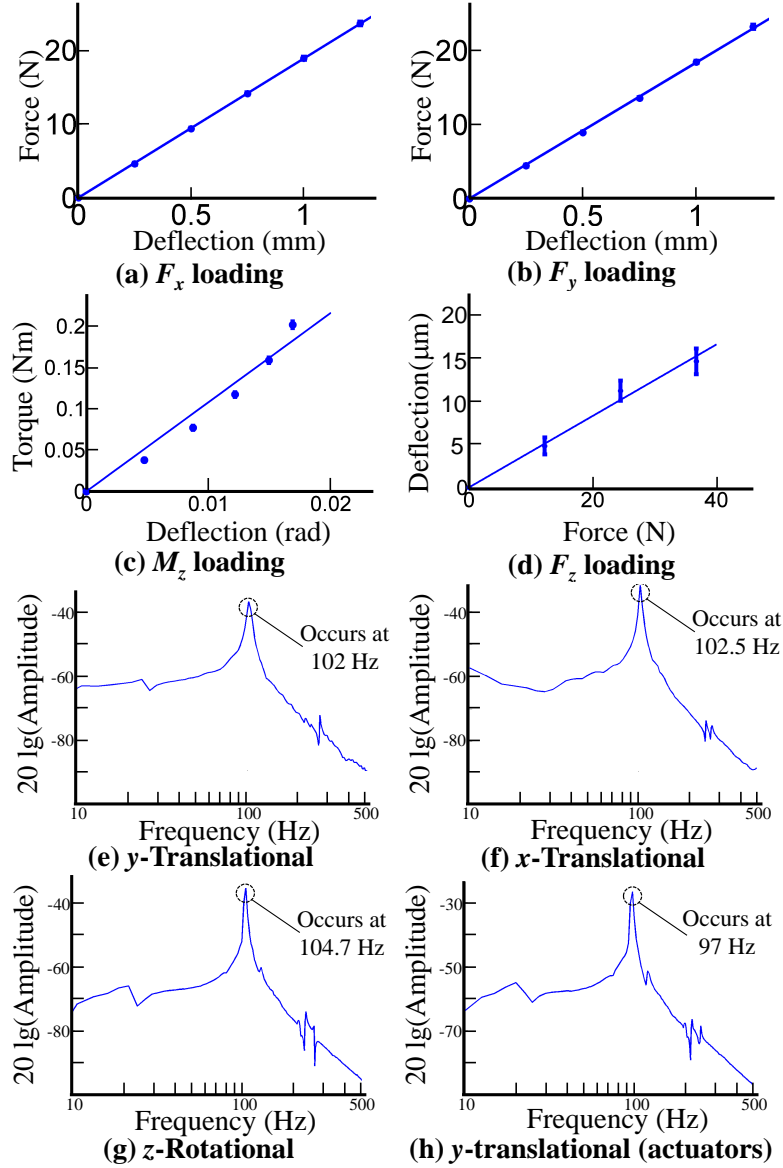
Figure 5.15: (a), (b), (c) and (d) are the experimental results for the F_x, F_y, M_z and F_z loading, respectively. The actuating stiffness experiments that are shown in (a), (b) and (c) have three sets of five data points. The off-axis stiffness experiment data that is shown in (d) have five sets of three data points. Based on the slope of the plots, the experimental K_{xx}, K_{yy}, $K_{\theta z\theta z}$ and K_{zz} stiffness of the FPM are 1.89×10^4 N/m, 1.84×10^4 N/m, 10.8 Nm/rad and 2.41×10^6 N/m, respectively. (e), (f) and (g) are the Bode plots that correspond to the FPM's translational y- and x-axes, and rotational z-axis mode shapes, respectively. Their corresponding resonance frequencies are 102 Hz, 102.5 Hz and 104.7 Hz, respectively. (h) The experimental frequency response of the FPM when it was connected to the actuators. The resonance frequency occurred at 97 Hz.
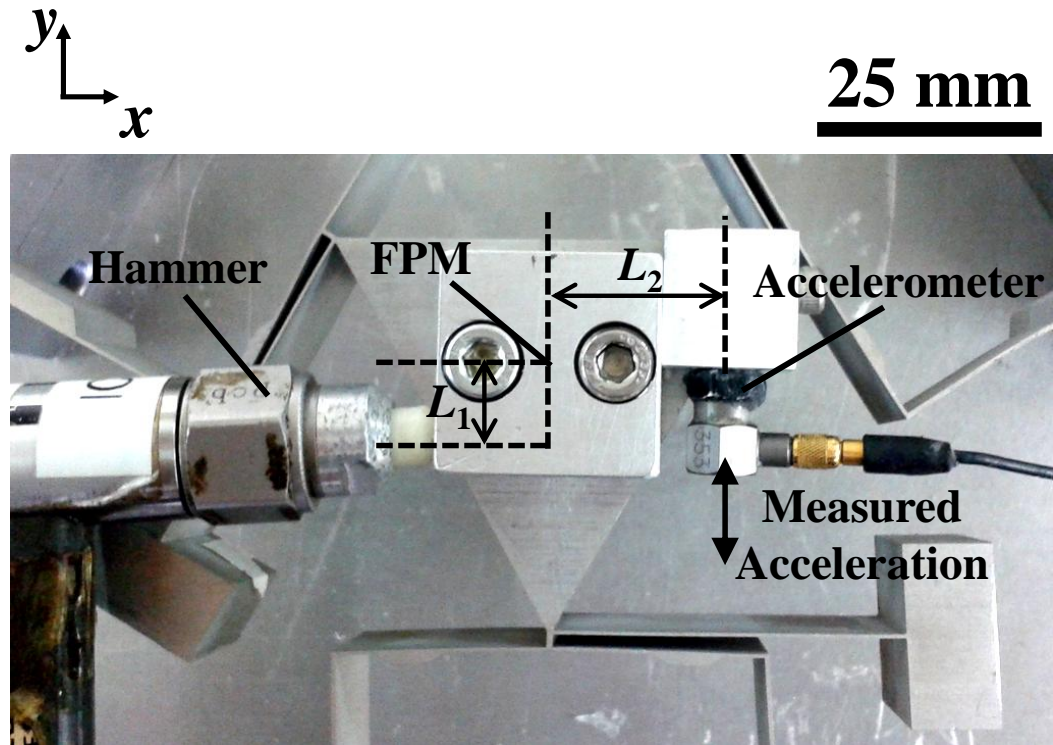
Figure 5.16: The experimental setup for evaluating the frequency response that corresponds to the z-axis rotational mode shape. A torque impulse is applied to the FPM by using the hammer to generate an impulse that is parallel to the x-axis but with an offset length of L_1 along the y-axis. As the accelerometer is placed parallel to the y-axis but with an offset length of L_2 along the x-axis, it measures the angular acceleration of the FPM by dividing the measured tangential acceleration with L_2.

setup that evaluated the z-axis rotational mode shape was shown in Fig. 5.16. Note that the accelerometer would only measure the tangential acceleration as its orientation was perpendicular to the attached point's centripetal acceleration. This experiment was repeated 6 times and the average frequency response for the rotary z-axis mode shape was shown in Fig. 5.15(g). The resonance frequency was found to be 104.7 Hz.

These experimental results agreed with Comsol simulations as the predicted natural frequencies in the translational x- and y-axes, and rotational z-axis were

Table 5.2: An overview of the FPM's stiffness properties where the simulation results are compared with the experimental data. The second and third rows represent the translational stiffness ratios while the fourth and fifth rows represent the rotational stiffness ratios of the FPM.

Stiffness Properties	Simulation	Experimental Data
K_{zz}/K_{xx}	134	128
K_{zz}/K_{yy}	134	131
$K_{\theta x \theta x}/K_{\theta z \theta z}$	111	——
$K_{\theta y \theta y}/K_{\theta z \theta z}$	111	——
K_{xx} (N/m)	1.86×10^4	1.89×10^4
K_{yy} (N/m)	1.86×10^4	1.84×10^4
K_{zz} (N/m)	2.5×10^6	2.41×10^6
$K_{\theta x \theta x}$ (Nm/rad)	1.26×10^3	——
$K_{\theta y \theta y}$ (Nm/rad)	1.26×10^3	——
$K_{\theta z \theta z}$ (Nm/rad)	11.4	10.8

111 Hz, 111 Hz and 115 Hz, respectively. The deviation between the experimental data and simulation predictions was within 9%. Note that there was a discrepancy in comparing the measured resonance frequencies $(= \omega_n \sqrt{1 - 2\zeta^2})$ with the predicted natural frequencies, ω_n, as damping effects were ignored in the latter situation. Although this friction was small, a small deviation between the resonance and natural frequencies should still be expected. The variable ζ referred to the damping ratio resultant by air friction.

Similar experiments were also performed on the FPM when it was attached to the actuators. The obtained bandwidth was 97 Hz, and the frequency response was shown in Fig. 5.15(h). This agreed with the Comsol FEA simulation, where the additional moving mass of the actuators had less than 6% effects on the FPM's open-loop bandwidth. The frequency responses of higher order mode shapes were not evaluated experimentally as their natural frequencies exceeded the working range of our available sensors.

Table 5.3: An overview of the FPM's dynamic properties where the simulation results are compared with the experimental data. The first column indicates the corresponding mode shape while the second and last column represent the simulation predictions and experimental data, respectively.

Mode Shape	Simulation	Experimental Data
y-Translational (Hz)	111	102
x-Translational (Hz)	111	102.5
z-Rotational (Hz)	115	104.7
z-Translational (Hz)	890	——
x-Rotational (Hz)	910	——
y-Rotational (Hz)	910	——

5.4.3   Discussion

Tables 5.2 and 5.3 compare the FPM's experimental stiffness and dynamic properties with its simulation results, respectively. The stiffness and dynamic experimental data agreed with the simulation results as their deviations were within 5% and 9%, respectively. These deviations could be caused by other manufacturing errors that were difficult to account for. The dynamic experimental errors were larger because there was a discrepancy in comparing the resonance frequency with the natural frequency. Note that due to damping effects, the resonance frequency was always slightly lower than the natural frequency.

5.5   Summary

In this chapter, we have introduced the generic design methodology that can integrate both the kinematic and structural optimization approaches. In order to implement this methodology, we have also proposed a generic dynamic model that can accurately predict the fundamental natural frequency of a FPM with arbitrary geometries. The universality of the proposed model will allow scientists and engineers to evaluate the dynamic characteristics of FPMs that have either 2D

or 3D motions. Using the dynamic model and the mechanism-based approach, the proposed design methodology uses a structural optimization approach to optimize the topology, shape and size of a FPM's sub-chains. This is in contrast with existing kinematic approaches where the sub-chains are only subjected to size optimizations. It is found that by including topological and shape optimizations, the FPM's dynamic and stiffness properties can be improved significantly.

A FPM that has optimal sub-chains can be synthesized by first using the kinematic approach to determine its overall topology. Subsequently, a structural optimization method is applied to synthesize the sub-chains of the FPM by determining their optimal topology, shape and size sequentially. The topological and shape optimizations aim to select an optimal configuration for the FPM to realize its desired kinematics. This is achieved by formulating optimization problems that can maximize the stiffness ratios of the FPM. Based on the optimal topology and shape, a size optimization is then used to optimize the FPM's dynamic properties.

The proposed synthesis approach is illustrated via designing a planar $X-Y-\theta_z$ FPM. This FPM is evaluated experimentally to have a large workspace of 1.2 mm $\times$ 1.2 mm $\times$ $6°$, bandwidth of 102 Hz, and stiffness ratios above 120. The improvement in stiffness ratio is significant compared to existing centimeter-scale compliant mechanisms with 3-degrees-of-freedom. The stiffness ratios of these compliant mechanisms are typically between $0.5-50$ [7, 8, 9, 46, 50, 51, 52, 53]. Furthermore, the bandwidth of existing large workspace compliant mechanisms, which have translational and rotational deflections greater than 0.5 mm and $0.5°$ respectively, do not exceed 45 Hz [7, 8, 46, 52]. From the synthesized FPM, we have demonstrated the benefits of performing topological and shape optimizations on the sub-chains. It should be noted that there is no loss of generality in

applying the proposed approach to optimize the natural frequency of higher vibrational modes. We envision that the proposed design methodology can be used universally to create multi-degrees-of-freedom FPMs that have optimal dynamic and stiffness properties.

Chapter 6

Conclusion and Future Works

6.1 Conclusion

In this research, a new design methodology that can synthesize multi-degrees-of-freedom FPMs with optimal stiffness and dynamic properties has been established. This methodology is specifically created to address the limitations of existing synthesis approaches, which are unable to optimize these properties when the compliant mechanisms have multi-degrees-of-freedom. In order to implement this methodology, we have developed a new topological optimization algorithm termed the mechanism-based approach, and also a generic semi-analytical dynamic model that can accurately predict the fundamental natural frequencies of FPMs with arbitrary geometries. The effectiveness of the proposed methodology has been illustrated via the synthesis of an optimal $X - Y - \theta_z$ FPM. The main contributions of this work are summarized as follows:

- **The Development of Mechanism-based Approach for Synthesis**

  As many existing topological optimization algorithms may produce infeasible solutions, a new topological optimization algorithm termed

the mechanism-based approach has been developed specifically for the proposed design methodology. Based on the required degrees-of-freedom of the compliant mechanism, the mechanism-based approach will first identify various traditional mechanisms that can satisfy this requirement. These mechanisms are termed as seeds and their geometrical characteristics will be used to create the topology of a compliant mechanism. By gradually evolving the seeds' geometrical properties with genetic algorithm, an optimal compliant mechanism will eventually emerge. A notable advantage of the mechanism-based approach is that it will never produce disconnected solid elements because the links of the seed are always physically connected. Furthermore, as the selection of the solid elements is done in a discrete manner, the possibility of having ambiguous "grey" elements is eliminated. Lastly, this algorithm does not overconstrain the topology of the compliant mechanism because it has been shown that even the "topology" of the seeds can be changed. The effectiveness of this algorithm has been evaluated via several case studies, including the development of a μ-gripper, a compliant $\underline{P}$ joint, and a compliant PR joint that have optimal stiffness characteristics. For all these case studies, it has been shown that these devices are able to exhibit superior stiffness characteristics compared to the ones obtained via intuitive designs. Furthermore, the convergence plots for all of the case studies suggest that the mechanism-based approach has good convergence properties. While the mechanism-based approach shows promise, it has two main limitations. First, it can only simplify a complex topology but cannot change a simple topology into a more complicated one. Second, it requires more computational time compared to algorithms such as the

SIMP and homogeneous methods. A feasible solution to moderate the first limitation will be to include more complex seeds during the optimization process, allowing our proposed algorithm to have a larger search space. On the other hand, we can reduce the computational time by converting our programming platform from Matlab to C++ to speed up the computational process. Both of these proposed solutions will be explored as future work.

- **A Generic Dynamic Model for FPMs**

In order to have a generic design methodology that can produce FPMs with optimal dynamic properties, the derivation of a universe model that can accurately predict the fundamental natural frequency of a FPM with arbitrary geometries will be required. An analytical model, however, maybe too difficult when the geometries of the sub-chains are too complex. Alternatively, if a full FEA is implemented, the entire optimization process would be too computationally expensive. In view of this, we had proposed a semi-analytical dynamic model where the derivation of the model is divided into two stages. The first stage will use a FEA dynamic condensation to obtain the lump mass and stiffness matrices for the sub-chains. This will be followed by the second stage where the Lagrangian method will use all these lump matrices and the inertia of the end-effector to obtain the equations of motion for the FPM. The accuracy of the model has been evaluated by at least 20 structures with arbitrary geometries. The fundamental natural frequency of these structures obtained by the proposed model has less than 3% deviation compared to a full FEA dynamic model - suggesting high credibility for the model.

- **Design Methodology for Multi-degrees-of-freedom FPMs with Optimal Stiffness and Dynamic Properties**

The proposed design methodology is realized by integrating the benefits of two existing synthesis approaches - the kinematic and the structural optimization approaches. First, the rigid-body-replacement method is used to determine suitable parallel-kinematics configurations for the compliant mechanism. This reduced the complexity of using a structural optimization approach to synthesize a compliant mechanism with multi-degrees-of-freedom - overcoming the previous challenges of existing structural optimization methods. Subsequently, the mechanism-based approach and the generic dynamic model are utilized to synthesize the sub-chains of the FPM by determining their optimal structural topology, shape and size sequentially. By automating this process, the proposed integrated design methodology has the potential to surpass traditional FPMs that are synthesized via the kinematic approach. The effectiveness of the proposed approach is demonstrated via synthesizing a $X-Y-\theta_z$ FPM that has a large workspace of 1.2 mm$\times$1.2 mm$\times$6°. This FPM (shown in Fig. 6.1) has significantly better stiffness and dynamic properties over existing 3-degrees-of-freedom, centimeter-scale compliant mechanisms. For example, this FPM can achieve a large translational and rotational stiffness ratio of 130 and 108 respectively while existing ones can only achieve 0.5-50. Likewise, the synthesized FPM has a large bandwidth of 117 Hz while other existing large workspace FPMs, which can deflect more than 0.5 mm and 0.5°, can only achieve bandwidths that are lower than 45 Hz. The stiffness and dynamic properties of the FPM have been evaluated experimentally via a
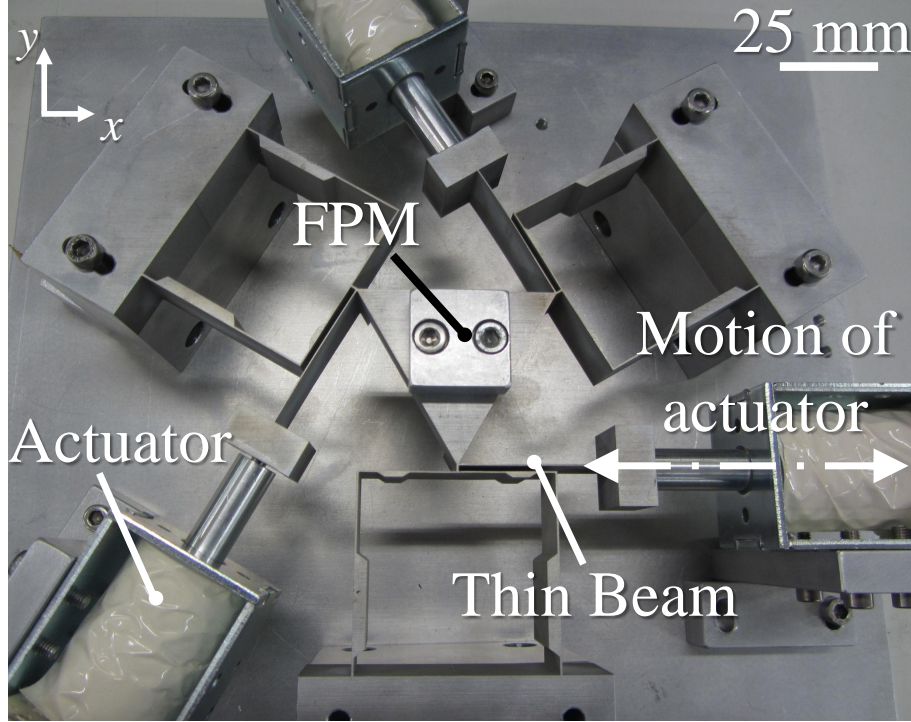
Figure 6.1: The optimal $X - Y - \theta_z$ FPM.

prototype. The experimental stiffness properties and bandwidth agree with the simulation results as their deviations are within 5% and 9%, respectively. Although there is no loss in generality to implement the proposed method to synthesize FPMs with non-planar motions, currently such synthesis would require too much computational time. Therefore, we will try to reduce the computational time by switching the programming platform from Matlab to C++.

In conclusion, the presented scope in this thesis can guide engineers to design multi-degrees-of-freedom FPMs that have optimal stiffness and dynamic properties. We envision that this study will inspire the design and development of a variety of new high precision machines that have large workspaces, strong capabilities to reject disturbances, and fast transient responses.

135

6.2 Future Works

Although a universal design methodology has been developed, there remains several aspects in this area that have yet to be explored.

- **Development of other FPMs**

  Currently, the proposed design methodology has only been used to develop a $X - Y - \theta_z$ FPM. It will be interesting, however, to use this methodology to develop other types of planar FPMs like a $X - Y$ precision stage, or other spatial-motioned FPMs like a $X - Y - Z$ or a $\theta_x - \theta_y - Z$ stage. As the spatial FPMs would require more computational resources, the mechanism-based approach would have to be modified to optimize its computational efficiency for such FPMs. Finally, as compliant mechanisms can be scaled down easily, this methodology can be explored to create novel, functional MEMS devices or micro-robots.

- **Design Methodology for Soft Robots**

  In recent years, the design and development of soft robots have become increasingly popular within the robotics community. Despite the popularity in this subject, the design of current soft robots may not be optimal as they rely heavily upon human intuition. As it is necessary to account for both the geometrical design and actuation modes concurrently, it may be difficult to depend solely on human intuition to design these robots. Thus, we believe it might be beneficial to modify the current design methodology such that it can become suitable to synthesize soft robots that have optimal performance. This modification, however, will be non-trivial as the soft robots have much larger deflections compared to flexure mechanisms - the strains of these robots are usually greater than one. Thus, it will be

136

necessary to modify the FEA such that it can accurately predict large deflections, and also the optimization formulations have to be adapted to suit these applications.

- **Integrated Mechatronics Approach**

  Lastly, a concept termed the integrated mechatronics approach has been recently proposed. For this concept, they will consider the performance of the entire system during the synthesis phase by accounting for the control aspect of the system. By implementing such concepts for the high precision machines, it might be possible to further enhance the performance of such systems. However, before this design approach can be implemented, new fitness functions and design parameters have to be explored in the future.

List of Author's Publication

Journal Publications

1. **G. Z. Lum**, T. J. Teo, G. L. Yang, S. H. Yeo and M. Sitti, "Integrating classical mechanism synthesis and modern topological optimization technique for stiffness-oriented design of three degrees-of-freedom flexure-based parallel mechanisms", *Precision Engineering*, vol. 39, pp. 125-133, January 2015.

2. **G. Z. Lum**, T. J. Teo, G. L. Yang, S. H. Yeo and M. Sitti, "Structural optimization for flexure-based parallel mechanisms - Towards achieving optimal dynamic and stiffness properties", *Precision Engineering*, vol. 42, pp. 195-207, October 2015.

Conference Publications

1. **G. Z. Lum**, T. J. Teo, G. L. Yang, S. H. Yeo and M. Sitti, "Topological optimization for continuum compliant mechanisms via morphological evolution of traditional mechanisms", *4th International Conference on Computational Methods*, Gold Coast, Australia, Nov 2012, pp. 2008-2014.

2. T. J. Teo, **G. Z. Lum**, G. L. Yang, S. H. Yeo and M. Sitti, "Geometrical-based approach for flexure mechanism design", *13th International Conference of European Society for Precision Engineering and Nanotechnology*, Berlin, Germany, May 2013, pp. 184-187.

3. **G. Z. Lum**, T. J. Teo, G. L. Yang, S. H. Yeo and M. Sitti, "A novel hybrid topological and structural optimization method to design a 3-DOF planar motion compliant mechanism", *IEEE/ASME International Conference on Advanced Intelligent Mechatronics*, Wollongong, Australia, July 2013, pp.

247-254.

4. **G. Z. Lum**, E. Diller, and M. Sitti, "Structural optimization method towards synthesis of small scale flexure-based mobile grippers", *IEEE International Conference on Robotics and Automation*, Hong Kong, China, May 2014, pp. 2339-2344.

Award

Received Third Prize at the 2012 A*STAR-SIMTech Postgraduate Posters Exhibition

Appendix A

CAD Drawings for Synthesized Flexural Mechanisms

This section presents the detailed 2-D CAD drawing for the synthesized compliant P and PR joints, the 3PPR FPM and the optimal $X - Y - \theta_z$ FPM. Except for the 3PPR FPM, which is constructed by stainless steel, the rest of the flexure mechanisms are made by aluminum. The thickness of the compliant joints are 10 mm while the FPMs' thickness are 20 mm. All of these flexure mechanisms are fabricated by wire-EDM techniques.

Figure A.1: The 2D CAD drawing for the synthesized compliant P joint. The units for all the dimensions are in millimeters and the thickness of the joint is 10 mm.

Figure A.2: The 2D CAD drawing for the synthesized compliant PR joint. The units for all the dimensions are in millimeters and the thickness of the joint is 10 mm.
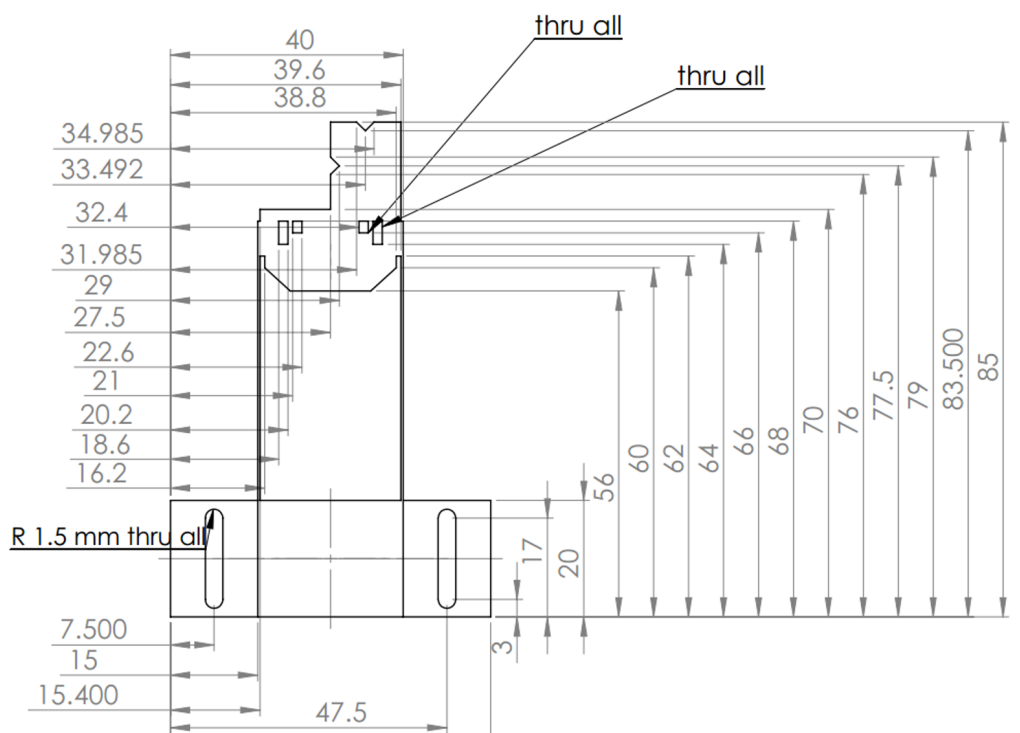

Figure A.3: The 2D CAD drawing for the synthesized 3PPR FPM. The units for all the dimensions are in millimeters and the thickness of the joint is 20 mm.
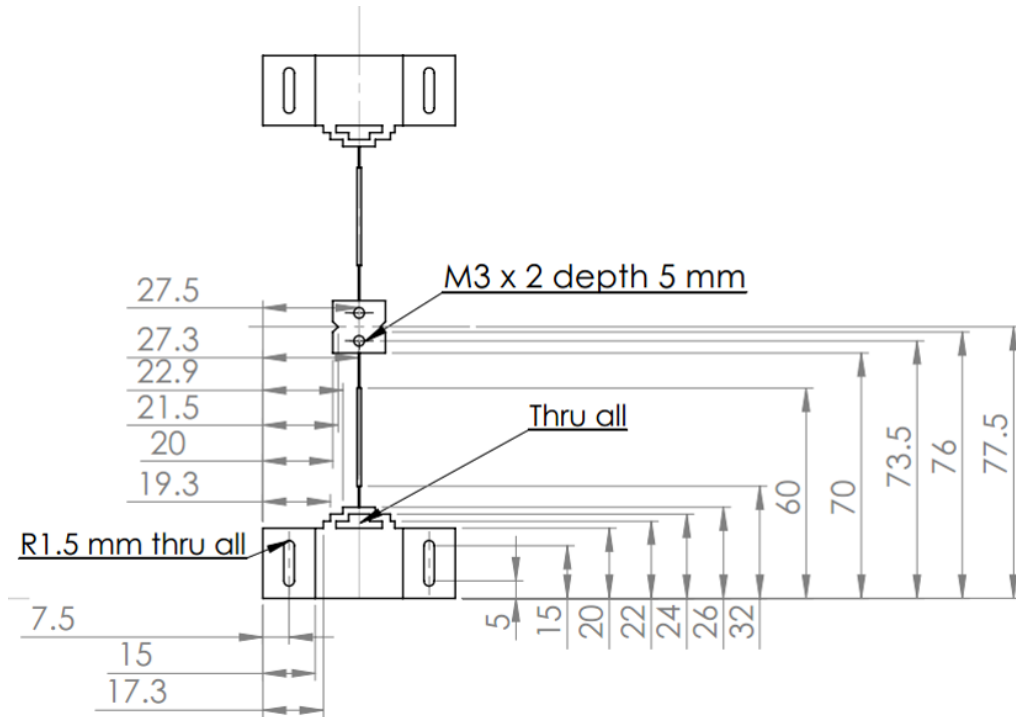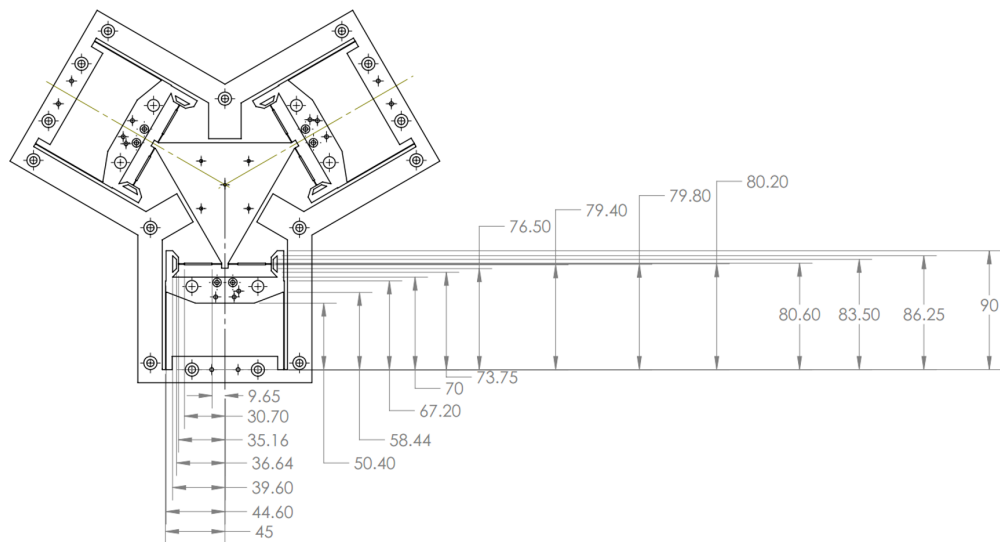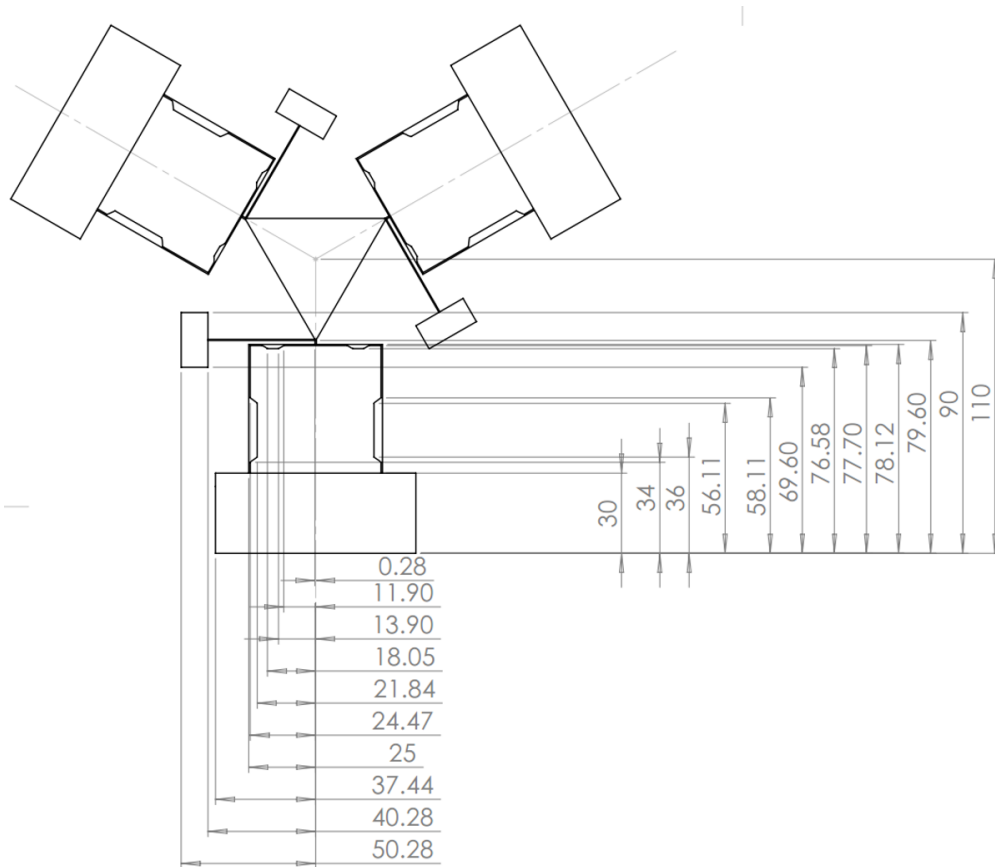
Figure A.4: The 2D CAD drawing for the synthesized optimal $X - Y - \theta_z$ FPM. The units for all the dimensions are in millimeters and the thickness of the joint is 20 mm.

Bibliography

[1] L. L. Howell, *Compliant mechanisms*. Wiley, 2001.

[2] S. T. Smith, *Flexures: elements of elastic mechanisms*. Gordon & Breach, 2000.

[3] Y. Bellouard, *Microrobtics: methods and applications*. CRC Press, 2010.

[4] D. L. Blanding, *Exact constraint: machine design using kinematic principles*. ASME Press, 1999.

[5] L. C. Hale, *Principles and techniques for designing precision machines*. PhD Thesis, Massachusetts Institute of Technology, 1999.

[6] J. A. Miller, R. Hocken, S. T. Smith, and S. Harb, "X-ray calibrated tunneling system utilizing a dimensionally stable nanometer positioner," *Precision Engineering*, vol. 18, no. 23, pp. 95 – 102, 1996.

[7] T. J. Teo, G. Yang, and I. M. Chen, "A large deflection and high payload flexure-based parallelmanipulator for uv nanoimprint lithography: part i. modeling and analyses," *Precision Engineering*, vol. 38, pp. 861–871, October 2014.

[8] T. J. Teo, I. M. Chen, and G. Yang, "A large deflection and high payload flexure-based parallelmanipulator for uv nanoimprint lithography: part ii. stiffness modeling and performance evaluation," *Precision Engineering*,

vol. 38, pp. 872–884, October 2014.

[9] J. W. Ryu, D. G. Gweon, and K. S. Moon, "Optimal design of a flexure hinge based $x-y-\theta_z$ wafer stage," *Precision Engineering*, vol. 21, pp. 18–28, July 1997.

[10] C. W. Lee and S. W. Kim, "An ultraprecision stage for alignment of wafers in advanced microlithography," *Precision Engineering*, vol. 21, pp. 113–122, September 1997.

[11] G. Yang, W. Lin, T. Teo, and C. Kiew, "A flexure-based planar parallel nanopositioner with partially decoupled kinematic architecture," in *EU-SPEN International Conference*, (Zurich, Switzerland), pp. 2751–2756, June 2009.

[12] T. Lu, D. C. Handley, Y. K. Yong, and C. Eales, "A three-dof compliant micromotion stage with flexure hinges," *Industrial Robot: An International Journal*, vol. 31, no. 4, pp. 355–361, 2004.

[13] A. A. Eielsen, M. Vagia, J. T. Gravdahl, and K. Y. Pettersen, "Damping and tracking control schemes for nanopositioning," *IEEE/ASME Transactions on Mechatronics*, vol. 19, pp. 432–444, April 2014.

[14] M. N. M. Zubir and B. Shirinzadeh, "Development of a high precision flexure-based microgripper," *Precision Engineering*, vol. 33, no. 4, pp. 362 – 370, 2009.

[15] X. Shi, W. Chen, J. Zhang, and W. Chen, "Design, modeling, and simulation of a 2-dof microgripper for grasping and rotating of optical fibers," in *IEEE/ASME International Conference on Advanced Intelligent Mechatronics*, (Wollongong, Australia), pp. 1597–1602, 2013.

[16] M. Grossard, C. Rotinat-Libersa, N. Chaillet, and M. Boukallel, "Mechan-

ical and control-oriented design of a monolithic piezoelectric microgripper using a new topological optimization method," *IEEE/ASME Transactions on Mechatronics*, vol. 14, pp. 32–45, February 2009.

[17] D. Mukhopadhyay, J. Dong, E. Pengwang, and P. Ferreira, "A soi-mems-based 3-dof planar parallel-kinematics nanopositioning stage," *Sensors and Actuators A: Physical*, vol. 147, pp. 340 – 351, April 2008.

[18] N. Lobontiu and E. Garcia, "Analytical model of displacement amplification and stiffness optimization for a class of flexure-based compliant mechanisms," *Computers and Structures*, vol. 81, pp. 2797 – 2810, July 2003.

[19] K. Sharma, I. G. Macwan, L. Zhang, L. Hmurick, and X. Xiong, "Design optimization of mems comb accelerometer," in *in ASEE Zone 1 Conference 2008, United States Military Academy*, (New York, USA), pp. 833–837, July 2008.

[20] F. Peano and T. Tambosso, "Design and optimization of a mems electret-based capacitive energy scavenger," *Journal of microelectromechanical systems*, vol. 14, pp. 429 – 435, June 2005.

[21] O. Sigmund, "Design of multiphysics actuators using topology optimization - part i: One-material structures," *Computer Methods in Applied Mechanics and Engineering*, vol. 190, pp. 6577 – 6604, October 2001.

[22] O. Sigmund, "Design of multiphysics actuators using topology optimization - part ii: Two-material structures," *Computer Methods in Applied Mechanics and Engineering*, vol. 190, pp. 6605 – 6627, October 2001.

[23] M. D. Murphy, A. Midha, and L. . L. Howell, "The topological synthesis of compliant mechanisms," *Mechanisms and Machine Theory*, vol. 31, no. 2, pp. 185–199, 1996.

[24] S. Chen and M. Y. Wang, "Designing distributed compliant mechanisms with characteristic stiffness," in *ASME International Design Engineering Technical Conferences and Computers and Information in Engineering Conference*, (Nevada, USA), pp. 33–45, 2008.

[25] M. Y. Wang, "A kinetoelastic approach to continuum compliant mechanism optimization," in *ASME International Design Engineering Technical Conferences and Computers and Information in Engineering Conference*, (New York, USA), pp. 183–195, August 2009.

[26] M. P. Bendse and O. Sigmund, *Topology optimization: theory, methods, and applications*. Springer, 2003.

[27] Y. M. Xie and G. P. Steven, *Evolutionary structural optimization*. Springer, 1997.

[28] S. Shuib, M. I. Z. Ridazwan, and A. H. Kadarman, "Methodology of compliant mechanisms and it current developments in applications: A review," vol. 4, pp. 160–167, 2007.

[29] K. Tai and T. H. Chee, "Design of structures and compliant mechanisms by evolutionary optimization of morphological representations of topology," *Journal of Mechanical Design*, vol. 122, pp. 560–566, December 2000.

[30] P. Bernardoni, P. Bidaud, C. Bidard, and F. Gosselin, "A new compliant mechanism design methodology based on flexible building blocks," Society of Photo-Optical Instrumentation Engineers (SPIE) Conference Series, (France), pp. 244–254, July 2004.

[31] J. Zhan and X. Zhang, "Topological optimization of multiple inputs and multiple outputs compliant mechanisms using the ground structure," in *IEEE/ASME International Conference on Advance Intelligent Mechatron-*

ics, (Singapore, Singapore), pp. 833–837, July 2009.

[32] N. F. Wang and K. Tai, "Design of 2-dof compliant mechanisms to form grip-and-move manipulators for 2d workspace," *Journal of Mechanical Design*, vol. 132, pp. 0310071–0310079, March 2010.

[33] H. H. Pham and I. M. Chen, "Stiffness modeling of flexure parallel mechanism," *Precision Engineering*, vol. 29, no. 4, pp. 467–478, 2005.

[34] L. C. Hale and A. H. Slocum, "Optimal design techniques for kinematic couplings," *Precision Engineering*, vol. 25, no. 2, pp. 114–127, 2001.

[35] S. Awtar and A. H. Slocum, "Constraint-based design of parallel kinematic xy flexure mechanisms," *ASME Journal of Mechanical Design*, vol. 129, no. 8, pp. 816–830, 2006.

[36] J. B. Hopkins and M. L. Culpepper, "Synthesis of multi-degree of freedom, parallel flexure system concepts via freedom and constraint topology (fact) - part i: principles," *Precision Engineering*, vol. 34, pp. 259–270, July 2010.

[37] J. B. Hopkins and M. L. Culpepper, "Synthesis of multi-degree of freedom, parallel flexure system concepts via freedom and constraint topology (fact) - part ii: practice," *Precision Engineering*, vol. 34, pp. 271–278, July 2010.

[38] J. B. Hopkins and M. L. Culpepper, "Synthesis of precision serial flexure systems using freedom and constraint topologies (fact)," *Precision Engineering*, vol. 35, pp. 638–649, July 2011.

[39] H. J. Su, D. V. Dorozhkin, and J. M. Vance, "A screw theory approach for the type synthesis of compliant mechanisms with flexures," in *International Design Engineering Technical Conferences & Computers and Information in Engineering Conference*, (California, USA), pp. DETC2009–86684, September 2009.

[40] J. A. Gallego and J. Herder, "Synthesis methods in compliant mechanisms: An overview," in *in ASME International Design Engineering Technical Conferences and Computers and Information in Engineering Conference*, (California, USA), pp. 193–214, 2010.

[41] Y. Tian, B. Shirinzadeh, D. Zhang, and Y. Zhong, "Three flexure hinges for compliant mechanism designs based on dimensionless graph analysis," *Precision Engineering*, vol. 34, no. 1, pp. 92 – 100, 2010. CIRP-CAT 2007.

[42] S. Polit and J. Dong, "Development of a high-bandwidth xy nanopositioning stage for high-rate micro-/nanomanufacturing," *Mechatronics, IEEE/ASME Transactions on*, vol. 16, pp. 724–733, Aug 2011.

[43] Y. Li and Q. Xu, "Design and analysis of a totally decoupled flexure-based xy parallel micromanipulator," *Robotics, IEEE Transactions on*, vol. 25, pp. 645–657, June 2009.

[44] Q. Xu, "Design and development of a compact flexure-based xy precision positioning system with centimeter range," *Industrial Electronics, IEEE Transactions on*, vol. 61, pp. 893–903, Feb 2014.

[45] Q. Yao, J. Dong, and P. Ferreira, "Design, analysis, fabrication and testing of a parallel-kinematic micropositioning {XY} stage," *International Journal of Machine Tools and Manufacture*, vol. 47, no. 6, pp. 946 – 961, 2007.

[46] H. Kim and D.-G. Gweon, "Development of a compact and long range x–y–θ_z nano-positioning stage," *Review of Scientific Instruments*, vol. 83, pp. –, August 2012.

[47] X. Tang, I.-M. Chen, and Q. Li, "Design and nonlinear modeling of a large-displacement xyz flexure parallel mechanism with decoupled kinematic structure," *Review of Scientific Instruments*, vol. 77, no. 11, 2006.

[48] D. Zhu and Y. Feng, "A spatial 3-dof translational compliant parallel manipulator," in *International Conference on Mechanical Engineering and Green Manufacturing*, (Hunan, China), pp. 143–147, 2010.

[49] Y. Li and Q. Xu, "A totally decoupled piezo-driven xyz flexure parallel micropositioning stage for micro/nanomanipulation," *Automation Science and Engineering, IEEE Transactions on*, vol. 8, pp. 265–279, April 2011.

[50] H.-Y. Kim, D.-H. Ahn, and D.-G. Gweon, "Development of a novel 3-degrees of freedom flexure based positioning system," *Review of Scientific Instruments*, vol. 83, pp. –, May 2012.

[51] B. J. Yi, G. Chung, H. Y. Na, W. H. Kim, and I. H. Suh, "Design and experiment of a 3-dof parallel micromechanism utilizing flexure hinges," *IEEE Transactions on Robotics and Automation*, vol. 19, pp. 604–612, August 2003.

[52] G. Yang, T. J. Teo, I.-M. Chen, and W. Lin, "Analysis and design of a 3-dof flexure-based zero-torsion parallel manipulator for nano-alignment applications," in *IEEE International Conference on Robotics and Automation*, (Shanghai, China), pp. 2751–2756, May 2011.

[53] Y. Tian, B. Shirinzadeh, and D. Zhang, "Design and dynamics of 3-dof flexure-based parallel mechanism," *Microelectronics Engineering*, vol. 87, pp. 230–241, February 2010.

[54] M. P. Bendse and N. Kikuchi, "Generating optimal topologies in structural design using a homogenization method," *Computer Methods in Applied Mechanics and Engineering*, vol. 71, pp. 197–224, November 1988.

[55] O. Sigmund and J. Petersson, "Numerical instabilities in topology optimization: A survey on procedures dealing with checkerboards, mesh-

dependencies and local minima," *Structural Optimization*, vol. 16, no. 1, pp. 68–75, 1998.

[56] S. Ananiev, "On equivalence between optimality criteria and projected gradient methods with application to topoloy optimization problem," *Multibody System Dynamics*, vol. 13, no. 1, pp. 25–38, 2005.

[57] N. P. Garcia-Lopez, M. Sanchez-Silva, A. L. Medaglia, and A. Chateauneuf, "A hybrid topology optimization methodology combining simulated annealing and simp," *Computers and Structures*, vol. 89, no. 15-16, pp. 1512–1522, 2011.

[58] X. Liu, Z. Li, L. Wang, and J. Wang, "Solving topology optimization problems by the guide-weight method," *Frontiers of Mechanical Engineering*, vol. 6, no. 1, pp. 136–150, 2011.

[59] H. Panganiban, G. W. Jang, and T. J. Chung, "Topology optimization of pressure-actuated compliant mechanisms," *Finite Elements in Analysis and Design*, vol. 46, no. 3, pp. 238–246, 2010.

[60] J. Lin, Z. Luo, and L. Tong, "A new multi-objective programming scheme for topology optimization of compliant mechanisms," *Structural and Multidisciplinary Optimization*, vol. 40, no. 1-6, pp. 241–255, 2010.

[61] J. Zhan, X. Zhang, and J. Hu, "Maximization of values of simple and multiple eigenfrequencies of continuum structures using topology optimization," in *International Conference on Measuring Technology and Mechatronics Automation*, (Hunan, China), pp. 833–837, 2009.

[62] X. Huang and Y. M. Xie, "A further review of eso type methods for topology optimization," *Structural and Multidisciplinary Optimization*, vol. 41, pp. 671–683, May 2010.

[63] X. Huang and Y. M. Xie, "Evolutionary topology optimization of continuum structures including design dependent self-weight loads," *Finite Elements in Analysis and Design*, vol. 47, no. 8, pp. 942–948, 2011.

[64] K. Tai and S. Akhtar, "Structural topology optimization using a genetic algorithm with a morphological geometric representation scheme," *Structural and Multidisciplinary Optimization*, vol. 30, no. 2, pp. 113–127, 2005.

[65] N. F. Wang and K. Tai, "Design of grip-and-move manipulators using symmetric path generating compliant mechanisms," *Journal of Mechanical Design*, vol. 130, no. 11, pp. 1123051–1123059, 2008.

[66] N. F. Wang and K. Tai, "Target matching problems and an adaptive constraint strategy for multiobjective design optimizations using genetic algorithms," *Computers and Structures*, vol. 88, no. 19-20, pp. 1064–1073, 2010.

[67] N. F. Wang and Y. W. Yang, "Structural design optimization subjected to uncertainty using fat bezier curve," *Computer Methods in Applied Mechanics and Engineering*, vol. 199, no. 1-4, pp. 210–219, 2009.

[68] M. Y. Wang, X. Wang, and D. Guo, "A level set method for structural topology optimization," *Computer Methods in Applied Mechanics and Engineering*, vol. 192, pp. 227–246, January 2003.

[69] X. Wang, Y. Mei, and M. Y. Wang, "Incorporating topological derivatives into level set methods for structural topology optimization," in *10th AIAA/ISSMO Multidisciplinary Analysis and Optiization Conference*, (New York, USA), pp. 2923–2932, 2004.

[70] X. Wang, M. Wang, and D. Guo, "Structural shape and topology optimization in a level-set-based framework of region representation," *Structural and*

Multidisciplinary Optimization, vol. 27, no. 1-2, pp. 1–19, 2004.

[71] P. Wei and M. Y. Wang, "Piecewise constant level set method for structural topology optimization," *International Journal for Numerical Methods in Engineering*, vol. 78, no. 4, pp. 379–402, 2009.

[72] J. Zhan and X. Zhang, "Topology optimization of compliant mechanisms with geometrical nonlinearities using the ground structure approach," *Chinese Journal of Mechanical Engineering*, vol. 24, no. 2.

[73] A. Asadpoure, M. Tootkaboni, and J. K. Guest, "Robust topology optimization of structures with uncertainties in stiffness," *Computers and Structures*, vol. 89, no. 11-12.

[74] D. S. Ramrakhyani, M. I. Frecker, and G. A. Lesieutre, "Hinged beam elements for the topology design of compliant mechanisms using ground structure approach," *Structural and Multidisciplinary Optimization*, vol. 37, no. 6.

[75] M. Sauter, G. Kress, M. Giger, and P. Ermanni, "Complex-shaped beam element and graph-based optimization of compliant mechanisms," *Structural and Multidisciplinary Optimization*, vol. 36, no. 4.

[76] P. Martinez, P. Marti, and O. M. Querin, "Growth method for size, topology and geometry optimization of truss structures," *Structural and Multidisciplinary Optimization*, vol. 33, no. 1.

[77] W. Achtziger and M. Stolpe, "Truss topology optimization with discrete design variables - guaranteed global optimality and benchmark examples," *Structural and Multidisciplinary Optimization*, vol. 34, no. 1.

[78] C. J. Kim, Y.-M. Moon, and S. Kota, "A building block approach to the conceptual synthesis of compliant mechanisms utilizing compliance and stiff-

ness ellopsoids," *Journal of Mechanical Design*, vol. 130, pp. 022308–1, January 2008.

[79] G. I. N. Rozvany, "A critical review of established methods of structural topology optimization," *Structural and multidisciplinary optimization*, vol. 37, pp. 217–237, January 2009.

[80] M. J. Jakiela, C. Chapman, J. Duda, A. Adewuya, and K. Saitou, "Continuum structural topology design with genetic algorithms," *Computer Methods in Applied Mechanics and Engineering*, vol. 186, no. 2-4, pp. 339–356, 2000.

[81] C. E. Wilson, J. P. Sadler, and W. J. Michels, *Kinematics and dynamics of machinery*. Pearson Education, 2003.

[82] X. Kong and C. Gosselin, *Type synthesis of parallel mechanisms*. Springer, 2007.

[83] J. P. Merlet, *Parallel Robot*. Kluwer Academic Publishers, 2000.

[84] H.-H. Pham and I.-M. Chen, "Stiffness modeling of flexure parallel mechanism," *Precision Engineering*, vol. 29, pp. 467–478, March 2005.

[85] R. Guyan, "Reduction of stiffness and mass matrices," *AIAA Journal*, vol. 3, no. 2, p. 380, 1965.

[86] J. O'Callahan, "A procedure for an improved reduced system (irs) model," in *Seventh International Modal Analysis Conference*, (Las Vegas, USA), pp. 17–21, 1989.

[87] J. O'Callahan, P. Avitabile, and R. Riemer, "System equivalent reduction expansion process (serep)," in *Seventh International Modal Analysis Conference*, (Las Vegas, USA), pp. 29–37, 1989.

[88] T. J. Teo, G. Yang, and I.-M. Chen, *Compliant Manipulators*. Handbook of

Manufacturing Engineering and Technology, Springer, 2014.